2D and 3D high-speed multispectral optical imaging systems for in-vivo biomedical research

Matthew B. Bouchard

Submitted in partial fulfillment of the
requirements for the degree of
Doctor of Philosophy
in the Graduate School of Arts and Sciences

COLUMBIA UNIVERSITY

2014

ABSTRACT

2D and 3D high-speed multispectral optical imaging systems for in-vivo biomedical research

Matthew B. Bouchard

Functional optical imaging encompasses the use of optical imaging techniques to study living biological systems in their native environments. Optical imaging techniques are well-suited for functional imaging because they are minimally-invasive, use non-ionizing radiation, and derive contrast from a wide range of biological molecules. Modern transgenic labeling techniques, active and inactive exogenous agents, and intrinsic sources of contrast provide specific and dynamic markers of *in-vivo* processes at subcellular resolution. A central challenge in building functional optical imaging systems is to acquire data at high enough spatial and temporal resolutions to be able to resolve the *in-vivo* process(es) under study. This challenge is particularly highlighted within neuroscience where considerable effort in the field has focused on studying the structural and functional relationships within complete neurovascular units in the living brain. Many existing functional optical techniques are limited in meeting this challenge by their imaging geometries, light source(s), and/or hardware implementations. In this thesis we describe the design, construction, and application of novel 2D and 3D optical imaging systems to address this central challenge with a specific focus on functional neuroimaging applications.

The 2D system is an ultra-fast, multispectral, wide-field imaging system capable of imaging 7.5 times faster than existing technologies. Its camera-first design allows for the fastest possible image acquisition rates because it is not limited by synchronization challenges that have hindered previous multispectral systems. We present the development of this system from a bench top instrument to a portable, low-cost, modular, open source, laptop based instrument. The

constructed systems can acquire multispectral images at >75 frames per second with image resolutions up to 512 x 512 pixels. This increased speed means that spectral analysis more accurately reflects the instantaneous state of tissues and allows for significantly improved tracking of moving objects. We describe 3 quantitative applications of these systems to *in-vivo* research and clinical studies of cortical imaging and calcium signaling in stem cells. The design and source code of the portable system was released to the greater scientific community to help make high-speed, multispectral imaging more accessible to a larger number of dynamic imaging applications, and to foster further development of the software package.

The second system we developed is an entirely new, high-speed, 3D fluorescence microscopy platform called Laser-Scanning Intersecting Plane Tomography (L-SIPT). L-SIPT uses a novel combination of light-sheet illumination and off-axis detection to provide *en-face* 3D imaging of samples. L-SIPT allows samples to move freely in their native environments, enabling a range of experiments not possible with previous 3D optical imaging techniques. The constructed system is capable of acquiring 3D images at rates >20 volumes per second (VPS) with volume resolutions of 1400 x 50 x 150 pixels, over a 200 fold increase over conventional laser scanning microscopes. Spatial resolution is set by choice of telescope design. We developed custom opto-mechanical components, computer raytracing models to guide system design and to characterize the technique's fundamental resolution limits, and phantoms and biological samples to refine the system's performance capabilities. We describe initial applications development of the system to image freely moving, transgenic *Drosophila Melanogaster* larvae, 3D calcium signaling and hemodynamics in transgenic and exogenously labeled rodent cortex *in-vivo*, and 3D calcium signaling in acute transgenic rodent cortical brain slices *in-vitro*.

Contents

List of Figures and Illustrations

List of Tables

Publications and Presentations Related to the Thesis

Peer Reviewed Publications

1. M. B. Bouchard, V. Voleti, E. M. C. Hillman, et al. *Swept Oblique Light Sheet (SOLiS) imaging for ultra-fast, volumetric microscop in awake, behaving organisms*, Nature Photonics 2014, *submitted.*

2. A. Rayshubskiy, T. J. Wojtasiewicz, C. B. Mikell, M. B. Bouchard, D. Timerman, B. E. Youngerman, R. A. McGovern, M. L. Otten, P. D. Canoll, G. M. McKhann II, and E. M. C. Hillman, *Direct, intraoperative of ~0.1 Hz hemodynamic oscillations in awake human cortex: Implications for fMRI*, NeuroImage, 2014. 15(87): p. 323-31.

3. B. R. Chen, M. G. Kozberg, **M. B. Bouchard**, and E. M. C. Hillman, *A critical role for vascular endothelium in functional neurovascular coupling, in preparation*

4. M. G. Kozberg, B. R. Chen, S. E. DeLeo, **M. B. Bouchard**, and E. M. C. Hillman, *Resolving the transition from negative to positive BOLD in the developing brain,* Proceedings of the National Academy of Sciences, 2013. 110(10): p. 4380-5

5. C. B. Amoozegar, T. W, **M. B. Bouchard**, A. F. H. McCaslin, W. S. Blaner, R. M. Levenson, and E. M. C. Hillman, *Dynamic contrast enhanced optical imaging of liver function in mice*, Journal of Biomedical Optics, 2012. 17(9): p. 96003-1.

6. E. M. C. Hillman, C. B. Amoozegar, T. Wang, A. F. H. McCaslin, **M. B. Bouchard**, J. R. Mansfield, and R. M. Levenson, *In-vivo optical imaging and dynamic contrast methods for biomedical research*, Philosophical Transactions of the Royal Society A, 369 (1955), 4620-4643 (2011).

7. B. R. Chen, **M. B. Bouchard**, A. F. McCaslin, S. A. Burgess, and E. M. C. Hillman, *High-speed vascular dynamics of the hemodynamic response*, NeuroImage, 2011. 54(2):1021-30.

8. R. Sun, **M. B. Bouchard**, and E. M. C. Hillman, *SPLASSH: Open source software for camera-based high-speed, multispectral in-vivo optical image acquisition*, Biomedical Optics Express, 2010. 1(2):385-397.
    - Selected for the Optical Imaging and Spectroscopy (2011) Virtual Journal.

- Co-first author

9. **M. B. Bouchard**, B. R. Chen, S. A. Burgess, and E. M. C. Hillman, *Ultrafast multispectral optical imaging of cortical oxygenation, blood flow, and intracellular calcium dynamics*, Optics Express, 2009. 17(18):15670-8.
    - Selected for the vol. 4, iss. 10 of the Virtual Journal for Biomedical Optics

10. B. Yuan, S. A. Burgess, A. Iranmahboob, **M. B. Bouchard**, N. Lehrer, C. Bordier, and E. M. C. Hillman, *A system for high-resolution depth-resolved optical imaging of fluorescence and absorption contrast*, Review of Scientific Instruments, 2009. 80, 043706-1.

11. S. A. Burgess, **M. B. Bouchard**, B. Yuan, and E. M. C. Hillman, *Simultaneous Multi-Wavelength Laminar Optical Tomography*, Optics Letters, 2008. 33, 2710-2712.
    - Selected for the vol. 4, iss. 1 of the Virtual Journal for Biomedical Optics

12. A. J. Radosevich, **M. B. Bouchard**, S. A. Burgess, B. R. Chen, and E. M. C. Hillman, *Hyperspectral* in vivo *two-photon microscopy of intrinsic contrast,* Optics Letters, 2008. 33(18): p. 2164-2166.
    - Selected for the vol. 3, iss. 11 of the Virtual Journal for Biomedical Optics

Conference Presentations and Posters

1. V. Voleti, **M. B. Bouchard**, C. Lacefield, R. M. Bruno, and E. M. C. Hillman, *High-speed 3D in-vivo imaging of neuronal populations using laser scanning intersecting plane tomography*, at the Society for Neuroscience Annual Meeting, November, 2013 in San Diego, paper 489.11/NNN12.

2. E. M. C. Hillman, B. R. Chen, M. G. Kozberg, and **M. B. Bouchard**, *A novel mechanicam for fast neurovascular coupling*, at the Society for Neuroscience Annual Meeting, November, 2013 in San Diego, paper 86.18/CCC10-DP7.

3. S. Kim, V. Voleti, Y. Ma, E. Ramirez, M. G. Kozberg, **M. B. Bouchard**, B. R. Chen, A. Rayshubskiy, and E. M. C. Hillman, *Chronic assessment of resting state functional connectivity variance in the rat brain,* at the Society for Neuroscience Annual Meeting, November, 2013 in San Diego, paper 282.19/HHH41.

4. M. G. Kozberg, S. Rayshubskiy, B. R. Chen, **M. B. Bouchard**, and Elizabeth M. C. Hillman, *Imaging the co-development of hemodynamic and neuronal receptive fields in the neonatal brain,* at the Society for Neuroscience Annual Meeting, November, 2013 in San Diego, paper 408.10.

5. B. R. Chen, M. G. Kozberg, **M. B. Bouchard**, and E. M. C. Hillman, *The role of the vascular endothelium in neurovascular coupling,* at the Society for Neuroscience Annual Meeting, October, 2012, in New Orleans, paper 95.08-Sa.

6. M. G. Kozberg, B. R. Chen, **M. B. Bouchard**, and E. M. C. Hillman, *The development of neurovascular coupling in the neonatal brain,* at the Brain Energy Metabolism and Blood Flow Gordon Research Conference in Waterville, ME, August 2012.

7. S. Rayshubskiy, M. Shaik, A. Liu, **M. B. Bouchard**, B. L'Heureux, and E. M. C. Hillman¸ *In-vivo imaging of flavoprotein and NADH autofluorescence dynamics in the rat somatosensory cortex,* at the Brain Energy Metabolism and Blood Flow Gordon Research Conference in Waterville, ME, August, 2012.

8. J. M. Cayce, **M. B. Bouchard**, E. D. Jansen, E. M. C. Hillman, and A. Mahadevan-Jansen. *Parametric evaluation of calcium waves evoked by infrared neural stimulation,* Proc. SPIE, Vol. 8207G, Photons and Neurons IV. Paper 8207G-157, Photonics West, San Francisco, CA. January 2012.

9. C. Amoozegar, T. Persigehl, **M. B. Bouchard**, L. H. Schwartz, and E. M. C. Hillman, *Comparison of Optical and MRI dynamic contrast imaging in liver pathologies*, at the Radiological Society of North America's Annual Meeting, November, 2011, Chicago, IL.

10. B. R. Chen, B. L'Heureux, **M. B. Bouchard**, M. Castelli, and E. M. C. Hillman, *A multi-phase model of neurovascular coupling*, at the Society for Neuroscience Annual Meeting, November, 2011, Washington, D. C., paper 507.22/WW60.

11. S. Rayshubskiy, **M. B. Bouchard**, D. Timerman, C. Mikell, B. Youngerman, M. Otten, and E. M. C. Hillman, *Multispectral optical imaging of resting state fluctuations in the human cortex during neurosurgery*, at the Society for Neuroscience Annual Meeting, November, 2011, Washington, D. C., paper 204.21/YY25.

12. S. Rayshubskiy, **M. B. Bouchard**, C. Mikell, B. Youngerman, M. Otten, and E. M. C. Hillman, *Ultrafast multispectral optical imaging of the human cortex during neurosurgery*, at the 2011 Engineering Conferences International Advances in Optics for Biotechnology, Medicine, and Surgery XII, Burlington, VT, USA, June, 2011.

13. **M. B. Bouchard** and E. M. C. Hillman, *3D Laser-Scanning Intersecting Plane Tomography (L-SIPT) for High Speed, Translationless Volumetric Microscopy*. SPIE European Conferences on Biomedical Optics, Munich, Germany, May 2011, paper 8086-29.

14. M. Kozberg, S. E. DeLeo, **M. Bouchard**, and E. M. C. Hillman, *Optical imaging of neurovascular coupling during neonatal development*. Brain, Barcelona, Spain, May, 2011, abstract [823].

15. J. M. Cayce, **M. Bouchard**, B. Chen, E. D. Jansen, E. M. C. Hillman, A. Mahadevan-Jansen, *Optical imaging of signals evoked by infrared neural stimulation of the rat brain*, at Photons and Neurons III, Photonics West 2011, San Francisco, CA, paper 7883G-146.

16. **M. B. Bouchard** and EMC Hillman. *Laser-Scanning Intersecting Plane Tomography for High Speed, translationless 3D Microscopy,* in Society of General Physiologists Annual

Meeting: New Optical Methods in Cell Physiology. Marine Biological Laboratory, Woods Hole, MA. September 2010.

17. L. E. Grosberg, A. J. Radosevich, **M. B. Bouchard**, and E. M. C. Hillman. *Characterization of intrinsic contrast in intact tissues using hyperspectral two-photon microscopy,* in Society of General Physiologists Annual Meeting: New Optical Methods in Cell Physiology. Marine Biological Laboratory, Woods Hole, MA. September 2010.

18. B. R. Chen, A. F. H. McCaslin, B. L'Heureux, **M. B. Bouchard**, and E. M. C. Hillman. *Two-Photon Microscopy of Neurovascular Dynamics,* in Society of General Physiologists Annual Meeting: New Optical Methods in Cell Physiology. Marine Biological Laboratory, Woods Hole, MA. September 2010.

19. **M. B. Bouchard**, L. Grosberg, S. A. Burgess, and E M. C. Hillman, *Laser-Scanning Intersecting Plane Tomography (L-SIPT) for High Speed 3-D Imaging,* in *Biomedical Optics*, OSA Technical Digest (CD) (Optical Society of America, 2010), paper (BTuE7).

20. R. Sun, **M. B. Bouchard**, S. A. Burgess, A. J. Radosevich, and E M. C. Hillman, *A Low-Cost, Portable System for High-Speed Multispectral Optical Imaging,* in *Biomedical Optics*, OSA Technical Digest (CD) (Optical Society of America, 2010), paper (BTuD41).

21. B. R. Chen, **M. B. Bouchard**, A. F. H. McCaslin, and E. M. C. Hillman, *Characterization of cortical vascular compartment-specific hemodynamics during somatosensory stimulation*, at the Society for Neuroscience Annual Meeting, October 2009, Chicago IL.

22. **M. B. Bouchard**, B. R. Chen, S. A. Burgess, and E. M. C. Hillman, *Ultra-fast multiwavelength CCD-based optical imaging*, at the 2009 Engineering Conferences International Advances in Optics for Biotechnology, Medicine, and Surgery XI, Burlington, VT, USA, June, 2009.

23. L. Grosberg, A. J. Radosevich, **M. B. Bouchard**, B. R. Chen, E. M. C. Hillman, *Hyperspectral Two-Photon Microscopy for 3D Instant Histology*, at the 2009 Engineering Conferences International Advances in Optics for Biotechnology, Medicine, and Surgery XI, Burlington, VT, USA, June, 2009.

24. S. A. Burgess, **M. B. Bouchard**, C. Bordier, B. Chen, E. M. C. Hillman, *Fluorescence Laminar Optical Tomography for Imaging Skin*, at the 2009 Engineering Conferences International Advances in Optics for Biotechnology, Medicine, and Surgery XI, Burlington, VT, USA, June, 2009.

25. B. R. Chen, A. F. H. McCaslin, **M. B. Bouchard**, A. J. Radosevich, S. A. Burgess, B. Cauli, and E. M. C. Hillman, *High speed two-photon microscopy of reactive cortical cells* in vivo, at the 2009 Engineering Conferences International Advances in Optics for Biotechnology, Medicine, and Surgery XI, Burlington, VT, USA, June, 2009.

26. C. Amoozegar, A. F. H. McCaslin, **M. B. Bouchard**, W. S. Blaner, and E. M. C. Hillman, *Non-invasive Evaluation of Organ Function Using Dynamic Contrast Enhanced Molecular Imaging*, at the 2009 Engineering Conferences International Advances in Optics for Biotechnology, Medicine, and Surgery XI, Burlington, VT, USA, June, 2009.

27. E. M. C. Hillman, B. Chen, S. A. Burgess, A. J. Radosevich, **M. B. Bouchard**, A. K. Iranmahboob, A Das, B. Cauli. *Multidimensional functional optical imaging of the brain,* [Invited, Best of the Topicals] in: Proceedings of OSA Frontiers in Optics (FiO) October 19, 2008, Rochester, NY.

Patents

1. U.S. Patent 8,619,237 B2, Granted Dec. 31, 2013 (Elizabeth M. C. Hillman and **Matthew B. Bouchard**, applicants) "Laser-Scanning Intersecting Plane Tomography Such As For High Speed Volumetric Optical Imaging"

Definitions and list of acronyms

CT	computed tomography
DPF	differential path length factor
DSLM	digital scanned laser light-sheet microscopy
FITC	fluorescein isothiocyanate
fMRI	functional magnetic resonance imaging
FPS	frames per second
FRET	fluorescence resonance energy transfer
GCaMP	a single GFP molecule with high Ca^{2+} affinity (Nakai et al. 2001)
GECI	genetically encoded calcium indicator
GFP	green fluorescent protein
HbO_2	oxygenated hemoglobin
HbR	deoxygenated hemoglobin
HbT	total hemoglobin
L-SIPT	laser-scanning intersecting plane tomography
LCTF	liquid crystal tunable filter
LED	light emitting diode
LP	long pass
LSCTM	line-scanning confocal theta microscopy
MBLL	modified Beer-Lambert law
NA	numerical aperture

NIR	near-infrared
OCPI	objective-coupled planar illumination
OISI	optical intrinsic signal imaging
OPM	oblique plane microscopy
OPT	optical projection tomography
PSF	point spread function
RBC	red blood cell
RGB	red green blue
ROI	region of interest
SNR	signal-to-noise ratio
SPIM	selective plane illumination microscopy
VPS	volumes per second

Acknowledgements

Without the support of many people, friends, family, co-workers, and advisors, this work would never have been possible.

I'd first like to thank my parents, Janet and Philip Bouchard, and my brother, Brad, whose unflinching support and guidance in making tough life decisions has never steered me down a poor path. Mom, Dad, Brad, I love you.

Second, for the 3 years prior to and all throughout my thesis, I worked for an advisor who is without equal, Dr. Elizabeth Hillman. During my eight years under her mentorship I grew more as a scientist and as a person than I ever thought possible. Thank you Beth, for everything.

I would like to thank my thesis committee, Dr. Henry Hess, Dr. Andreas Hielscher, Dr. Jung-Chi Liao, and Dr. Ken Shepard for their scientific insight, guidance, and support throughout the thesis process.

I owe a great deal of gratitude to Professor Charles DiMarzio, Dr. Bill Warger, Shelia DiMarzio, and Maya Silvis from Northeastern University. Chuck and Bill pulled me into biomedical optical imaging right from the start of undergrad and kept me there for the next 10 years. Without the Northeastern crew my life today could have been working on oil rigs in Siberia. Thanks guys.

Thanks goes to Keith Yeager, the maestro of rapid prototyping, for helping me build a zoo of crazy mechanical devices and Professor Aaron Kyle for teaching me advanced electronics, mentoring, and how to wear business socks with style.

Thanks goes out to all of the members of the Laboratory for Functional Optical imaging who played both large and small roles in shaping both this work and my time at Columbia: Cyrus Amoozegar, Clemence Bordier, Sean Burgess, Brenda Chen, Daniel Chow, Gali Galwaduge, Lauren Grosberg, Sharon Kim, Mariel Kozberg, Barbara L'Heureux, Angela Liu, Ying Ma, Addason McCaslin, Timothy J. Muldoon, Andrew Radosevich, Evelyn Ramirez, Sasha Rayshubskiy, Mohammed Shaik, Ryan Sun, Elsa Swanson, Venk Voleti, and Tim Weber.

My last thanks goes to my beautiful fiancé Kacey Ronaldson. Kacey saw me through the best of times and the worst of times. She made sure I saw this thing through to the end. Kacey is the love of my life, makes every day a hilarious, wondrous joy, and I am beyond excited to continue the rest of our lives together. I truly hit the jackpot.

Funding Sources

The work was funded in part by a NSF Graduate Research Fellowship and a Department of Defense National Defense Science and Engineering Graduate Fellowship.

Chapter 1 Introduction and Background

Imaging technologies have revolutionized biological sciences as well as clinical care. Whereas standard laboratory and clinical procedures necessarily damage and/or kill the tissue under study (i.e. histological sectioning), biomedical imaging techniques such as optical imaging, Magnetic Resonance Imaging (MRI), and Computed Tomography (CT) can often provide the same or more information non-invasively and non-destructively. In the case of the biosciences, this advantage allows biological systems to be studied as they are and as they develop natively *in-vivo*. In the case of clinical applications, this means less stress on the patient, improved recovery times, and a reduction in unnecessary surgical procedures.

Functional imaging techniques seek to study changes in physiology through measurements of dynamic systems such as blood flow and metabolism. Measurements of these systems provide insight into the current state of a complex biological system *in-vivo*. Functional optical imaging techniques are especially well-suited for functional imaging because they are minimally-invasive, use non-ionizing radiation, provide sub-cellular resolution, and derive contrast from a wide range of biological molecules. Contrast for specific and dynamic markers of *in-vivo* processes can be gained from modern transgenic labeling techniques, active and inactive exogenous agents, and intrinsic sources. Some optical imaging techniques can capture high-

information content wide-field 2-Dimensional (2D) images at high spatiotemporal resolutions. Other techniques provide high-resolution 3-dimensionally (3D) resolved images of living biological tissues, showing the structural and functional relationships between cellular structures at the base of biological systems.

A central challenge in building functional optical imaging systems is to acquire data at high enough spatial and temporal resolutions to be able to resolve the *in-vivo* process(es) under study. Conventional wide-field 2D multispectral imaging systems have limited spatiotemporal resolutions due to their imaging geometries, light source(s), and/or hardware implementations. Additionally, conventional wide-field 2D imaging systems are limited in the amount and types of contrast which can be employed simultaneously, reducing the number and types of physiological parameters which can be measured in a single experiment. 3D functional optical imaging technologies have largely been limited by slow volumetric scan rates. This has reduced the size of the scanned volumes in functional imaging experiments, shrinking the size and complexity of systems which can be studied study. This challenge is particularly highlighted within neuroscience where considerable effort in the field has focused on studying the structural and functional relationships within complete neurovascular units in the living brain. In this thesis we describe the design, construction, and application of novel 2D and 3D optical imaging systems to address this central challenge, with a specific focus on functional neuroimaging applications.

In Chapter 1 we introduce fundamental optical interactions with tissues, including absorption, fluorescence, and scattering (Section 1.1). Optical microscopy, including multispectral imaging and optical intrinsic signal imaging, is covered in Section 1.2. In Section 1.3 conventional approaches to volumetric optical imaging and their use within neuroscience are discussed.

In Chapter 2 we discuss the new high-speed, wide-field multispectral optical imaging system we developed which overcomes the temporal resolution and simultaneous contrast limits of conventional system designs, providing complete multispectral images 7.5 times faster than conventional systems. In Section 2.1 we describe the design and construction of two generations of our new high-speed, wide-field 2D multispectral imaging system design. In Section 2.2 we demonstrate three applications of our systems to in-vivo biomedical research and clinical neuroimaging studies.

In Chapter 3 we discuss an entirely new, high-speed, 3D fluorescence microscopy platform called Laser-Scanning Intersecting Plane Tomography (L-SIPT). L-SIPT uses a novel combination of light-sheet illumination and off-axis detection to provide *en-face* 3D imaging of samples at volumetric scan rates with a greater than 200-fold increase over conventional laser scanning microscopies. In Section 3.1 we cover the state of the art for volumetric optical imaging, including laser scanning microscopy, optical projection tomography, and the new light-sheet illumination geometries. In Section 3.2 we detail the design and construction of the L-SIPT system, covering the fundamental imaging concept of scanning and detecting fluorescence from an oblique illumination plane. In Section 3.3 we cover the development of initial imaging applications for L-SIPT.

1.1 Photon interactions

The optical properties of biological tissues are typically wavelength dependent and their differences provide one of the hallmark strengths of optical imaging: the incredible breadth and depth of tissue-specific contrasts available to image. Optical imaging uses electromagnetic radiation from the ultraviolet into the near-infrared spectrum (approximately 300 nm to approximately 1 μm). In this range light interacts with biological tissues largely through two processes: absorption and scattering (Figure 1). Fluorescence is a radiative process resulting from light absorption which causes molecular excitation into a radiative state. The relative rates of these processes are described by the tissue optical properties.

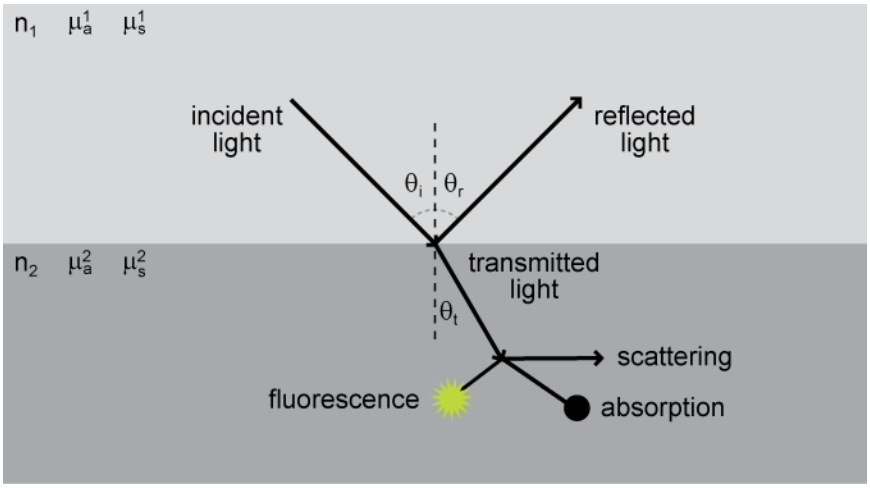

Figure 1: The major interactions of light with biological tissues. Optical imaging uses electromagnetic radiation from the UV (~300 nm) into the near-infrared (~1 μm) spectrum. In this range electromagnetic radiation is non-ionizing and interacts with biological tissues largely through two mechanisms: absorption and scattering. Fluorescence is a radiative process resulting from light absorption. Biological tissues are characterized by their wavelength-dependent optical properties whose differences provide a wealth of imaging contrasts.

1.1.1 Absorption

Absorption is the physical process whereby light is absorbed by a medium. The light's energy is transferred to the electrons of the medium's atoms and/or molecules moving them into an excited

state. After the photon's energy is absorbed, the molecule undergoes at least one of the following processes: non-radiative energy dissipation, radiative dissipation at thermal wavelengths, radiative dissipation through fluorescence, radiative dissipation through phosphorescence, and/or initiation of chemical reactions. See Section 1.1.2 for more information on fluorescence. The likelihood of these processes occurring depends on the wavelength of light (and therefore its energy) and the electronic structure of the medium. For light to be absorbed, its energy must exactly match the bandgap energy for an electron in the absorber to go from the ground state to an excited state (Figure 2A). Absorption is a probabilistic process, with the probability of absorption described by the medium's wavelength-dependent absorption coefficient, $\mu_a(\lambda)$, and properties of the illumination beam (e.g. wavelength, intensity, pulse duration). Linear and non-linear absorption processes are possible (Ed. Diaspro 2002). The absorption coefficient is an intrinsic source of contrast which provides a unique spectral signature to each absorber, or chromophore (Figure 2C). Absorption spectra provide a unique spectral signature intrinsic which can be imaged using multispectral imaging to quantitatively identify co-located chromophores. The imaging systems described in this thesis acquire ensemble measurements of large numbers of absorbers in living biological tissues. Therefore, we use physical models of ensemble absorption such as the Beer-Lambert law to model how light is absorbed by these tissues. See Section 1.2.4 for a more in-depth discussion of the Beer-Lambert Law. Here we provide a short introduction.

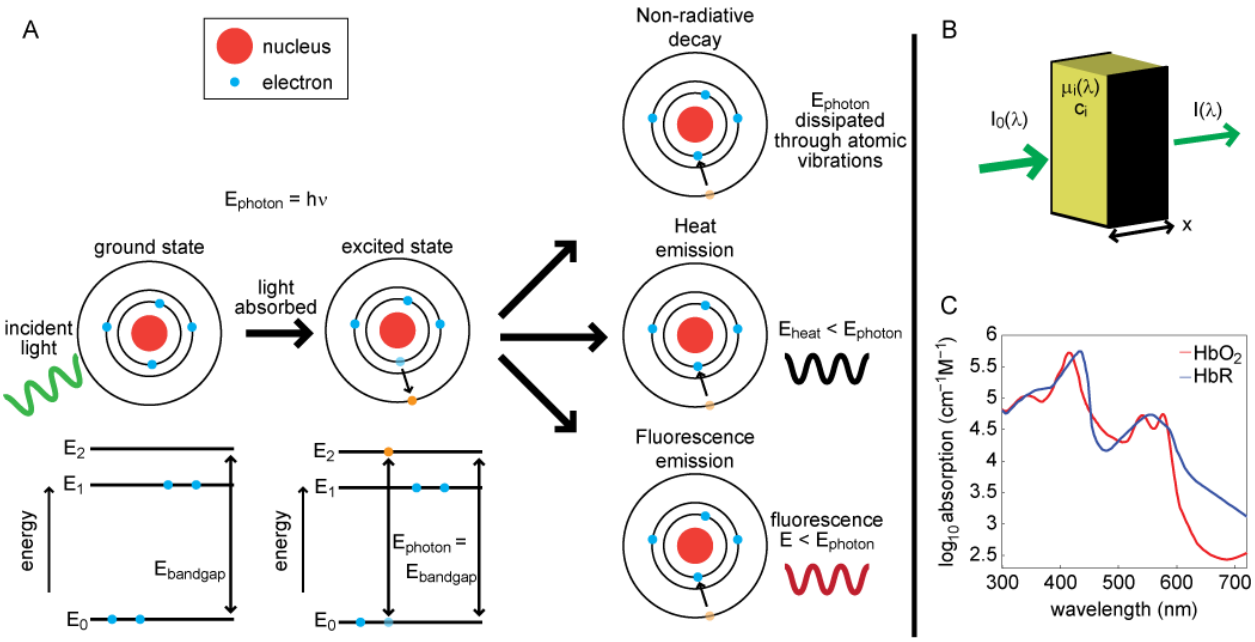

Figure 2: Light absorption. A.) Absorption of light is the process by which an atom or a molecule absorbs light energy. When light is absorbed an electron is excited from the ground state into an excited state at a higher energy level. The energy difference between the two states is equal to exactly the energy of absorbed photon (E_{photon}) which is related to the wavelength, or color, of the light. Once the atom or molecule is in the excited state the absorbed energy is eventually dissipated in some way to return the atom or molecule back to the ground state. Three candidate mechanisms are shown but are not inclusive: non-radiative decay, emission via long heat wavelengths, and fluorescence emission. B.) The Beer-Lambert Law models the absorption of light by large numbers of atomic molecules. It provides a simple, yet powerful, method to identify and measure the concentrations of chromophores in an absorbing medium. The amount of light absorbed is a function of the absorption properties of the medium and its concentrations. C.) Example absorption spectra for oxygenated (HbO_2) and deoxygenated hemoglobin (HbR), two of the most important chromophores in the brain.

The Beer-Lambert Law for ensemble absorption in non-scattering media

The Beer-Lambert law (1) relates the amount of light energy entering and leaving an absorbing medium (in the absence of scattering):

$$I = I_0 e^{-\mu_a x} \qquad (1)$$

where I_0 is the light intensity entering the medium (in units of energy per area per time), I is the light intensity leaving the medium, μ_a is the medium's absorption coefficient (units of absorption events per distance), and x is the distance traveled through the medium (referred to as the

pathlength) (Figure 2B). As the distance traveled in the medium increases, - or the absorption coefficient of the medium increases, - the amount of light absorbed will increase. The absorption coefficient is described by the wavelength-dependent physical properties of the medium and the concentration of the absorbers within medium. For a medium composed of N homogenously mixed chromophores:

$$\mu_a(\lambda) = \sum_{1}^{N} \varepsilon_i(\lambda) c_i \qquad (2)$$

where $\varepsilon_i(\lambda)$ is extinction coefficient spectra and c_i are the molar concentrations of the chromophores. The inverse of $\mu_a(\lambda)$ is called the penetration depth, and is the distance traveled into the medium where $^1/_e$ of the original light energy remains. Extinction coefficient spectra are known *a priori* to imaging and can be determined using the Beer-Lambert Law (Prahl 1999). Imaging applications of modified versions of the Beer-Lambert Law typically seek to determine chromophore concentration (Hillman 2007). The absorbance of a medium is given by:

$$A(\lambda) = -ln\left(\frac{I}{I_0}\right) = x \sum_{1}^{N} \varepsilon_i(\lambda) c_i \qquad (3)$$

Time-dependent changes in chromophore concentration (Δc_i) can be determined from measurements of changing absorbance (ΔA):

$$\Delta A(\lambda) = -ln\left(\frac{\Delta I}{I_0}\right) = x \sum_{1}^{N} \varepsilon_i(\lambda) \Delta c_i \qquad (4)$$

For media with N absorbers with distinct absorption spectra, N - 1 distinct wavelengths at minimum are required to calculate chromophore concentrations (Lansford et al. 2001, Bouchard et al. 2007). Care must be taken when selecting measurement wavelengths such that the chromophores have distinct absorption coefficient values at each wavelength, otherwise it is impossible to solve for distinct chromophore concentrations. Solving the systems of equations generated by these spectral measurements is known as spectral unmixing (Lansford et al. 2001, Levenson and Mansfield 2006). However, biological tissues are typically highly scattering (See Section 1.1.3 for more information on scattering). Modifications to the Beer-Lambert Law to take into account the increase in pathlength due to scattering are discussed in Section 1.2.4.

1.1.2 Fluorescence

Fluorescence is the process through which light is absorbed by an atom or a molecule and then light is later emitted by the fluorophore (the absorbing atom or molecule). Fluorescence begins with the absorption of a photon which causes an electron to transition to a higher energy level. This first half of the process is termed excitation. After some time the electron returns to its ground state energy level and a second photon is emitted (Figure 3A). Non-radiative losses in energy are possible during this time. This second half of the process is termed emission. The Jablonksi diagrams in Figure 3A depict this process. Fluorescence of biological fluorophores commonly occurs on the order of nanoseconds; the same electronic process is termed phosphorescence when it is on longer timescales. The absorbed light is termed excitation light while the emitted light is termed emission light. In most cases the energy of the absorbed photon is exactly equal to the bandgap energy between the ground and excited states of the electron.

This is known as linear absorption. A photon's energy (E_{photon}) is related to its wavelength via the following equation:

$$E_{photon} = \frac{hc}{\lambda} \quad (5)$$

where h is Planck's constant, c is the speed of light in a vacuum, and λ is the photon's wavelength. Due to non-radiative energy losses while the electron is in the excited state, the emitted photon is typically of lower energy and therefore a longer wavelength. This shift in photon wavelength is called the Stokes' Shift (Figure 3B). Non-linear absorption is possible where the intensity of the excitation light is very high or the absorbing medium has non-linear optical properties (Ed. Diaspro 2002) (Figure 3C). In the case of high excitation light intensity there is a non-zero probability that an atom or molecule will absorb two photons whose individual energies are half the bandgap energy. When this occurs, the electron transitions to an excited state and then later emits a photon when the electron returns to the ground state (Goeppert-Mayer 1931). In this case the Stokes' Shift is reversed and the emission photon is typically at a higher energy and shorter wavelength than the excitation photons. Non-linear absorption and fluorescence is termed two photon fluorescence and its advantages for biological imaging have revolutionized optical imaging in neuroscience (Section 1.3.2).

Typically a range of electronic transitions with closely spaced energy bandgaps are possible for fluorophores. However, not all energy transitions are equally probable. These properties result in what are termed fluorescence excitation and emission spectra which show the relative probabilities as a function of wavelength for photon absorption and photon emission, respectively (Figure 3B). Fluorescence spectra provide an identifying fingerprint for each fluorophore and can be distinguished using spectral imaging techniques (Section 1.2.3 for more

detail). Measurements tracking the amplitude of a fluorescent signal can be used as direct measurements of the amount of fluorophore present in a medium. Spectrally resolved measurements can provide information about amounts of multiple, co-located fluorophores (Levenson and Mansfield 2006, Radosevich et al. 2008, Grosberg et al. 2011).

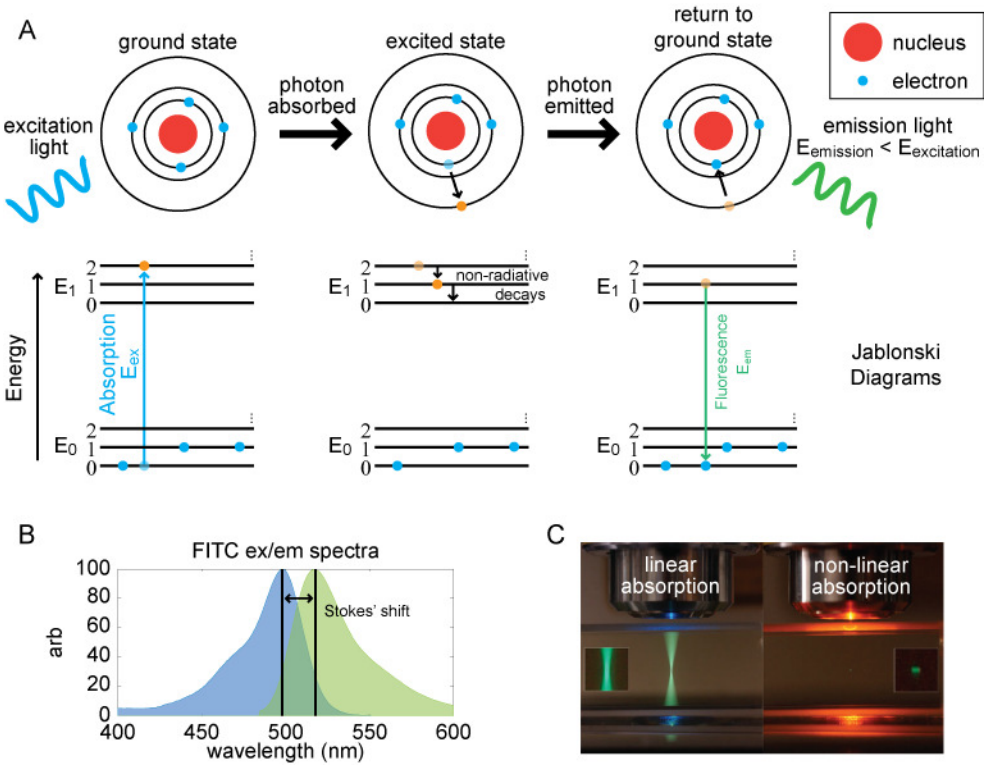

Figure 3: Fluorescence. A.) Fluorescence is the process by which light is absorbed by an atom or molecule which then emits light at a later time. When light is absorbed an electron transitions to a higher energy level, placing the fluorophore in an excited state. After non-radiative decays, light is emitted by the fluorophore at a longer wavelength than the excitation light, reflecting the non-radiative loss of energy. B.) Fluorescence excitation and emission spectra detail the relative probabilities of electronic transitions as a function of wavelength. Fluorescence spectra provide an identifying fingerprint for each fluorophore. C.) Linear vs. non-linear absorption leads to unique fluorescence properties. Under linear absorption there is an equal probability of fluorescence at the same excitation light intensity. Under non-linear absorption, the probability of fluorescence is very low and increases with the square of the excitation intensity. Image adapted from (Ruzin and Aaron 2013).

Important properties of fluorophores:

Every photon which is absorbed by a fluorophore does not lead to fluorescence emission. The ratio of the number of emitted photons to the number of absorbed photons is termed the quantum yield (Φ) of the fluorophore:

$$\Phi = \frac{number\ of\ emitted\ photons}{number\ of\ absorbed\ photons} \quad (6)$$

The quantum yield is an important measurement relating the effectiveness of fluorophores to produce a fluorescent signal. Many biological imaging experiments are termed "photon starved" in that fluorophores typically emit weak signals which are difficult to detect. Where possible, experiments can be optimized by choosing fluorophores with the highest quantum yield which match the required spectral properties of the experiment.

The amount of time between photon absorption and photon emission is termed the fluorescence lifetime (τ). The fluorescence lifetime is a probabilistic process unique to the electronic structure of each fluorophore and provides an identifying fingerprint. It is measured with time resolved measurements of fluorescence signal intensity. The lifetime provides information about the electronic environment of the molecule and can also provide measurements of the concentrations of multiple fluorophores in the same location and the distances between pairs of fluorophores using fluorescence resonance energy transfer (FRET) imaging (van Munster and Gadella 2005). FRET is also known as Forster resonance energy transfer in some publications. The kinetics of excited fluorophores can be described as a first order process which relates the number of excited fluorophores as a function of time immediately following excitation (t = 0):

$$[S] = [S_{t=0}]e^{-t/\tau} \quad (7)$$

Where [S] is the concentration of excited fluorophores, $[S_{t=0}]$ the concentration of excited fluorophores at t = 0, and t is the time after excitation. The fluorescence lifetime is defined by the amount of time it takes for $^1/_e$ % of the excited molecules to emit a photon.

Intrinsic vs. exogenous sources of fluorescence:

Many natural molecules vitally important to biological systems are also fluorophores, such as NADH, FAD, and hemoglobin. These molecules are termed intrinsic fluorophores, and their experimental power within biological imaging is exploited to image biological systems in their native environments with minimal perturbations (Ranji et al. 2006, Mayevsky and Chance 2007, Radosevich et al. 2008, Grosberg et al. 2011). However, there still remains a need for fluorophores which can label specific tissue structures, provide active measures of changing molecule concentrations *in-vivo*, and report physiologically important information such as the partial pressure of oxygen in tissues (Kazmi et al. 2013). Exogenous fluorophores are molecules not native to biological systems which fill this need. These molecules can be used found in nature or engineered for their specific biological purposes. Their fluorescence excitation and emission spectra can be engineered for specific applications and they can be engineered to label highly specific tissue structures. They can be used to image samples *in-vivo* and *in-vitro*. However, exogenous fluorophores can be toxic to living biological systems, provide non-specific labeling of tissues, and can be difficult to introduce to biological systems without significant experimental difficulties (Bouchard et al. 2009).

More recently genetic sources of fluorescence have been harnessed to provide a cross between the strengths of intrinsic and exogenous fluorophores (Chalfie et al. 1994). Genetic

sources of fluorescence can be used for highly specific labeling of biological tissues (Livet et al. 2007) and provide active sources of contrast which reflect changing concentrations of physiological important atoms and molecules while remaining non-toxic to biological tissues (Akerboom et al. 2012). Genetic sources can be introduced into biological systems via crosses with transgenic animals or via viral delivery vectors. Due to their relatively recent introduction to the biological sciences, genetic sources of fluorescence remain the focus of intense research and engineering to improve their quantum yields, spectral properties, and functional response times when used as active probes (Akerboom et al. 2012, Cai et al. 2013).

1.1.3 Scattering

Scattering is the process by which light changes direction after interacting with an object. Scattering can be elastic (no loss of photon energy) or inelastic (a loss of photon energy and change in wavelength, and therefore color). Both types of scattering can be used as a source of contrast in optical imaging. Scattering occurs on multiple length scales, from light-particle interactions where the particles are approximately the same size as the light's wavelength, up to objects many times the wavelength such as drops of water. There are multiple physical models of light scattering, with a full solution to scattering only given by analytical solutions of Maxwell's Equations which are only found for specific, highly controlled situations. The ratio of the particle size to the wavelength determines which type of scattering dominates (Chaney 2013). General solutions to scattering problems use discretization and computational solution methods for arbitrary geometries.

The amount of scattering caused by a tissue can be described by its scattering coefficient, μ_s, which has units of scattering events per distance. The inverse of the scattering coefficient tells how far on average a photon will travel into a medium (the mean free path) before being scattered and is given by the scattering cross section (how large the particle appears to the light) multiplied by the medium's particle density (Jacques and Prahl 1998). The dimensionless anisotropy factor, g, gives the probability that a scattered particle will continue in the same direction it was travelling before being scattered. g has values from [-1 1] with -1 indicating direct backscatter, 1 indicating direct forward scatter, and 0 indicating isotropic scattering. g is determined from the specific scattering phase function which describes the medium (Jacques and Prahl 1998). The reduced scattering coefficient, μ_s' is important when the probability of scattering is much larger than the probability of absorption events (known as the diffusive transport regime) (Jacques and Prahl 1998). μ_s' is given by:

$$\mu_s' = \mu_s(1 - g) \tag{8}$$

μ_s' is important to photon transport models because it models multiple direction-oriented steps described by the mean free path as a single isotropically scattered step, a model which provides a good approximation to photon transport through large biological tissues (Jacques and Prahl 1998, 2002). The inverse of μ_s' is known as the reduced mean free path. In tissues where absorption events are equally likely as scattering events more complex photon propagation models are used, such as the Equation of Radiative Transport (Klose and Hielscher 1999). Depending on the imaging geometry modifications to the mean pathlength factor are made. Within biological tissues photons experience a relatively high rate of scattering, making it difficult for focused light to propagate through tissue undisturbed. This is one of the central challenges volumetric

optical imaging techniques must overcome to image in 3D. Spatial apertures (confocal microscopy), non-linear absorption processes (two photon fluorescence), computed tomography reconstructions (Optical Projection Tomography), and novel light delivery methods (light-sheet illumination) all have been developed partially with the goal of minimizing the effects of scattering to produce spatially resolved images at depths in biological samples.

1.2 Optical Microscopy

Optical microscopy has been a central tool for the biosciences since its first recorded invention in 1590 by the Janssen brothers. The first published application of microscopy was Robert Hooke's study of cork cells (1667) and the first published use of microscopy to image biological samples was performed by Anton von Leewenhoek to image and describe bacteria, yeast, and blood flow in capillaries (1675) (AB 2013). Since its early days, optical microscopy has been used extensively due to its ability to provide high resolution images at low cost and with relatively simple equipment. Additionally, optical imaging is able to employ an unparalleled range of contrast agents (both naturally occurring and man-made) to label biological tissues *in-vivo*, *in-vitro*, and *ex vivo* providing structural, functional, and disease state information with high tissue specificity. High-speed, high resolution imaging can reveal dynamic events such as changes in blood flow and responses to external stimulation.

The most common, and experimentally simple, optical imaging techniques are camera based wide-field imaging methods which illuminate samples with light and measure scattered and/or transmitted light. While these techniques provide high resolution images, they suffer from resolution and signal to noise losses when the sample in greater than 5 μm thick because biological tissues are typically highly scattering at visible wavelengths. Additionally these techniques require samples to be fixed and mechanically sliced into thin sections, necessarily precluding *in-vivo* studies. Multispectral wide-field imaging (the acquisition of spectrally resolved images of a sample) can provide spectroscopic information to allow quantitative analysis of multiple absorbers and/or fluorophores in parallel. Beyond these neuroscience-directed applications discussed in Section 1.2.2, the same wide-field multispectral and fluorescence imaging systems can be valuable for clinical applications such as characterizing the

structure and function of a broad range of tissues including cervix, retina, oral mucosa, gastric tissues, the heart, internal organs during surgery and skin (Svanberg et al. 1998, Lawlor et al. 2002, Zemlin et al. 2008, Themelis et al. 2009, Troyan et al. 2009, Rahman et al. 2010), and for basic research applications such as small animal molecular imaging (Rudin and Weissleder 2003, Levenson and Mansfield 2006, Hillman and Moore 2007). However, common implementations of wide-field multispectral imaging suffer from slow image acquisition speeds due to typical system designs, limiting their use to imaging relatively slow dynamic events *in-vivo*.

1.2.1 Fundamentals of optical microscopy

This section provides an overview of concepts important to modeling and constructing 2D optical microscopy systems. Geometrical optics, the definition of spatial resolution, and basic components of optical microscopes are discussed. Please refer to (Hecht 2001, Murphy 2001) for more in-depth information.

Geometrical optics: a first approximation for modeling optical systems

Geometrical optics models light propagation as "rays" which travel in straight lines until they encounter an optical element (for example, a lens or mirror). Optical elements are defined by the specific deviations to ray paths they impart, each governed by specific rules. Geometrical optics is used as a first approximation for placement of optical elements and for determining object and image positions for arbitrary optical systems. Certain types of optical aberrations (malformations of images due to non-ideal optical surfaces) can be modeled.

The optical axis is an imaginary line which passes through the rotational center of a lens element. In the case of a mirror the optical axis is normal to the mirror's surface. In the case of a lens the optical axis passes through the center of the lens such that it is rotationally symmetric.

Mirrors follow the Law of Reflection which states that a ray reflected by a surface has the same angle of reflection as its angle of incidence (Figure 4). Stated another way, the reflected ray leaves the mirror surface at the same angle relative to the normal that it was incident on.

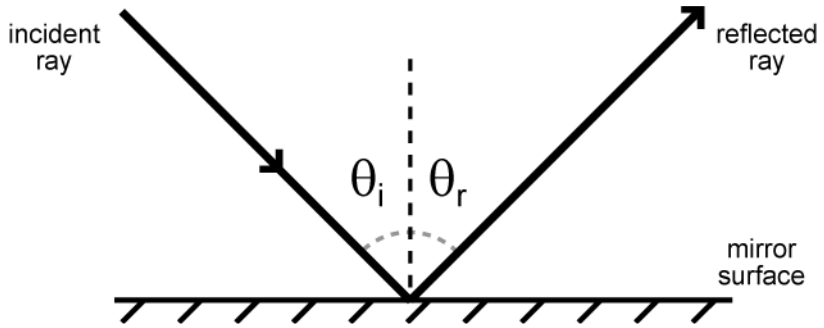

Figure 4: Mirror. Mirrors follow the Law of Reflection which states that the angle of incidence θ_i is equal to the angle of reflection θ_r.

A lens is an optical element which uses refraction to focus or defocus light. Lenses are made from various materials whose indexes of refraction are different from air. Lenses can be described geometrically as thin lenses and thick lenses. Thin lenses are modeled using the well-known Lensmakers' Equation which relates the object distance (x_o), the image distance (x_i), and the lens focal length, f:

$$\frac{1}{x_o} + \frac{1}{x_i} = \frac{1}{f} \tag{9}$$

When drawing rays interacting with thin lenses, three rules are followed (Figure 5):

1. A ray traveling parallel to the lens' optical axis will be deviated by the lens such that it passes through the focal point on the opposite side of the lens.
2. A ray traveling through the center of the lens travels straight.

3. A ray passing through the front focal point will be deviated such that it travels parallel to the lens' optical axis after the lens.

These three rules can be used as a first approximation to determine object and image locations in any lens based optical system. ABCD matrices can be used for a mathematical version of these rules (BYU-optics-lab 2009).

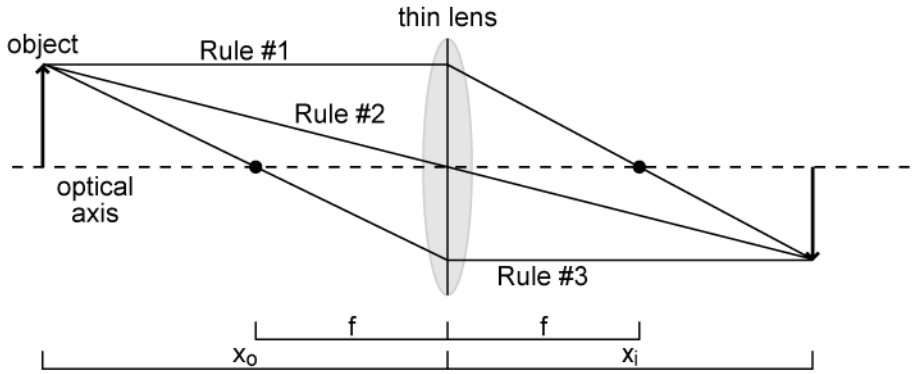

Figure 5: Three rules of geometrical raytracing for thin lenses.

The Thin Lens equation is not able to model optical aberrations from non-ideal optical surfaces. The Thick Lens equation takes into account the physical size and shape of lens surfaces and the physical properties of the materials used to make the lens. Refraction is the physical process by which light traveling from one medium to another will be deviated if the two media have differing indexes of refraction. The index of refraction is the ratio between the speed of light in a vacuum and the speed of light in a media. Light traveling from a medium with a lower index of refraction to one with a higher one will be deviated toward the normal of the interface between the two media (Figure 6). Snell's Law tells us by how much the light ray will be deviated when traveling through the interface:

$$n_1 \sin(\theta_1) = n_2 \sin(\theta_2) \quad (10)$$

where n_i is the index of refraction for medium i and θ_i is the angle of the ray relative to the surface normal between the two media for medium i (Figure 6). When modeling lenses as thick lenses the radii of each lens surface, the distance between surfaces, and the indexes of refraction for lens materials are known. Snell's Law is used to calculate the outgoing angle of the ray at each lens surface. Computer software packages can be written to model arbitrary optical systems (Section 3.2.2).

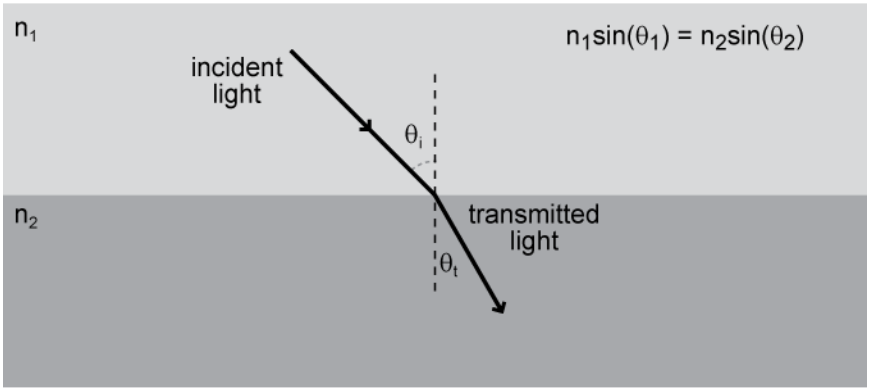

Figure 6: Snell's Law. Snell's Law describes the relationship between the angle of incidence and the angle of transmission for a light ray traveling between media with different indexes of refraction. Refraction occurs at the interface because the speed of light is different between the media causing waves of light to bend.

Typical lenses (known as spherical lenses) are rotationally symmetric about the optical axis: a light ray incident on the lens surface parallel to the optical axis will be focused to a single focal point in space regardless of where the ray intersects the lens. This occurs because spherical lenses focus light along both spatial axes transverse to the optical axis. A cylindrical lens, in contrast, is not rotationally symmetric and focuses light only along a single transverse axis such that a single focal point does not exist for the lens but instead a focus line will be created. See Section 1.3.2 for more information on the types of images created with a cylindrical lens.

Optical aberrations are deviations from ideal performance in real optical systems. Aberrations reduce imaging performance through a loss in resolution and contrast. Lens

aberrations can be modeled to a first approximation using the thick lens approximation and geometrical raytracing.

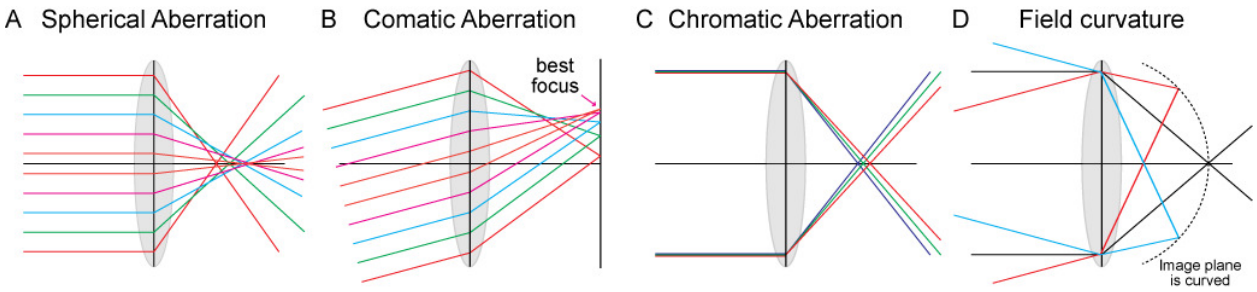

Figure 7: Optical Aberrations. A.) Spherical aberration. B.) Comatic aberration. C.) Chromatic aberration. D.) Field curvature. False colors provided to make tracing individual rays easier in A.), B.), and D.).

Spherical aberrations are the result of using spherical surfaces to create a lens (ideal lens surfaces would be aspheric). Rays which intersect the lens' surface at different radial distances from the optical axis are focused to different points on the optical axis because they experience different refractive power of the lens (Figure 7A). This results in a bright image symmetrically surrounded by a blurred image with interference rings.

Comatic aberrations result from rays intersecting a lens at an angle not parallel to the optical axis (Figure 7B). This situation is commonly encountered when the object is not on or near the optical axis. Rays which enter the lens at different radial distances are focused to different locations on the optical axis, creating a "comet-like" effect where a bright image is surrounded by a hazy image which gets larger along a single axis. Field curvature is the same aberration as coma except the object has extremes on either side of the optical axis. In this case, the edges of the object focus to planes closer to the lens than points located on the center of the object (Figure 7D). Modern lenses correct for field curvature by changing lens focusing power as a function of radial distance.

Chromatic aberrations result from the wavelength dependence of common optical glasses used to make lenses (Figure 7C). The index of refraction partially determines by how much a ray is deviated when it interacts with a lens surface. Lens radii are designed to focus/defocus light to certain positions along their optical axis and are fixed for a given lens. Different index of refraction for different wavelengths results in rays being deviated through different angles, thus causing light of different wavelengths to be focused to different locations. Stacking two lenses together, known as an achromatic doublet, can correct chromatic aberration across the visible spectrum.

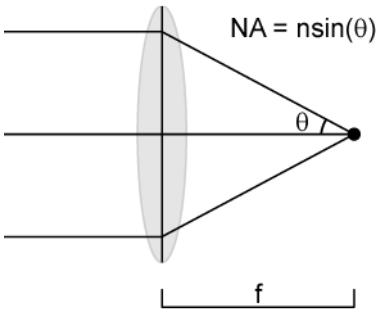

Figure 8: Numerical aperture (NA) for a lens. The NA for a lens is one its most important properties. Knowledge of a lens' NA directly provides information on the minimum size of an object resolvable with the lens

The numerical aperture (NA) of a lens defines the range of angles of light it can collect (Figure 8). The NA is one of the most important parameters of any lens as it directly relates to the lens' spatial resolution. Planar light incident on the circular aperture of a spherical lens is focused to a point. Diffraction limits the minimum size and features of this point and, in the ideal case, is described by an Airy disk. The Airy disk is a circularly symmetric diffraction pattern described by a central bright region surrounded by alternating rings of light and darkness. The rings are created by constructive and destructive interference. The Rayleigh Criterion is one definition of spatial resolution which states that the minimum resolvable size for a lens is the distance between the center of one Airy disk and the first dark ring of the disk (Murphy 2001).

The Rayleigh Criterion is an arbitrary definition of spatial resolution but it is the best accepted. This distance, d, can be calculated from:

$$d = \frac{0.61\lambda}{NA} \quad (11)$$

where λ is the wavelength of the light and NA is the numerical aperture. Objects smaller than d appear as Airy disks. Non-ideal optical systems will have d values larger than (11). The minimum resolvable distance for a given optical system is also known as the system's point spread function (PSF).

Basic components of optical systems

Optical systems are constructed from a wide variety of optical elements such as mirrors, lenses, optical filters, beamsplitters, and more exotic elements such as non-linear crystals. Optical filters are optical devices which selectively pass or reject specific wavelengths of bands of wavelengths of light. Shortpass filters are filters which pass light below a "cut-off" wavelength, longpass filters are filters which pass light above a "cut-on" wavelength, and bandpass filters are filters which pass a specific band of wavelengths. Shortpass and longpass filters are used to separate excitation from emission light when fluorescence is performed while bandpass filters are typically used to select specific bands from broadband light sources or broad fluorescence emission sources. An additional type of filter is known as a neutral density filter which in the ideal case reduces the amplitude of all wavelengths equally. The units of neutral density are in powers of 10 such that a neutral density filter with an optical density of 2 reduces intensity by a factor of 10^{-2}.

Beamsplitters are optical devices which spatially separate different components of a beam of light. Dichroic beamsplitters separate beams of light based on wavelength. Longpass dichroic beamsplitters transmit light above a "cut-on" wavelength and reflect light below this wavelength. Shortpass dichroic beamsplitters do the opposite. Polarizing beamsplitters separate light based on its polarization and can be used to filter polarized from unpolarized light. Amplitude beamsplitters exist as well which separate light into two beams with different amounts of power (i.e. 50/50 or 70/30 separation of optical power).

1.2.2 Optical imaging in neuroscience: OISI

In response to almost any stimulus (for example somatosensory and visual stimuli), discrete regions of the brain will experience an increase in blood flow (Figure 10A). It is this hemodynamic response that provides a signal that can be measured via functional magnetic resonance imaging (fMRI) (Kwong et al. 1992). In 1986 Grinvald et al. demonstrated that these changes in blood flow could be detected by simply imaging the exposed cortex under optical illumination using a photodiode array (Grinvald et al. 1986). This initial observation led to the field of "Optical Intrinsic Signal Imaging" (OISI) which uses wide-field 2D multispectral imaging techniques to provide dynamic measurements of blood flow and tissue oxygenation states in the cortex *in-vivo*. Within the cortex, "optical intrinsic signals" correspond to changes in reflected light intensity due to changes in the concentration of the two main absorbers in the brain: oxy- and deoxyhemoglobin (HbO_2 and HbR, respectively) (Hillman 2007). The dynamic behavior of the two oxygenation states of hemoglobin can be measured because they have distinct absorption spectra (Figure 9). Through images of the cortex under carefully selected

illumination wavelengths and image analysis using physical models of photon propagation, wide-field 2D multispectral absorption imaging can provide dynamic maps of hemoglobin concentrations, tissue oxygenation, oxygen consumption, and changes in blood flow (Hillman 2007, Bouchard et al. 2009, Chen et al. 2011).

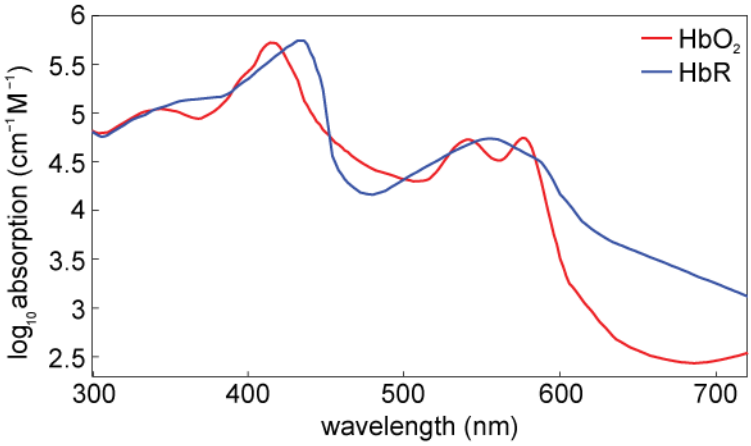

Figure 9: Hemoglobin absorption spectra. Oxygenated (HbO_2) and deoxygenated hemoglobin (HbR) have different absorption spectra allowing their relative concentrations to be measured with multispectral absorption imaging technologies. Changes in hemoglobin concentrations in the cortex comprise "optical intrinsic signals" within neuroscience.

Mapping these changes in blood flow has significantly improved our understanding of the way the brain organizes and processes information (Tso et al. 1990, Owen et al. 1998, Fox et al. 2005). Since 1986, improvements in digital camera technology, light sources, and optical filters have led to widespread use of so-called 'optical intrinsic signal imaging' (OISI) for neuroscience research (Blood et al. 2002, Pouratian et al. 2002, Devor et al. 2003, Vanzetta et al. 2005, Bouchard et al. 2009, Lu et al. 2009, Chen et al. 2011, Kozberg et al. 2013, Rayshubskiy et al. 2013). In most implementations, OISI acquires multispectral image sets of the brain and calculates changing hemoglobin concentrations and brain oxygenation using spectral unmixing techniques (Figure 10B). Acquired at fast enough image acquisition rates, such measurements

can provide local estimates of changing brain oxygenation state, blood flow, and vessel dilation dynamics from direct tracking of hemoglobin.

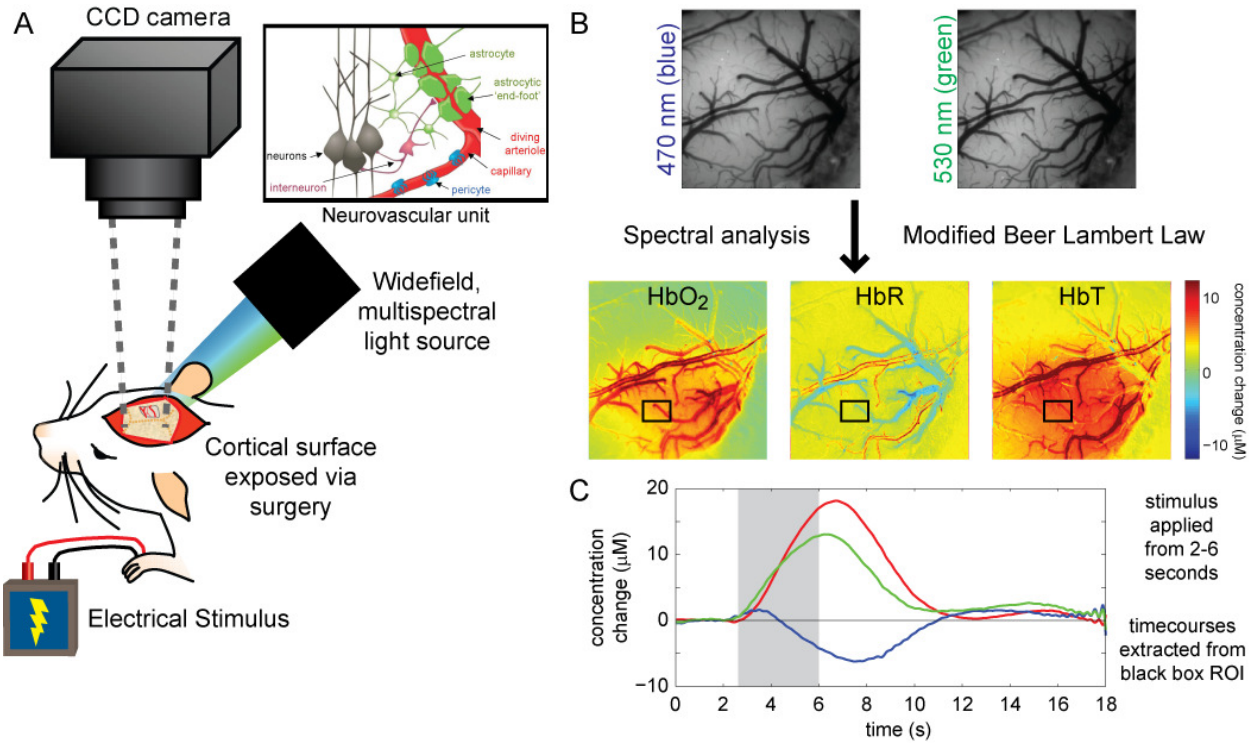

Figure 10: Optical Intrinsic Signal Imaging (OISI) experiment overview. A.) OISI imaging in rodents is accomplished by thinning or removing the skull under surgical anesthesia. A multispectral light source is used to illuminate the exposed brain tissue. A camera is used to acquire images of the cortex under changing illumination wavelengths. OISI can be used to study the morphological and functional interactions between the cells which comprise the neurovascular unit. B.) Example raw images under 470 nm illumination (left) and 530 nm illumination (right) comprise a multispectral image set. These component images are sensitive to different oxygenation states of hemoglobin. Spectral analysis can be used to calculate changes in hemoglobin concentration. C.) Example concentration change timecourse extracted from ROI shown in black box in hemoglobin maps from B.). Electrical forepaw somatosensory stimulus was applied from 2 to 6 seconds at 3 Hz with a 3 ms stimulus width and 1.0 ± 0.1 mA stimulus amplitude. (inset) adapted from (Gordon et al. 2007)

To gain a full understanding of the interplay between the brain's hemodynamic and neuronal systems in the evolution the hemodynamic response, OISI measurements must be supplemented with measurements of the activity of the brain's neuronal systems. A range of exogenous and intrinsic sources of contrast have been developed and deployed within the brain *in-vivo* in an attempt to solve this problem. Fluorescence imaging of exogenous voltage sensitive dyes (VSDs)

can be used to show neuronal activity on millisecond timescales across wide areas of the brain (Shoham et al. 1999, Peterka et al. 2011, Mohajerani et al. 2013). VSDs are designed to report changes in membrane electrical potential via a variety of molecular mechanisms ranging from Fluorescence Resonance Energy Transfer (FRET) quenching to electrochromic modification of fluorophore electron energy levels (Peterka et al. 2011). Other dyes sensitive to intracellular calcium concentration changes can be imaged to study the activity of neurons and astrocytes (Dani et al. 1992, Bouchard et al. 2009). More recently genetically encoded calcium indicators have been developed which place engineered Green Fluorescent Protein (GFP) molecules in the membranes of neurons (Akerboom et al. 2012). Known as GCaMP, the modified GFP molecule is fused to calmodulin in such a way that when calcium ions are present the GFP molecule is highly fluorescent while in the absence of calcium the GFP/calmodulin structure moves into a conformation where GFP fluorescence is reduced. GCaMP molecules can be introduced through viral transfections or crosses of transgenic animals. The power of the GCaMP molecules lies in the high signal-to-noise between calcium bound and calcium free states, highly specific labeling of specific cell types (individual classes of neurons can be labeled), and the relatively low photobleaching rates of GCaMP compared to common exogenous calcium indicator dyes (Akerboom et al. 2012). OISI imaging performed simultaneously with these active probes can provide insight into the functional and baseline interactions between the brain's hemodynamic and nervous systems on length scales ranging from individual cells to entire neuronal and hemodynamic networks.

However, while multispectral wide-field 2D imaging technology has made significant improvements since Grinvald's 1986 demonstration, applications of OISI and fluorescence imaging have largely been limited to studying relatively slow *in-vivo* processes or fast *in-vivo*

processes with poor spatial resolution. Wide-field multispectral imaging systems have largely been limited to approximately 5 multispectral frames per second, while common 3D volumetric optical imaging systems- such as confocal and two photon microscopy- have been limited to single plane depth-resolved imaging at video rates. To study faster dynamic *in-vivo* processes, such as measuring the velocity of blood flow from tracking individual red blood cells, vessel dilation dynamics, and neuronal signaling, it is necessary to improve the temporal resolution of OISI systems.

1.2.3 Multispectral imaging

Multispectral imaging encompasses any optical imaging technique which acquires images under varying spectral conditions and uses mathematical models of light propagation to provide spatially resolved maps of relative amounts of contrast sources. These conditions can include varying illumination wavelengths to measure reflectance signals (contrast from chromophores), fluorescence excitation wavelengths to measure fluorescence amplitude signals (contrast from fluorophores), and fluorescence emission wavelengths to measure fluorescence amplitude signals (contrast from fluorophores) (Figure 11). Multispectral imaging can be performed in wide-field imaging geometries and in laser-scanning imaging geometries. In wide-field functional optical imaging systems, multispectral imaging is typically accomplished by modulating the wavelength of the illumination light and detecting changes in absorption (via reflectance intensity) and/or fluorescence by a digital camera. A set of component images of the sample acquired under different illumination wavelengths constitutes a single multispectral image (Figure 11). Mathematical analysis of the component images acquired over time based on photon propagation

models for the imaging geometry and the measured photon/tissue interaction(s) provides maps of the changing concentration of the contrast agent (Lansford et al. 2001, Levenson and Mansfield 2006, Bouchard et al. 2007, Radosevich et al. 2008, Grosberg et al. 2011). For example, in the case where spectrally resolved images of fluorescence emission spectra are acquired, the summed intensity at a given pixel (i, j) in the image is given by weighted sum of the emission spectra of the fluorophores present in the pixel (Figure 11A-B):

$$I_{em\,i,j}(\lambda) = c_1 A_1(\lambda) + c_2 A_2(\lambda) + \ldots \quad (12)$$

Where c_k are the concentration of fluorophore k, and $A_k(\lambda)$, etc. are the normalized fluorescence response spectra for fluorophore. Typically, the c_k's are solved for to provide a quantitative measurement of the amount of each fluorophore present. Common solution algorithms force the c_k's to sum to 1 for physiological considerations and to enable comparisons between spectral component images, therefore it is important to know a priori the fluorophores expected in an image (Bouchard et al. 2007). To perform this calculation, N spectral images must be acquired for N co-located fluorophores. In situations where not all of the $A_i(\lambda)$'s are known *a priori*, spectral subtraction methods can be used to determine spectral shapes (Bouchard et al. 2007). Acquisition of spectrally resolved images over time provides maps of changing fluorophore concentrations even when the fluorophores are located within the same pixel.

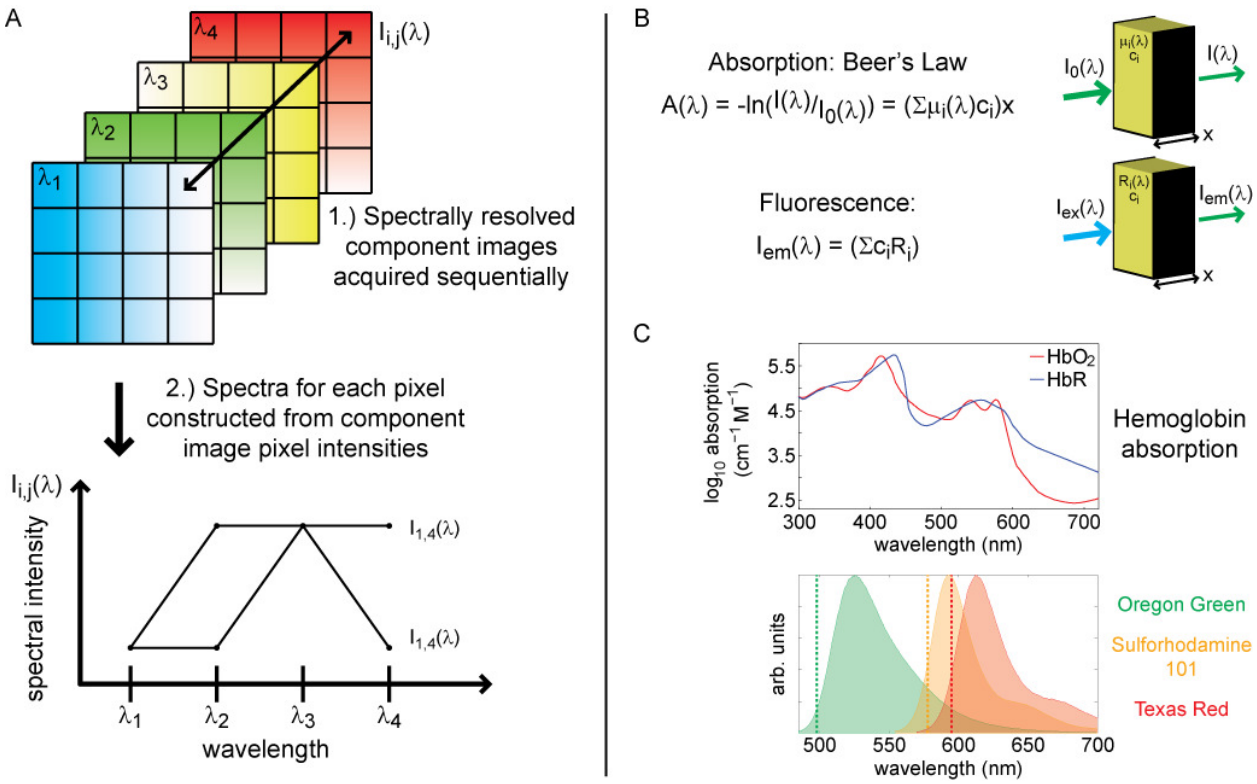

Figure 11: Multispectral imaging. A.) Multispectral images are constructed from a set of component images acquired under varying spectral conditions. Each pixel in a multispectral image contains a unique spectrum which is created by the sum of the spectra of sources of contrast co-located within the pixel. B.) Photon propagation models are used to calculate the concentration of sources of contrast within each pixel. C.) Absorption spectra and fluorescence spectra are known *a priori* to imaging and used as inputs to photon propagation models. Figure adapted from (Lansford et al. 2001).

OISI is a common use of multispectral imaging in neuroscience and involves multispectral absorption imaging of the oxygenation state of hemoglobin in the exposed cortex (Tso et al. 1990, Owen et al. 1998, Blood et al. 2002, Fox et al. 2005). The most common absorption model is the modified Beer-Lambert law which produces a system of equations which can be solved using spectral unmixing techniques (see Section 1.2.4 for a detailed discussion of this law) (Hillman 2007). The two oxygenation states of hemoglobin (oxy- and deoxyhemoglobin) have different optical absorption spectra which can be selectively measured by careful choice of illumination wavelength (Figure 9). Multispectral absorption imaging combined with active fluorophores sensitive to intracellular calcium concentrations can be used

to provide measurements of functional interactions between the vascular system and nervous system cells such as neurons and astrocytes potentially leading to a deeper understanding of the physiological mechanisms underlying the hemodynamic response (Bouchard et al. 2009). However, the choice of wavelength modulation source can significantly limit the amount and range of data which can be acquired with multispectral imaging. High imaging speeds are necessary for accurate measurement of sample physiology (spectral component images cannot be acquired far apart). The simultaneous imaging of absorption and fluorescence contrast enables more powerful experiments as multiple physiological systems can be measured simultaneously.

1.2.4 Modified Beer-Lambert Law

Parts of the discussion in this section are modified from the following references: (Kocsis et al. 2006, Hillman 2007).

Beer-Lambert Law for a homogenous slab

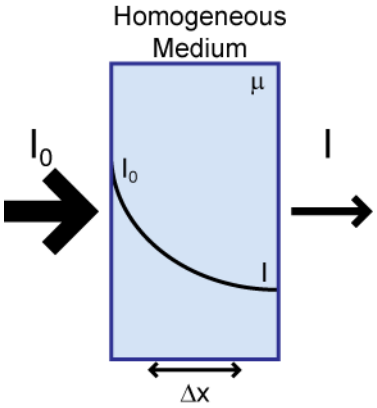

Figure 12: Beer-Lambert Law. Light traveling through a medium is attenuated by scattering and absorptive losses. The Beer-Lambert law describes the loss as a function of distance traveled through the medium and the physical properties of the medium.

Light traveling through a medium is attenuated by absorption and scattering losses (Figure 12). For light with intensity I_0 entering a medium, the differential loss of light at position x within the medium can be described as:

$$dI = -\mu I_0 dx \quad (13)$$

where I is the optical intensity at position x in the sample, μ is the attenuation coefficient which is a function of the medium, and x is the distance traveled into the medium. Equation (1) can be integrated to:

$$I(x) = I_0 e^{-\mu x} \quad (14)$$

This is the Beer-Lambert Law for a homogenous slab medium (Fuwa and Valle 1963). The transmission (T) of the medium is given by:

$$T = \frac{I}{I_0} = e^{-\mu x} \quad (15)$$

And the absorbance of the medium is given by:

$$A = -ln\left(\frac{I}{I_0}\right) = \mu x \quad (16)$$

Measurements of the absorbance and knowledge of the distance light has traveled into the medium can be used to calculate the medium's attenuation coefficient. For the homogenous slab geometry the attenuation coefficient can be described as the sum of the medium's absorption coefficient μ_a and the medium's scattering coefficient μ_s. If we assume no scattering losses in the medium, the attenuation coefficient is completely described by the absorption coefficient:

$$\mu = \mu_a = \varepsilon c$$

(17)

where ε is the extinction coefficient and is a wavelength dependent property of the medium which describes how the medium absorbs light at a given wavelength, and c is the concentration of the medium (for example see Figure 9 for hemoglobin absorption spectra). Extinction coefficient spectra are known *a priori* to wide-field multispectral imaging and can be obtained via measurements of pure samples of blood using the basic Beer-Lambert law and a spectrophotometer (Zijlstra et al. 1991). Therefore for a non-scattering medium:

$$A = -ln\left(\frac{I}{I_0}\right) = \varepsilon c x$$

(18)

the concentration of the medium can be directly calculated from measurements of the input and output optical power and medium thickness. In the case of a homogenous, non-scattering medium containing two absorbers, the absorbance becomes:

$$A = -ln\left(\frac{I}{I_0}\right) = (\mu_1^a + \mu_2^a)x$$

(19)

and:

$$A = -ln\left(\frac{I}{I_0}\right) = (\varepsilon_1 c_1 + \varepsilon_2 c_2)x$$

(20)

Given that the illumination intensity and extinction coefficients are wavelength dependent we can write Equation (21) as:

$$A(\lambda) = -ln\left(\frac{I(\lambda)}{I_0(\lambda)}\right) = (\varepsilon_1(\lambda)c_1 + \varepsilon_2(\lambda)c_2)x$$

(21)

where we assume the distance traveled in the medium is the same for all wavelengths. In the presence of scattering this assumption would not hold. To calculate the concentrations of each of the absorbers a minimum of two measurements of absorbance at two different wavelengths are required:

$$A(\lambda_1) = (\varepsilon_1(\lambda_1)c_1 + \varepsilon_2(\lambda_1)c_2)x$$
$$A(\lambda_2) = (\varepsilon_1(\lambda_2)c_1 + \varepsilon_2(\lambda_2)c_2)x$$

(22)

Systems of equations solution methods or matrix inversion techniques can then be used to calculate individual absorber concentrations. In the case of 2 absorbers and 2 measurement wavelengths the concentration of absorbers can be calculated from:

$$c_1 = \frac{A(\lambda_2)\varepsilon_2(\lambda_1) - A(\lambda_1)\varepsilon_2(\lambda_2)}{(\varepsilon_1(\lambda_1)\varepsilon_2(\lambda_2) - \varepsilon_1(\lambda_2)\varepsilon_2(\lambda_1))x}$$

$$c_2 = \frac{A(\lambda_2)\varepsilon_1(\lambda_1) - A(\lambda_1)\varepsilon_1(\lambda_2)}{(\varepsilon_1(\lambda_1)\varepsilon_2(\lambda_2) - \varepsilon_1(\lambda_2)\varepsilon_2(\lambda_1))x}$$

(23)

In the case of more measurement wavelengths than absorbers, least-squares fitting can be used to determine absorber concentration (Hillman 2007).

Spectral unmixing

Solving the systems of equations in Equation (**23**) to determine absorber concentrations is known as spectral unmixing (or linear unmixing) (Lansford et al. 2001, Bouchard et al. 2007, Hillman 2007). Spectral unmixing techniques have been applied within optical biomedical imaging to multispectral absorption measurements (Dunn et al. 2003, Bouchard et al. 2009, Chen et al. 2011, Kozberg et al. 2013), mixed fluorescence emission spectra (Lansford et al. 2001, Levenson and Mansfield 2006, Bouchard et al. 2007), mixed fluorescence excitation spectra (Radosevich et al. 2008, Grosberg et al. 2011), and time-dependent dynamic signals (Hillman and Moore 2007, Amoozegar et al. 2012). Spectral unmixing can be used to quantitatively visualize multiple spatially co-located biomarkers. Combined with high-speed imaging over time, spectral unmixing techniques can provide spatiotemporally resolved measurements of the changing concentrations of multiple co-located markers. This is an especially important capability for exposed cortex neuroimaging studies where the oxygenation state of the brain can be tracked through measurement of the changing concentrations of oxygenation and deoxygenated hemoglobin.

Modified Beer-Lambert Law for wide-field 2D Optical Intrinsic Signal Imaging

The Beer-Lambert Law provides a simple, yet powerful, method to determine material concentrations in the homogenous slab geometry. In the case of wide-field, 2D cortical neuroimaging the modified Beer-Lambert Law is used to account for the reflective imaging geometry (Figure 29). The modified Beer-Lambert law adjusts the distance variable in the original Beer-Lambert Law to account for wavelength dependent scattering and introduces a geometry dependent factor:

$$A = ln\frac{I_0}{I} = -\mu_a DPFx + G$$

(24)

where DPF is known as the differential pathlength factor and is the mean pathlength light traveled in the tissue and G is a geometry dependent factor. Both of these values are typically assumed to be constant. The DPF is a function of the material's wavelength dependent optical properties and is assumed not to change during a change in blood flow. DPF must be determined *a priori* to measurement and can be determined experimentally or theoretically (Kocsis et al. 2006, Hillman 2007). DPFx is therefore the true pathlength traveled by light. In this work we used DPF values estimated from Monte Carlo simulations of light propagation in brain tissue (Dunn et al. 2005). In the case of measuring hemodynamics in the cortex *in-vivo*, G is assumed not to be a function of absorption changes and accounts for loss of light due to scattering changes (Kocsis et al. 2006, Hillman 2007). In our neuroimaging studies we assume no scattering changes during the functional response. Substituting for μ_a for a single absorber we have:

$$A = ln\frac{I_0}{I} = -\varepsilon c DPFx + G$$

(25)

The absorber concentration can then be solved for directly with knowledge of DFP and G.

In wide-field 2D imaging applications it is difficult to measure I_0 accurately because it is typically spatially varying and G is difficult to quantify (Hillman 2007). Therefore time-dependent changes in absorber concentration are typically calculated from measurements of changing absorbance:

$$\Delta A = ln\frac{I(t)}{I(t_0)} = -\varepsilon \Delta c DPFx$$

(26)

The change in absorber concentration can then be calculated directly. In the case of N co-located absorbers, at least N measurements must be performed at different wavelengths to calculate changing absorber concentrations. For example, for two absorbers:

$$ln\frac{I_{\lambda_1}(t)}{I_{\lambda_1}(t_0)} = -(\varepsilon_1(\lambda_1)\Delta c_1 + \varepsilon_2(\lambda_1)\Delta c_2)DPFx_{\lambda_1}$$

$$ln\frac{I_{\lambda_2}(t)}{I_{\lambda_2}(t_0)} = -(\varepsilon_1(\lambda_2)\Delta c_1 + \varepsilon_2(\lambda_2)\Delta c_2)DPFx_{\lambda_2}$$

(27)

Spectral unmixing techniques can then be used to determine the changing absorber concentrations. The change in concentrations can be calculated from:

$$\Delta c_1 = \frac{\varepsilon_2(\lambda_1)\frac{DPFx_{\lambda_1}}{DPFx_{\lambda_2}} ln\frac{I_{\lambda_2}(t)}{I_{\lambda_2}(t_0)} - \varepsilon_2(\lambda_2) ln\frac{I_{\lambda_1}(t)}{I_{\lambda_1}(t_0)}}{\left(\varepsilon_1(\lambda_1)\varepsilon_2(\lambda_2) - \varepsilon_1(\lambda_2)\varepsilon_2(\lambda_1)\right)DPFx_{\lambda_1}}$$

$$\Delta c_2 = \frac{\varepsilon_1(\lambda_2)\frac{DPFx_{\lambda_2}}{DPFx_{\lambda_1}} ln\frac{I_{\lambda_1}(t)}{I_{\lambda_1}(t_0)} - \varepsilon_1(\lambda_1) ln\frac{I_{\lambda_2}(t)}{I_{\lambda_2}(t_0)}}{(\varepsilon_1(\lambda_2)\varepsilon_2(\lambda_1) + \varepsilon_1(\lambda_1)\varepsilon_2(\lambda_2))DPFx_{\lambda_2}}$$

(28)

Corrections for partial volume effects and cross talk between chromophores are included in modified versions of this law where the standard assumptions of the MBLL (absorption changes homogenously throughout the sampled volume and no cross talk in scattering changes between chromophores) are not held (Kocsis et al. 2006). In our neuroimaging studies we hold the standard assumptions due to the short path lengths of the wavelengths of light chosen and therefore the relatively small volumes probed by light in our reflective geometry.

1.2.5 Conventional OISI system designs

Wide-field 2D multispectral imaging systems must acquire sets of images at multiple wavelengths to create a single "multispectral image." As the number of absorbers increases, so too does the number of spectral component images which must be acquired. In the case of multispectral absorption imaging, at minimum N – 1 images must be acquired to decompose N absorbers (Lansford et al. 2001, Zimmermann et al. 2003). Conventional multispectral imaging systems modulate the wavelength of either the incident or the detected light (Figure 13). Most commonly, this is achieved using one of three distinct system designs: 1.) mechanical switching of excitation and/or emission filters, 2.) user of Bayer-mask simultaneous color camera imaging, and 3.) Multiview, spectrally resolved imaging systems.

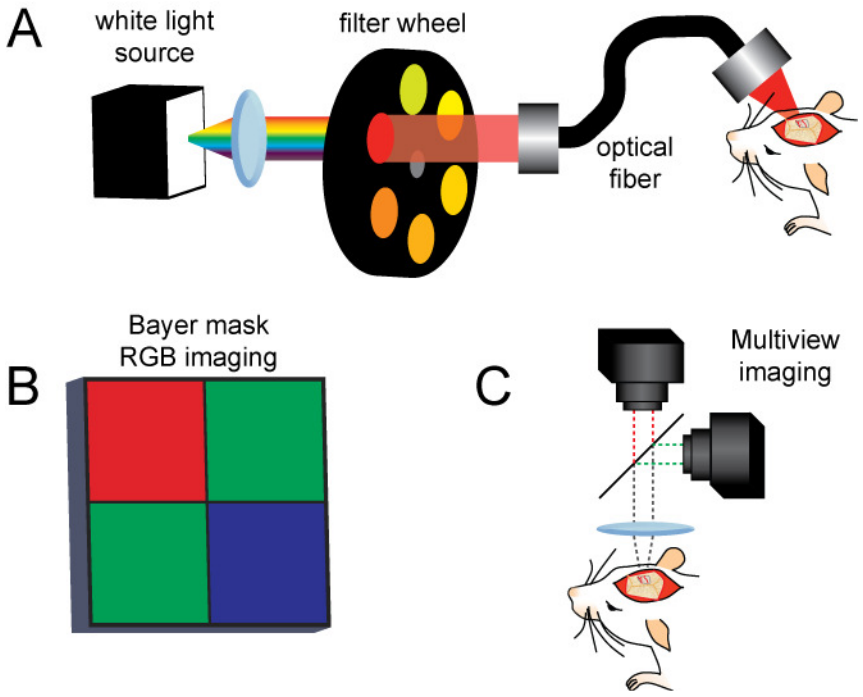

Figure 13: Conventional wide-field, multispectral imaging systems. A) Broadband white-light source and mechanical filter changer, B) Simultaneous multicolor imaging, and C) Simultaneous multiview imaging.

Design #1: Broadband white-light source and mechanical filter changer

The conventional approach to constructing multispectral imaging systems has been to modulate the wavelength of either incident or detected light. Most commonly, the incident light wavelength is modulated. A white light source, such as a halogen or mercury-xenon lamp, and band-pass filters to select appropriate wavelengths are typically used. Mechanical filter changers (most commonly filter wheels) provide switching of filters, with the filter changer generating a series of triggers for each filter change which instruct a camera when to acquire frames (Figure 13A). Filtered light is typically delivered to the sample via a flexible fiber-optic conduit for directed illumination. The main disadvantage of this system design is that cameras are not typically able to acquire at their maximum framerates when driven by an external trigger. Additionally, a filter wheel is generally limited to 6 positions, requiring purchase of a filter for each (even if fewer than 6 wavelengths are required). Unless duplicate filters are purchased, this limits the time in which one multispectral frame can be acquired to 1/6th of the triggered frame rate of the camera (e.g. 30 frames per second with 6 filters provides only 5 ‘ complete spectral frames’ per second (Devor et al. 2005, Dunn et al. 2005). Slow image acquisition speeds can affect the accuracy of spectral analysis since each spectral image is captured at a different time point. Further, even the highest performing white light sources do not have uniform spectral density, such that certain wavelengths may be less powerful than others. Galvanometer-based filter switching systems have recently become available (e.g. allowing 8 ‘spectral frames’ per second with 4 multiplexed wavelengths (Berwick et al. 2005)). While faster and more versatile than filter wheels, they are more costly and still limited by the total power and spectral range of the white light source. Tunable liquid crystal optical filters positioned in front of the camera on the detection side are typically lossy, slow, and not wholly effective in producing pure

wavelength passbands (Hahlweg and Rothe 2007). Detailed spectral analysis has been achieved by imaging a linear spectrometer onto the cortical surface, however alignment is challenging and the lack of a 2D image prevents detailed spectral analysis (Malonek and Grinvald 1996, Jones et al. 2001). Even if filter switching can be performed at higher speeds, it is generally impossible to synchronize mechanical filter changers with a free-running camera, and triggering a camera with signals from a filter changer results in much slower acquisition speeds. The mechanical complexity of filter changers also limits system portability and ease of integration of the system with other measurement techniques. These limitations have precluded the use of wide-field multispectral optical imaging techniques to image fast *in-vivo* processes.

Design #2: Simultaneous multicolor imaging

Simultaneous Bayer mask color imaging or a spectral image splitter with broadband white light illumination offers the advantage that complete multispectral images are acquired at the framerate of the camera (Figure 13B) (Prakash et al. 2007, Sakaguchi et al. 2007, Themelis et al. 2008) (Baik et al. 2013). However, typical color cameras offer only three, broad color channels optimized for reproducing vivid scenes and are not typically used for quantitative scientific applications. Color cameras commonly suffer from reduced signal-to-noise from optical filter losses, lower bit depth, reduced framerates, and reduced pixel sizes compared to monochrome cameras. Multispectral fluorescence imaging can be performed with proper selection of excitation wavelengths and bandpass filters (Muldoon et al. 2007). Imaging absorption and fluorescence contrasts on a single color camera can be difficult because reflected illumination powers are orders of magnitude larger than emission powers and will saturate the camera.

Custom Bayer masks with more than three color channels optimized for science applications are available from specialized equipment manufacturers but are inflexible for applications they are not designed for. Additionally, Bayer masks necessarily reduce the spatial resolution achievable because they typically require at minimum 4 pixels for each color pixel (one 'red', one 'blue', and two 'green' pixels for signal intensity balancing). Specialized Bayer masks with additional color channels only exacerbate the discussed challenges to using color cameras.

Design #3: Simultaneous multiview imaging

The third approach to multispectral imaging employs dichroic image splitters and multiple synchronized cameras (Figure 13C). For example, simultaneous imaging of speckle-flow- the measurement of the temporally changing speckle pattern created by illuminating the cortex with coherent light which can provide measurement of cerebral blood flow changes- and optical reflectance data has been demonstrated using two co-aligned cameras and a dichroic filter to spectrally discriminate light originating from a 785 nm laser diode (for speckle) and a filter-wheel with filters between 560 - 610 nm (for OISI) (Dunn et al. 2005, Devor et al. 2008, Shin et al. 2008). However it can be difficult to align and maintain precise pixel-to-pixel alignment between multiple cameras and system costs increase dramatically with increasing numbers of color channels.

Summary table of Conventional wide-field multispectral imaging systems

System Design	Temporally limited by	Spectrally limited by	Multiple sources of contrast?
Broadband white-light sources + mechanical filter changers	Mechanical filter wheel and camera synchronization	Number of slots on filter wheel (typ. 6)	Yes
Simultaneous Bayer mask imaging	Camera	Number of channels in Bayer Mask (typ. 3)	No
Multiview imaging	Camera(s)	Number of cameras used (expensive)	Yes

Table 1: Conventional wide-field multispectral imaging systems. Each imaging system is either temporally limited and/or spectrally limited. The number of spectra which can be acquired limits the number of absorbers which can be measured simultaneously. The ability to image multiple sources of contrast within the same experiment (i.e. absorbance and fluorescence) significantly improves the types and reach of wide-field multispectral imaging experiments.

1.3 Volumetric optical imaging

Wide-field 2D imaging techniques are not capable of imaging biological structures in 3-dimensions (3D) because they are not capable of confining optical signals to precise locations in 3D space (termed “optical sectioning”) (Figure 14A). Modern imaging techniques, such as laser scanning microscopy (Figure 14B), the more recent light sheet imaging techniques (Figure 14C), and Optical Projection Tomography (Figure 16) have been developed to overcome this limitation. Each of these 3D imaging techniques is capable of providing diffraction limited optical sectioning and imaging of samples in 3D through various imaging geometries and physical processes. However, each technique suffers from image acquisition rate limitations, the types of samples which can be imaged due to their commonly implemented imaging geometries, and the depth into samples at which they can resolve objects.

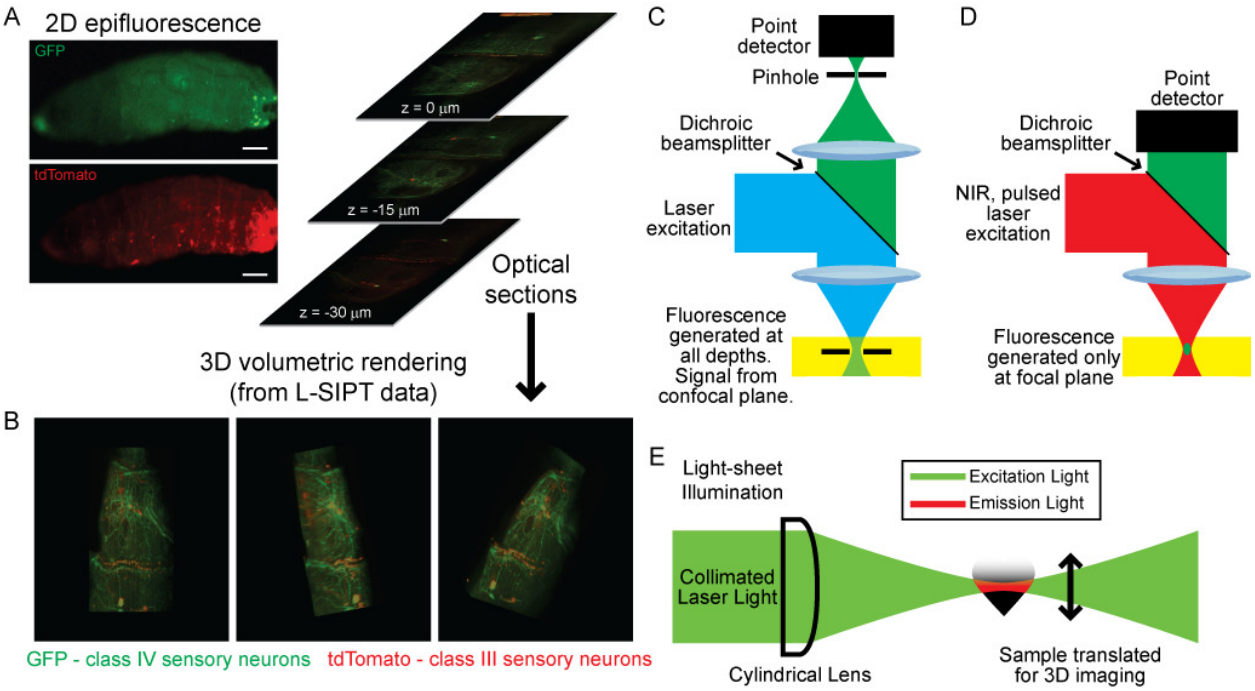

Figure 14: Volumetric Optical Imaging. A.) Images resolved in 3-dimensional space are said to be "optically sectioned." Optically sectioned images are similar to the types of images acquired from 2D images of single micron thick histological sections. However, optically sectioned images are acquired non-destructively and leave the sample intact for a full inspection. At left are epifluorescence images of a transgenic drosophila larva expressing GFP in class IV sensory neurons and tdTomato in class III sensory neurons (Grueber et al. 2002). At right are selected optical sections from a volumetric Laser-Scanning Intersecting Plane Tomography (L-SIPT) scan. B.) Stacks of optical sections can be rendered in 3D using computer visualization packages. Here we show three distinct views of the rendered optical sections from A.). C.) Optical sectioning can be achieved through a variety of imaging geometries. Confocal microscopy achieves optical sectioning by imaging a pinhole onto the focal plane of a focused laser beam. Signal originating from depths away from the focal plane is blocked by the pinhole. Optical scanners (not-shown) are used to steer the beam through the sample while mechanical translation stages are used to move the sample relative to the focal plane to construct 3D images pixel-by-pixel. D.) Two-photon fluorescence is a non-linear process whereby two photons are absorbed by the same molecule simultaneously to generate fluorescence at a shorter wavelength. Signal is only generated at the focused spot of the excitation laser, making signal collection easier than confocal microscopy. The same optical scanners and mechanical translation stages used by confocal microscopy are used to construct 3D images. E.) Light-sheet illumination microscopy creates single micron-thin sheets of light from laser light sources. These "light sheets" can be used to generate single micron-thin planes of fluorescence signal. 3D images are constructed by moving the sample step-wise through the sheet acquiring 2D optical sections at each step. Scale bars in A.) 200 μm.

Penetration of light in tissues

Light entering biological tissues can be scattered or absorbed (Section 1.1). The Beer-Lambert law provides a simplified model of light propagation through a media. The media's attenuation

coefficient describes the rate at which light energy is reduced by scattering and absorption events. The depth to which light can appreciably penetrate a medium is called the optical penetration depth and it is defined as the depth to which the incident light intensity is reduced to $^1/_e$ of its original value. In the case of the Beer-Lambert law this is equal to the inverse of the attenuation coefficient. This value is important to 3D optical imaging because it provides a measurement of how deep light can be expected to reach into a tissue regardless of the imaging geometry used. High scattering and absorption coefficients result in reduced depth penetration into tissues. Imaging places additional constraints on photon propagation into tissues, with different imaging geometries developed to overcome scattering and absorption losses in various tissue types and tissue sizes.

One strategy for increasing the penetration depth is to choose wavelengths of light which have low scattering and/or absorption coefficients for the medium under study. Biological tissues tend to have high scattering and absorption coefficients for UV into visible wavelengths of light and low coefficient values in the NIR. Lower scattering coefficients make imaging at depths easier as well. This is one reason imaging techniques such as two-photon fluorescence microscopy and second harmonic generation microscopy are so powerful: they are able to penetrate deeper into biological tissues while maintaining the ability to image at high resolution.

Another strategy for increasing the penetration depth involves modifying the optical properties of the medium itself. One of the major sources of light loss in biological tissues is scattering losses as light travels through cellular membranes. Cell membranes tend to have indexes of refraction close to 1.5 while the interior of cells have indexes closer to 1.33 (similar to glass and water, respectively). Optical clearing is a tissue fixation process which removes water from tissues and replaces it with a solution whose index of refraction is closer to that of the cell

membranes. This reduces tissue scattering to a minimum and allows light to propagate more directly through tissue unencumbered by scattering losses. Larger samples can then be imaged and signal can be resolved from deeper depths within samples. Computed tomography imaging techniques can be applied using visible light on large samples. However, optical clearing necessarily kills the sample and therefore can only be used in *ex vivo* studies. Additionally, it is a slow and complex procedure which can require tissue processing steps across multiple days to complete (Sharpe et al. 2002, Dodt et al. 2007).

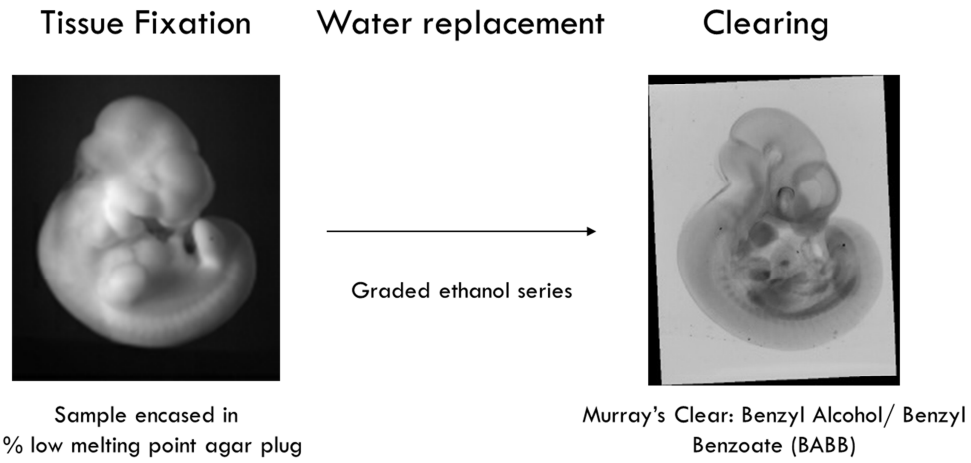

Figure 15: Optical Clearing Example. Optical clearing is a process which reduces the scattering properties of a sample, allowing light to travel deeper into biological tissues. Optical clearing replaces water with a chemical whose index of refraction more closely matches the index of refraction of cellular membranes to reduce the scattering coefficient. Previously opaque samples can be rendered nearly transparent using this process. Images from (Sharpe et al. 2002).

1.3.1 Existing approaches to volumetric optical imaging

Laser-scanning microscopies: Confocal and non-linear microscopies

Two of the most common 3D optical imaging techniques in use today are confocal microscopy and multiphoton microscopy (Denk et al. 1990, Helmchen and Denk 2005, Minsky 2011). Through their widespread commercial implementations, these microscopies have revolutionized

biomedical research *in-vivo*, *in-vitro*, and *in-situ*. Non-linear microscopy, specifically in the form of two-photon fluorescence microscopy, can provide diffraction limited 3D images of samples *in-vivo* at depths greater than 500 μm while reducing photobleaching and photodamage at planes away from the plane being imaged. Two-photon microscopy uses NIR wavelengths for fluorescence excitation. These wavelengths experience less scattering and absorption in tissue (including brain), allowing them to penetrate deeper into the brain to image at greater depths. Fluorescence excitation only occurs at the focal volume of the scanned laser beam which reduces photobleaching and photodamage at planes away from the imaged plane. This also allows for simpler, *en-face* illumination system designs (Radosevich et al. 2008, Grosberg et al. 2011).

Optical Projection Tomography: visible light computed tomography (CT)

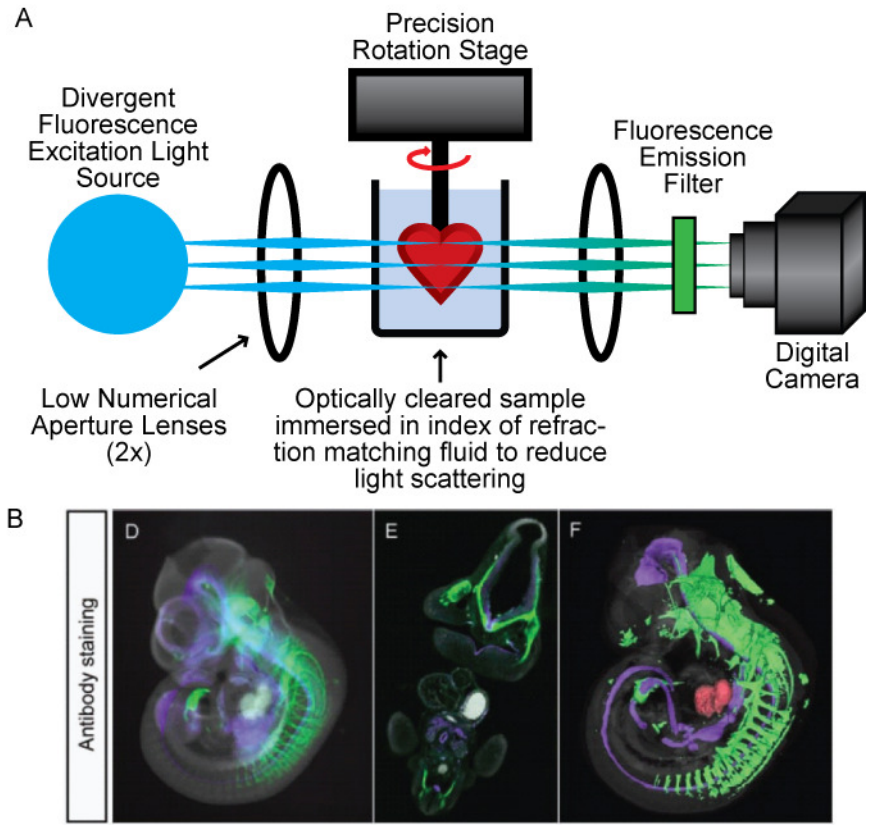

Figure 16: Optical Projection Tomography (OPT) system configured for fluorescence imaging. A.) OPT is an optical analog to x-ray Computed Tomography. A divergent fluorescence excitation light source is focused through the minimally to non-scattering sample using low numerical aperture optics. The sample is rigidly fixed to a precision rotation stage which rotates the sample in ~1° steps while projection images are acquired using a digital camera. Standard filtered-backprojection computed tomography reconstruction procedures can then be used, however improvements in image reconstruction quality can be obtained with optical models of computed tomography (Walls et al. 2007). B.) Example OPT reconstruction of a developing mouse embryo. Data acquired from a fixed optically cleared sample. Blue pixels label HNF3β gene, green pixels label neurofilament, and red blood autofluorescence. Image from (Sharpe et al. 2002).

Optical Projection Tomography (OPT) is an optical analogue to x-ray Computed Tomography (CT) which acquires projection images of transparent to minimally scattering samples and uses a modified back-projection algorithm to generate 3D images of absorbing and/or fluorescent contrast. The sample is rigidly mounted to and rotated with a precision rotation stage to acquire projection images (Sharpe et al. 2002, Sharpe 2003, Boot et al. 2008). OPT has been shown to have mesoscopic resolution (~10 μm^3 voxels) and the sample is preserved for subsequent

histology. However, to be effective OPT requires all but non-scattering samples to undergo optical clearing to reduce sample scattering to minimal levels so that light may travel straight paths through the sample. This is one of the assumptions underlying backprojection reconstruction algorithms. Optical clearing is a complex chemical procedure which removes water content from cells and replaces it with an index of refraction matching fluid whose index matches that of cellular membranes (~1.5) (Sharpe et al. 2002, Dodt et al. 2007). Historically optical clearing has involved a graded ethanol series to first dry the sample, potentially distorting the sample's morphology and potentially damaging exogenous contrast agents. New optical clearing procedures have been developed recently which offer improved clearing of larger samples while maintaining sample morphology and sources of contrast (Hama et al. 2011, Chung and Deisseroth 2013).

Light-sheet volumetric imaging

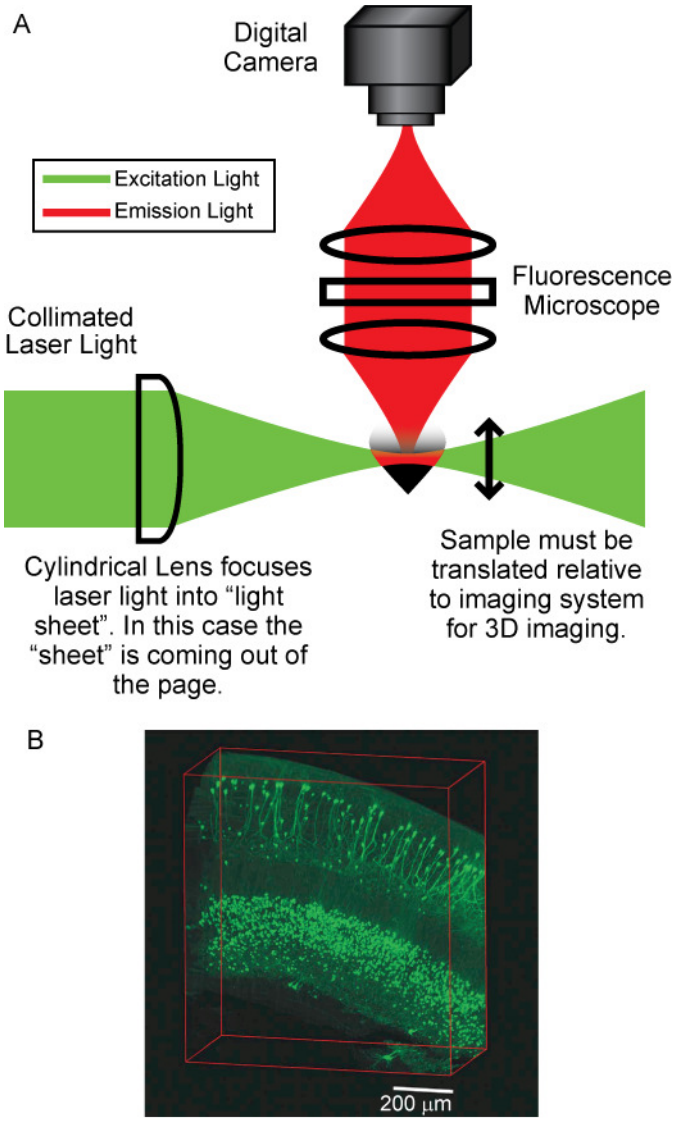

Figure 17: Basic Selective Plane Illumination Microscopy (SPIM) system. A.) In basic SPIM a 2D light sheet is created by focusing a collimated laser beam with a cylindrical lens. Light sheets with thicknesses ~1-10 mm thick can be created with off-the-shelf optics. The sample is placed within the sheet and a thin plane of fluorescence is generated. This optical section is then imaged with a rigidly mounted, orthogonally oriented fluorescence microscope. 3D volumes are imaged by translating the sample through the sheet in micron sized steps. B.) SPIM image of optically cleared, surgically resected transgenic mouse hippocampus. The imaged signal is mixed GFP and autofluorescence. The sample was optically cleared prior to imaging which necessarily killed the sample. Example image from (Dodt et al. 2007).

More recent approaches to volumetric imaging are encompassed by light-sheet imaging techniques such as selective plane illumination microscopy (SPIM), oblique plane microscopy

(OPM), objective coupled planar illumination microscopy (OCPI), and digital scanned laser light sheet microscopy (DSLM). These techniques achieve optical sectioning by illuminating the sample from the side using a thin 2D sheet of light and acquiring images using an orthogonal camera focused on the illuminated plane (Dodt et al. 2007, Verveer et al. 2007, Holekamp et al. 2008, Keller et al. 2010). The sample is then translated relative to the plane in micron sized steps to construct 3D image stacks. Sample rotation or multiview image acquisition can be incorporated into the volumetric image acquisition sequence to improve spatial resolution (Verveer et al. 2007, Krzic et al. 2012, Tomer et al. 2012). Light sheet illumination parallelizes volumetric image acquisition and constrains photobleaching and photodamage to the plane being imaged. Light-sheet techniques have been used to perform diffraction-limited 3D imaging of small or transparent samples, capturing processes such as cell division and migration during early embryogenesis (Dodt et al. 2007, Holekamp et al. 2008, Huisken and Stainier 2009, Keller et al. 2010). Optical clearing techniques can be applied to larger samples to aid in light penetration (Dodt et al. 2007, Hama et al. 2011, Chung and Deisseroth 2013).

Forming 2D light-sheets with a cylindrical lens

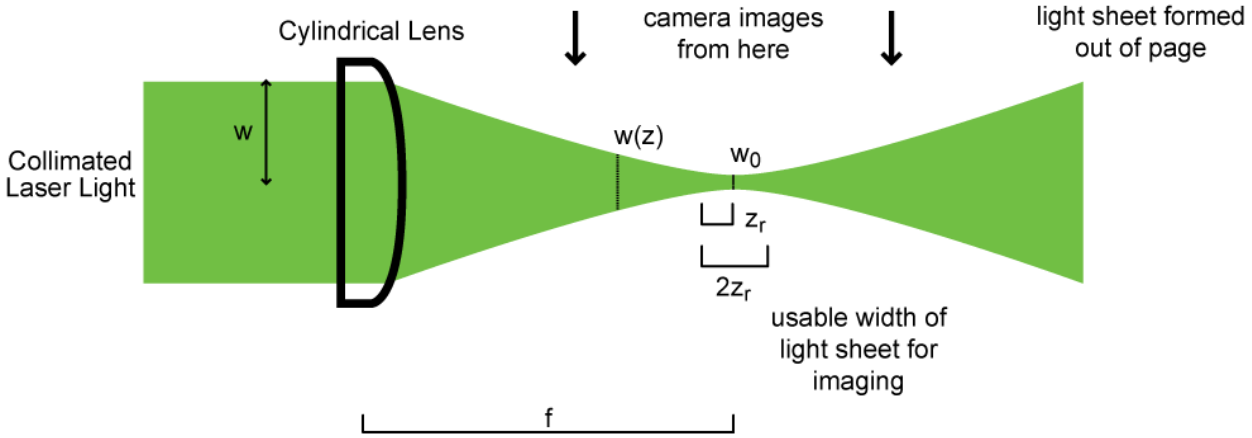

Figure 18: Light sheet formation using a cylindrical lens. Figure adapted from (Buytaert and Dirckx 2007).

The simplest method to form a light-sheet uses a cylindrical lens and a collimated input beam (Figure 18). A cylindrical lens is a lens which focuses light only along a single transverse axis, as opposed to standard spherical lenses which focus light along both transverse axes. The cylindrical lens will focus the collimated light to a linear image in the lens' focal plane. Light on either side of the focal plane creates a narrow "sheet" of high intensity light which can be used to excite fluorescence. The width of the sheet at its narrowest point, w_0, is given by:

$$w_0 = \frac{\lambda f}{\pi w} \tag{29}$$

where λ is the wavelength of light, f is the focal length of the cylindrical lens, and w is the radius of the collimated beam before focusing. The width of the sheet, w(z), at distance z from the focal plane is given by:

$$w(z) = w_0 \sqrt{1 + \left(\frac{\lambda z}{\pi w_0^2}\right)^2} \tag{30}$$

It is common to denote the usable width of the sheet as the width of the sheet where the thickness of the sheet has grown to $\sqrt{2}w_0$. This is defined as the Rayleigh range of the sheet, z_r. The confocal parameter is $2z_r$. The width of the light sheet sets the optical sectioning thickness for light sheet imaging and is therefore an important design parameter for any light-sheet imaging technique. From (30) we can see that with a tighter focused sheet at the center, the Rayleigh range of the sheet is reduced and vice-versa. Therefore, proper selection of sheet thickness and sheet width is a compromise which must be made on a sample by sample basis. For example, large samples may require a large sheet width and could tolerate a larger optical section thickness. This section drew from (Dodt et al. 2007) and (Buytaert and Dirckx 2007).

1.3.2 Volumetric optical imaging in neuroscience

Non-linear microscopy has revolutionized optical imaging in neuroscience through its ability to image a wide range of cell specific contrasts in the intact brain while inducing minimal amounts of photodamage to living tissues (Figure 19A). Simultaneous imaging of intrinsic sources of contrast (both fluorescent and other non-linear processes) and exogenous sources of contrast have enabled functional imaging studies probing the interactions between almost any combination of cellular and tissue level components of the brain (Radosevich et al. 2008, Grosberg et al. 2011, Grosberg et al. 2012). Volumetric optical imaging is largely applied to *in-vivo* rat and mouse neuroimaging. Studies probing the morphological interactions between blood vessels and nervous system cells can be performed (blood vessels labeled by red pixels, astrocytes by blue pixels in (Figure 19B-C)) (McCaslin et al. 2009). Blood flow velocity, blood vessel dilation dynamics, and RBC density changes in response to stimulus can be performed by imaging fluorescently labeled blood plasma (Figure 19D-I) (Hillman 2007). The same

intracellular calcium indicators used in 2D wide-field optical imaging can be used for 3D imaging (Figure 10). Exogenous calcium indicators such as Oregon Green and transgenic labels such as GCaMP provide spatiotemporally resolved 3D signals which directly correspond to neuronal activity (Bouchard et al. 2009, Akerboom et al. 2012).

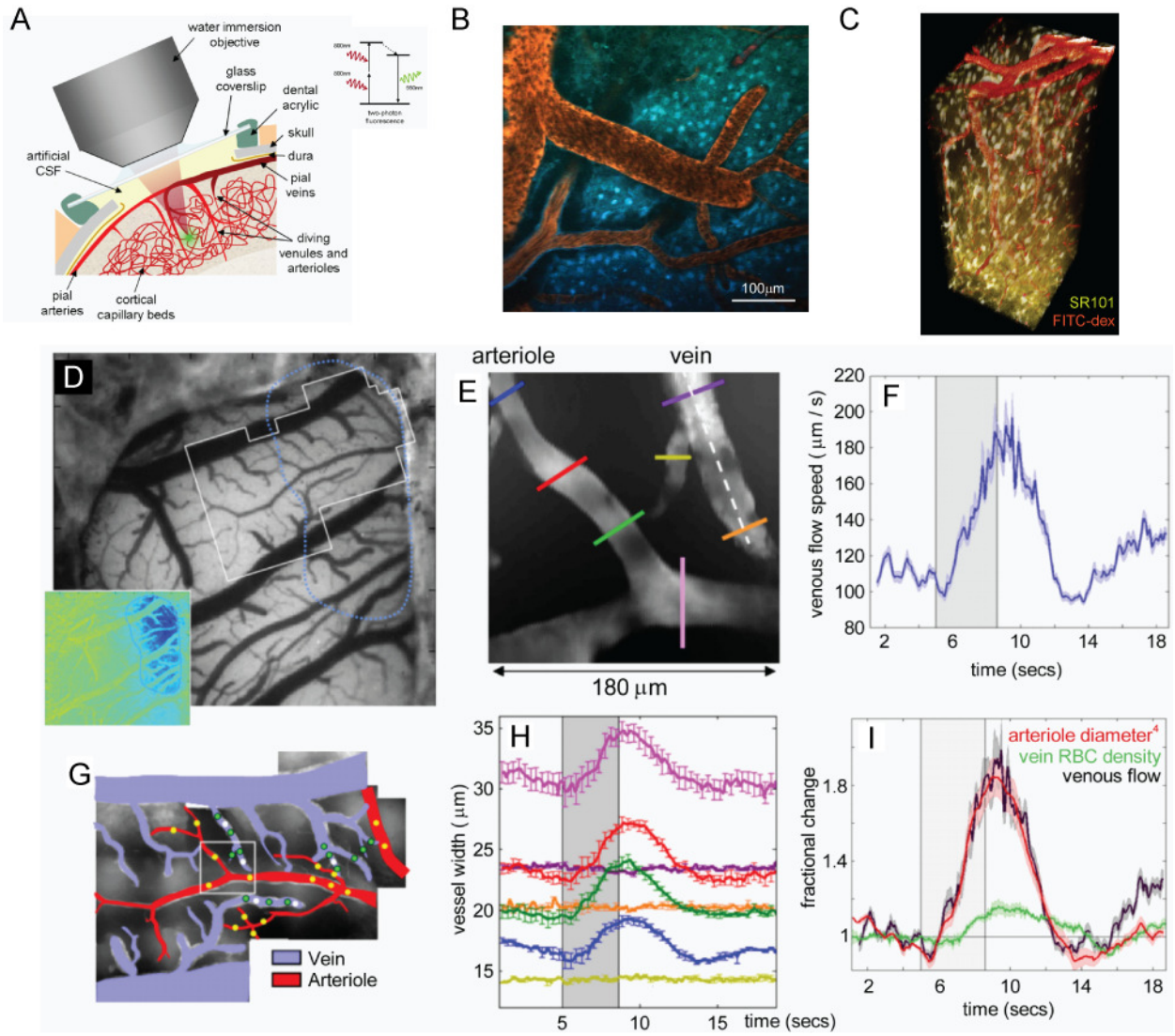

Figure 19: 3D Optical imaging in neuroscience: functional brain imaging. A.) Two-photon fluorescence microscopy has revolutionized neuroscience research. It provides the ability to image objects ~1 μm in size at depths >500 μm into the cortex at video framerates *in-vivo* while inducing low rates of photobleaching and photodamage. We acquired wide-field, two-photon images at 22 fps. B.) RGB color image of a maximum intensity projection image from a two-photon z-stack. Red indicates FITC-conjugated dextran (FITC-dex) which labels blood plasma. Blue indicates sulforhodamine 101 (SR101) which labels astrocytes. C.) 3D volume rendering of a column of rat cortex co-labeled with SR101 (yellow) and FITC-dex (red). Volume 250 x 250 x 540 μm^3 in size. D.) Wide-field, 2D camera image of exposed rat cortex. Two-photon fluorescence image shown in panel G.) outlined by white box. (inset) hemodynamic responding region to somatosensory stimulation. E.) Mean image from two-photon time-series. Vessel dilation dynamics can be studied by extracting lines of pixels and plotting the signal as a function of time. Colored lines drawn on image correspond to vessel diameter timecourses shown in Panel H.). Blood flow velocities can be measured by tracking red blood cells (RBCs) as black objects on the bright fluorescent plasma background. G.) Mosaic maximum intensity projection image constructed from multiple depth stacks. Veins and arterioles can be identified by eye. H.) Blood vessel dilation dynamics in response to somatosensory stimulation, and I.) Comparison of the fractional change in response to somatosensory stimulation arteriole diameter, venous RBC density, and venous flow. Somatosensory stimulation parameters: 3 Hz stim delivered for 4 seconds, 0.3 ms width, 1.0 ± 0.1 mA amplitude. Stimulation period indicated by gray regions on timecourse plots in F, H, and I.). Figure adapted from the following: A.) (Hillman 2007). B, D – I.) (Hillman et al. 2007) C.) (McCaslin et al. 2009).

However, non-linear microscopy has been limited in the study of dynamic 3D systems, such as intercellular communication across entire neuronal networks, due to its slow scan speed across volumes large enough to capture these entire networks (Grosberg et al. 2012). Various methods have been proposed (for example: multi-spot scanning, use of spatial light modulators, or novel random access scan patterns) to increase the scan rates of two photon microscopy but these methods increase their sampling rates by necessarily reducing the size of the sampled volume. None of the proposed methods thus far have achieved the volumetric scan rates across sample volumes large enough to study full, intact networks in 3D (Grosberg et al. 2012). The new light-sheet volumetric microscopies offer improved volumetric acquisition rates through the 2D parallelization of data acquisition (Krzic et al. 2012, Tomer et al. 2012). However, their orthogonal imaging geometries and need to translate the same through the illumination light sheet have largely precluded their use for *in-vivo* cortical imaging, save for one system (Objective Coupled Planar Illumination microscopy) which physically translates the entire imaging system relative to the brain. However, this system has largely been used to acquire signals from 2D oblique slices in the brain at framerates up to 200 fps and not to acquire 3D data (Holekamp et al. 2008).

Chapter 2 High-speed, 2-dimensional multispectral imaging

Wide-field, 2-dimensional (2D) imaging is performed by illuminating tissue with light and capturing wide-field 2-dimensional (2D) images using a camera. Images acquired in this manner can provide detailed information about the structure and function of living tissues via contrast from endogenous and exogenous absorbers and fluorophores. High-speed imaging can capture dynamic events such as changes in blood flow or responses to stimulation. Multispectral imaging (also known as hyperspectral imaging when dense spectral data is acquired) is any imaging technique which captures spectrally encoded information from a sample. Spectral unmixing is a mathematical process used to analyze multispectral image data which yields two-dimensional maps of the relative concentrations of absorbers and/or fluorophores in an image. High-speed, multispectral imaging combined with spectral unmixing is especially powerful for biomedical imaging because it can reveal information about the structure and function of multiple, co-located tissue absorbers and/or fluorophores in parallel, non-invasively, and non-destructively with subcellular resolution. Studies of living tissues in which the spatiotemporal behavior of multiple tissue absorbers and/or fluorophores can be tracked in the same sample *in-vivo* over periods ranging in length from seconds to weeks are routinely performed (Levenson and Mansfield 2006, Bouchard et al. 2007, Radosevich et al. 2008, Grosberg et al. 2011). Within neuroscience wide-field 2D imaging has been used to study the oxygenation state of hemoglobin

in the exposed cortex (Tso et al. 1990, Owen et al. 1998, Blood et al. 2002, Fox et al. 2005, Bouchard et al. 2009). Combining multispectral absorption imaging with active fluorophores sensitive to intracellular calcium concentrations or membrane potentials can be used to provide measurements of functional interactions between the vascular system and nervous system cells, such as neurons and astrocytes, potentially leading to a deeper understanding of the physiological mechanisms underlying the hemodynamic response (Bouchard et al. 2009). Studies such as these have implications for the significant body of neuroscience research which relies upon functional Magnetic Resonance Imaging (fMRI) as well as on current and future neuro-pharmaceutical designs (Rayshubskiy et al. 2013).

A multispectral image can be constructed from a set of images acquired under different illumination and/or detection spectral conditions, or from a series of spectra acquired point-by-point as in a laser scanning microscope (Palero et al. 2007, Radosevich et al. 2008, Grosberg et al. 2011). In wide-field 2D imaging of exposed cortex a set of component images of the sample acquired under different illumination wavelengths typically constitutes a single multispectral image. Conventional imaging systems used in wide-field 2D exposed cortex imaging studies employ a variety of methods to acquire spectral datasets, including modulating illumination wavelengths (Bouchard et al. 2008, Bouchard et al. 2009, Bouchard et al. 2009), modulating detection wavelengths (Bouchard et al. 2007), and simultaneous multi-color detectors as in color cameras (Dunn et al. 2005, Muldoon et al. 2007, Themelis et al. 2008). Each of these system architectures impose limitations on the maximum spatial and temporal resolutions which can be acquired and the range of contrasts which can be used simultaneously, limiting the types of experiments which can be performed. In this Chapter we describe the implementation of a new ultra-fast, multispectral, 2D wide-field optical imaging system which is not limited to the same

spatiotemporal resolution limits or contrasts sources seen in existing systems. In Section 2.1 we detail the concept, design, and construction of our new ultra-fast, multispectral, wide-field imaging system. Two versions are described, one a bench top instrument and the other a modular, low-cost, laptop based version for which we have made both the design and source code open to the scientific community. In Section 2.2 we demonstrate initial applications of our new system to *in-vivo* and clinical exposed cortex imaging of hemodynamics in living rodent cortex and living human cortex, respectively. Lastly, we show how the system can be incorporated into epifluorescence microscopes and used to image calcium signaling dynamics in living cardiac stem cells.

2.1 High-speed, multispectral 2-dimensional imaging system

Conventional multispectral imaging systems modulate the wavelength of either the incident or detected light. Most commonly, this is achieved using filter-changers, filter wheels, or tunable filters, all of which offer slow transition times which greatly reduce image acquisition speed. Even if wavelength switching can be performed at higher speeds, it is generally impossible to synchronize mechanical filter changers with a free-running camera, and triggering a camera with signals from a filter changer results in much slower acquisition speeds. The mechanical complexity of filter changers also limits portability and ability to easily integrate with other measurement systems. These limitations have precluded the use of multispectral optical imaging techniques to image dynamic *in-vivo* processes. In this Section we detail the design (Section 2.1.1), construction (Section 2.1.2), and application of our novel high-speed, multispectral wide-field imaging system whose camera-first design overcomes the spatiotemporal resolution limitations of previous multispectral imaging systems.

2.1.1 System concept

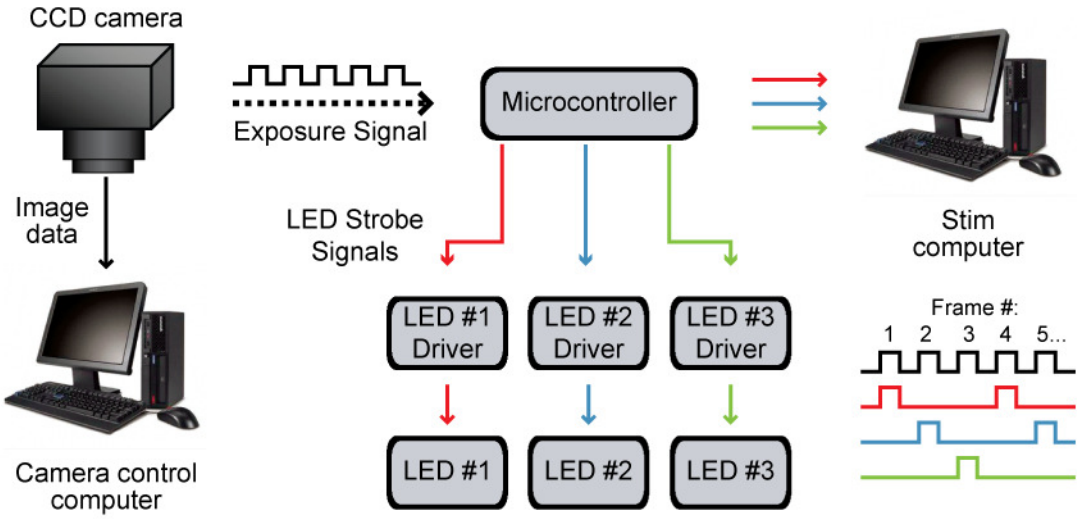

Figure 20: High-speed, multispectral imaging system concept. In our novel multispectral imaging system design image acquisition is completely digitalized. A high-speed camera is allowed to free-run at up to its maximum framerate. A TTL exposure signal indicating when the camera is exposing each frame is read by a low-cost microcontroller. Following a pre-programmed strobe sequence, the microcontroller outputs strobe signals to individual LED light sources. Image data is recorded by a camera control computer while a stim computer records the strobe signals for off-line data analysis. An example serial strobe sequence for 3 LEDs is shown at bottom right.

Our novel multispectral imaging system design overcomes the limitations of conventional wide-field multispectral systems at a reduced cost through the use of multiple co-aligned, high power, rapidly modulated light emitting diodes (LEDs), and a high-speed, low-cost, microcontroller-based synchronization circuit which synchronizes wavelength modulation to camera image acquisition. The exposure signal from the camera, which indicates real time frame-grabs (TTL), is used to synchronize sequential strobing of the LEDs via the microcontroller (Figure 20). This system design allows any camera to free-run at up to its maximum frame rate unencumbered by external synchronization issues. Not only does this design allow for increased frame rates over filter wheel systems, it also allows novel programmable strobe sequences and can utilize the broad range of strobable LED, laser diode,

and laser light sources available today making high illumination power available at almost any wavelength. Also, the power of each source can be tuned individually to provide optimal signal-to-noise and dynamic range, and each source can be individually filtered to block any wavelengths that are not required. Since each light source is illuminated sequentially, appropriate emission filters in front of the system's camera can allow acquisition of rapidly multiplexed fluorescence and absorption data within a single run. Laser diode and laser light sources can be easily integrated into the system and can used to perform speckle flow imaging in conjunction with absorption and fluorescence multiplex imaging (Dunn et al. 2005).

Using a programmable microcontroller allows the system's light sources to be modulated in synchrony with each image frame, which provides a range of benefits. First, at high frame rates inexpensive cameras without a high-speed shutter can suffer from a streaking artifact due to exposure of the imaging chip during data read-out. Using the camera exposure's signal, the microcontroller can precisely strobe the light source such that it only illuminates the sample during image acquisition and not during read-out. This in turn also reduces photobleaching and photodamage of the sample. Further, the microcontroller allows multiple different light sources to be strobed in any arbitrary sequence, allowing acquisition of high-speed multispectral or interlaced reflectance and fluorescence images. Since the microcontroller derives these illumination drive signals from the camera in real-time, image acquisition can proceed at up to the maximum frame rate of the free-running camera, rather than requiring the camera to be triggered from a signal derived from either the computer or a wavelength-switching element such as a filter wheel. By outsourcing the light source switching duty to the programmable microcontroller, the camera control computer can focus on grabbing and writing image data to disk at its maximum rate. The system can acquire image data at this rate until the computer's

hard drive is full. Programming of the microcontroller is integrated into the system control software such that it sets up the microcontroller to generate a defined strobe order at the start of every new image acquisition sequence. This means that strobe sequences can be readily altered as needed within an experiment. The microcontroller used in our system (Arduino Diecimila and Uno have been used) is widely available and costs less than $30 (Foundation 2013).

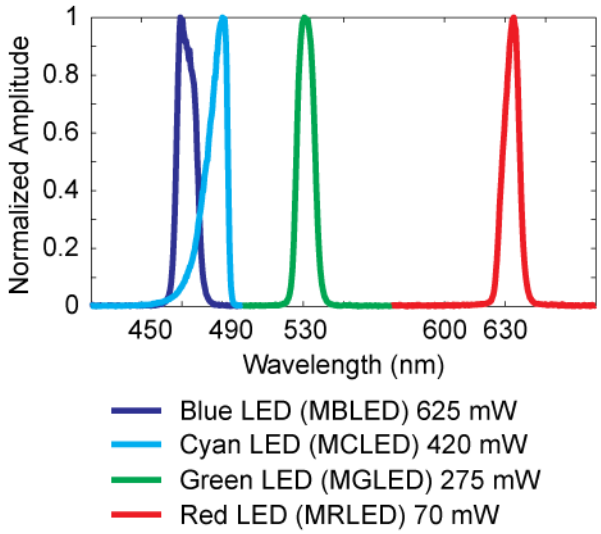

Figure 21: Spectra of commercially available high intensity, rapidly strobed LED light sources. Bandpass filters were used to narrow the illumination bands. Spectra measured with USB-2000 fiber spectrometer (Ocean Optics). LEDs from Thorlabs, part numbers listed for each LED used in original system design.

Our multispectral imaging system relies on the use of strobed light emitting diodes (LEDs) for illumination (example spectra through bandpass filters shown in Figure 21). The benefits of this approach are threefold: 1) LEDs are now available over a wide range of wavelengths, providing substantially more power at required wavelengths than is often obtainable from a filtered white light source, 2) LEDs are inherently portable, robust and low cost, 3) The response times of modulated LEDs allow strobing to be driven by pulse sequences derived from the real-time 'frame grab' output from a free-running camera. This design, therefore, completely digitizes the acquisition process and removes many of the existing framerate-limiting factors associated with filter-wheels and/or mechanical filter changers. As a

result, our system can strobe any combination of LEDs in any sequence at up to the highest acquisition speed of any camera. Low-cost, high power LEDs have recently become commercially available which offer spectral bandwidths of approximately 25 - 75 nm and optical powers approaching 1 W. As Figure 25 illustrates, two LEDs and a combining dichroic beamsplitter can be used to create a multiwavelength illuminator that does not require physical movement to change the illumination wavelength. The LEDs reach their full illumination intensity in < 25 μs, and can be modulated at rates up to 5 kHz with commercially available drivers (LEDD1B, Thorlabs).

2.1.2 System Realization

Commonly available commercial camera software packages are restricted in their utility beyond their designed for application or are optimized for *in-vitro* microscopy applications (e.g. point-and-click single frame acquisition, or slow time-lapse image acquisition routines for microscopy) (Sun et al. 2010). To best perform functional imaging experiments, our imaging systems must be able to:

1. Acquire ‘runs’, or ‘sets’, of data at high frame rates for periods of between 10 and 60 seconds. The start of each run must usually be triggered either internally by the camera or externally via an outside trigger timed precisely to stimulus or other experimental events.

2. Acquire multiple ‘runs’ of data in sequence without additional user input.

3. Provide the option to save acquired images in a standard image format, suitable for analysis by custom or commercial software analysis packages.

4. Be controlled by a simple graphical user interface (GUI) capable of providing intuitive and rapid control over major camera parameters (e.g. ability to set spatial binning, frame rates, regions of interest, etc.) and image acquisition routines.

5. Provide the flexibility to image fluorescence and absorption contrast, as well as the capability to switch quickly between the two during an experiment.

6. Provide the capacity to operate with multiple light sources for multispectral and/or fluorescence image acquisition.

7. Be compatible with physically adaptable hardware which can be arbitrarily positioned around living tissues/animals during imaging.

8. Be compatible with a wide range of imaging optics from wide-field lenses to high optical power microscope objectives.

9. Require relatively low monetary investment and be simple to implement.

To meet these design requirements we developed Graphical User Interfaces for both generations of our novel multispectral imaging system (Figure 22). Behind each button in our GUIs control routines for each aspect of the multispectral imaging systems are hidden. We developed functions to control the camera, communicate with the microcontroller, and synchronize image acquisition with the stimulus control computer using Software Development Kits (SDKs) available from our camera manufacturers (Figure 20).

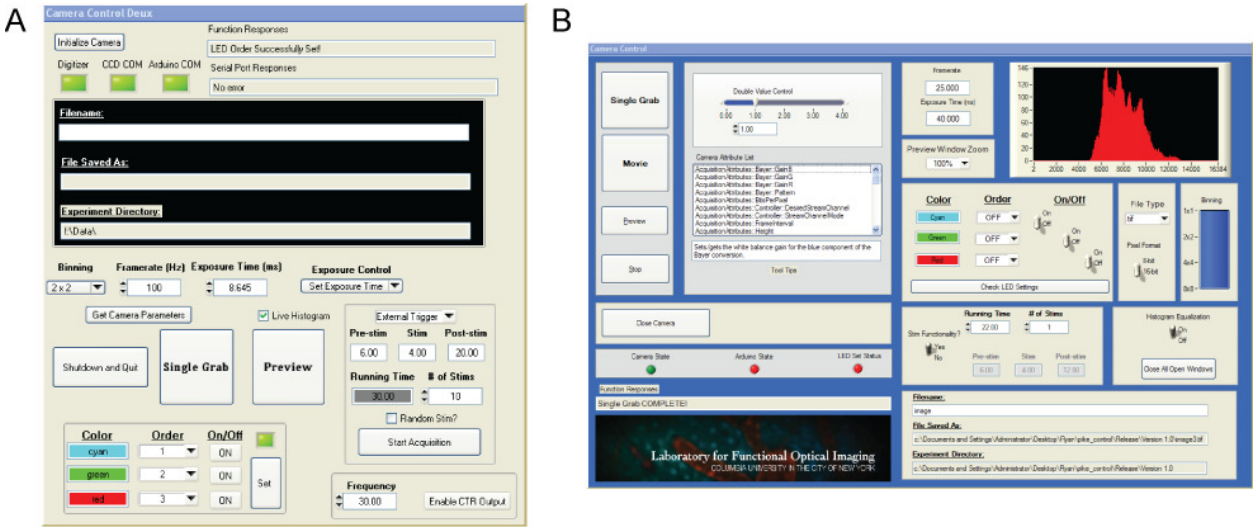

Figure 22: High-speed, multispectral imaging systems' camera control Graphical User Interfaces (GUIs). A.) First generation, benchtop system. B.) Second generation, open-source, modular system. This GUI can employ a wide range of 1394 Firewire standard cameras with minimal modifications to the GUI source code.

The most important task of the systems is to acquire “runs” of data. When a “run” is acquired a series of images are rapidly acquired and immediately saved to the computer’s hard drive for long term storage and offline analysis. This procedure is typically referred to as “streaming images to disk.” We designed an efficient streaming to disk routine to maximize the amount of data which can be acquired and saved to disk (Figure 23). This is important to maximize the spatiotemporal resolution of the acquired images and to fully utilize a computer’s resources. The common streaming to disk routine is to save all acquired images to the computer’s RAM during acquisition before writing the images to the hard drive after image acquisition is complete. This implementation is not optimal for functional imaging experiments because it limits the length of each “run” to the amount of RAM available divided by the size of the image and the image acquisition rate. Additionally, writing large amounts of data to disk requires a relatively large amount of time, increasing the amount of time between “runs” which reduces the efficacy of a functional imaging experiment.

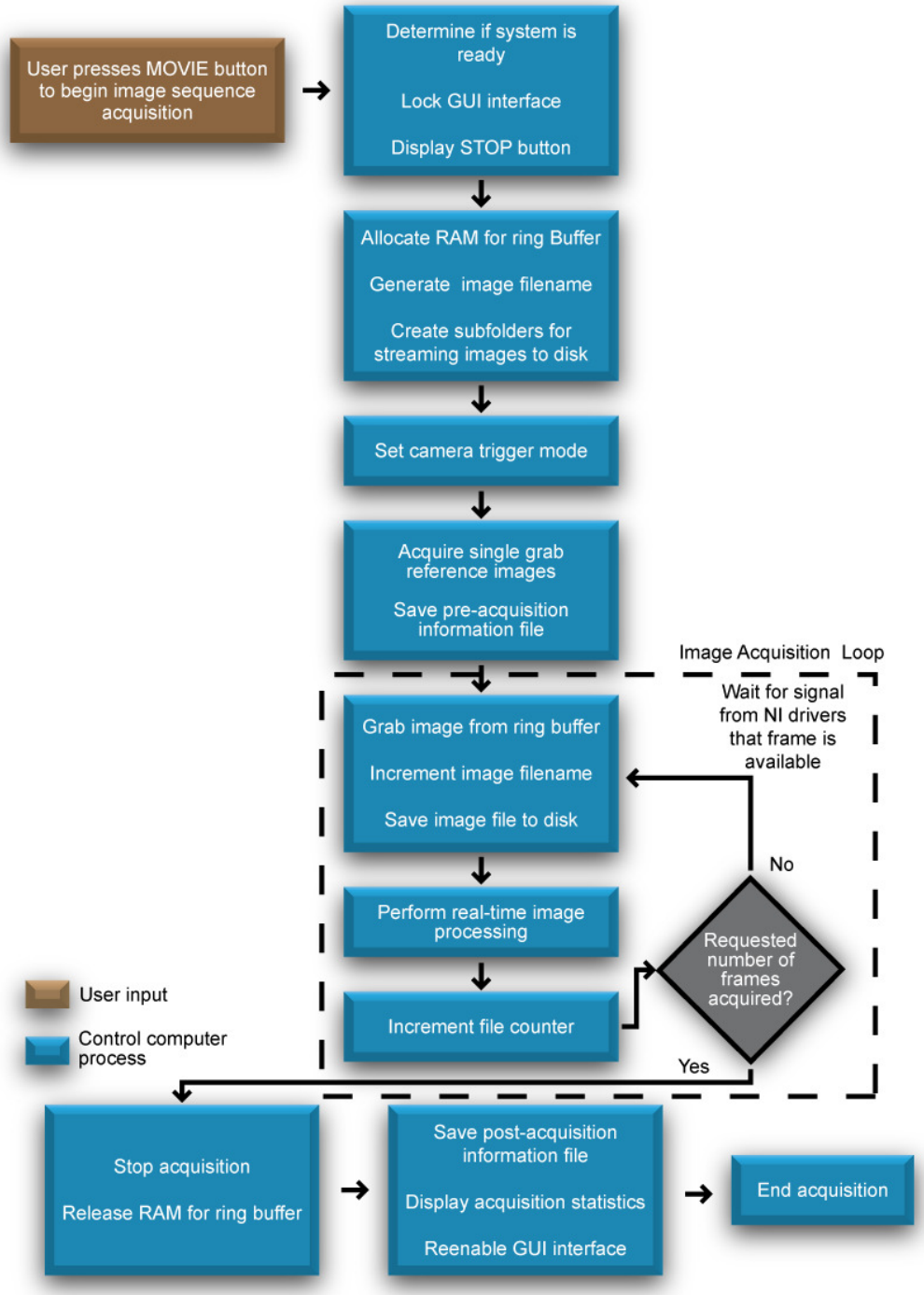

Figure 23: 'Movie' Image Acquisition Routine Flowchart. This flowchart details the major subroutines called when acquiring "runs" of data. Before a "run" can be acquired, the camera control program executes a series of preparatory subroutines. After the camera begins image acquisition, the control program enters the image acquisition loop in which frames are grabbed from the ring buffer, the image filename is incremented to reflect the number of the image acquired in the sequence, and the image is saved to the camera control computer's hard disk. Once the number of requested frames is acquired (determined by the frame rate multiplied by the length of the "run") the image acquisition loop ends. To end the acquisition of the "run", the control program executes a series of closing subroutines that prepare the system for the next acquisition.

The second control function unique to our multispectral imaging system was communication between the camera and the microcontroller to set illumination strobe sequences. Sequential strobe sequences for any order of up to 3 LEDs were preprogrammed and loaded into the microcontroller. Our imaging system control GUIs allow the user to select the desired sequence directly on the GUI (Figure 22). The camera control computer then sends a coded message to the microcontroller to select the desired strobe sequence. During image acquisition, the microcontroller senses the rising and falling edges of each frame acquisition and toggles the appropriate LED to turn on/turn off in sequence. This sequence of events is shown in Figure **24**.

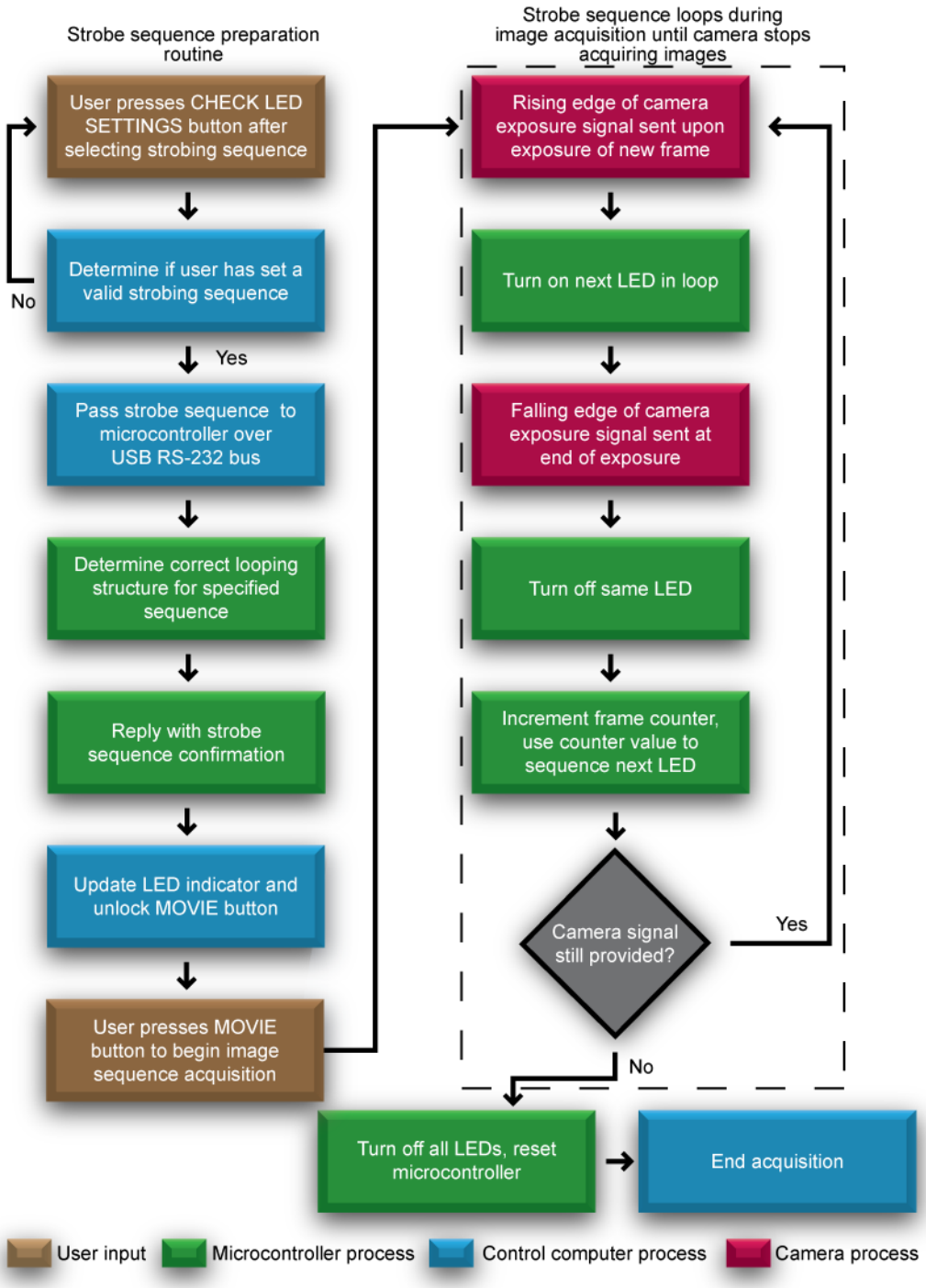

Figure 24: Multispectral illumination with a microcontroller flowchart. Multispectral illumination is provided through the interface of a microcontroller, control computer, and camera. Once the user inputs a desired strobing sequence from the GUI, the control computer checks the validity of the pattern and instructs the microcontroller to use a preprogrammed strobe sequence. If the process is successful, the user is allowed to begin image acquisition. During acquisition the microcontroller is driven by the camera to turn the LEDs on/off. A frame counter provides the next LED in the sequence. When acquisition ends, the microcontroller is reset.

Next we discuss the specific hardware implementations of the two developed systems. We developed two generations of the system: 1.) a prototype system which grew into a bench top, workhorse instrument and 2.) a portable, laptop based version whose control software was made generic to a large family of commercially available scientific cameras and open-source. This software package was released to the scientific community to broaden its use outside our laboratory and spur on its continued development.

1st generation high-speed, multispectral optical imaging system

Our 1st generation, workhorse system was constructed from a Pantera 1M60 12-bit CCD camera (Dalsa) and a Solios XCL/eCL framegrabber in the single-Medium CameraLink configuration (Matrox). A CameraLink breakout box (CLB-501, Vivid Engineering) was used to access all CameraLink signals, specifically the TTL EXSYNC exposure signal. Camera acquisition parameters, LED strobe synchronization, and image acquisition are controlled through a custom C image acquisition GUI which includes generic, off-the shelf functions from the Matrox Imaging Library Lite 8.0 software library (Matrox). A range of C-mount camera lenses can be attached to the camera depending on the required field of view and magnification required by a given experiment.

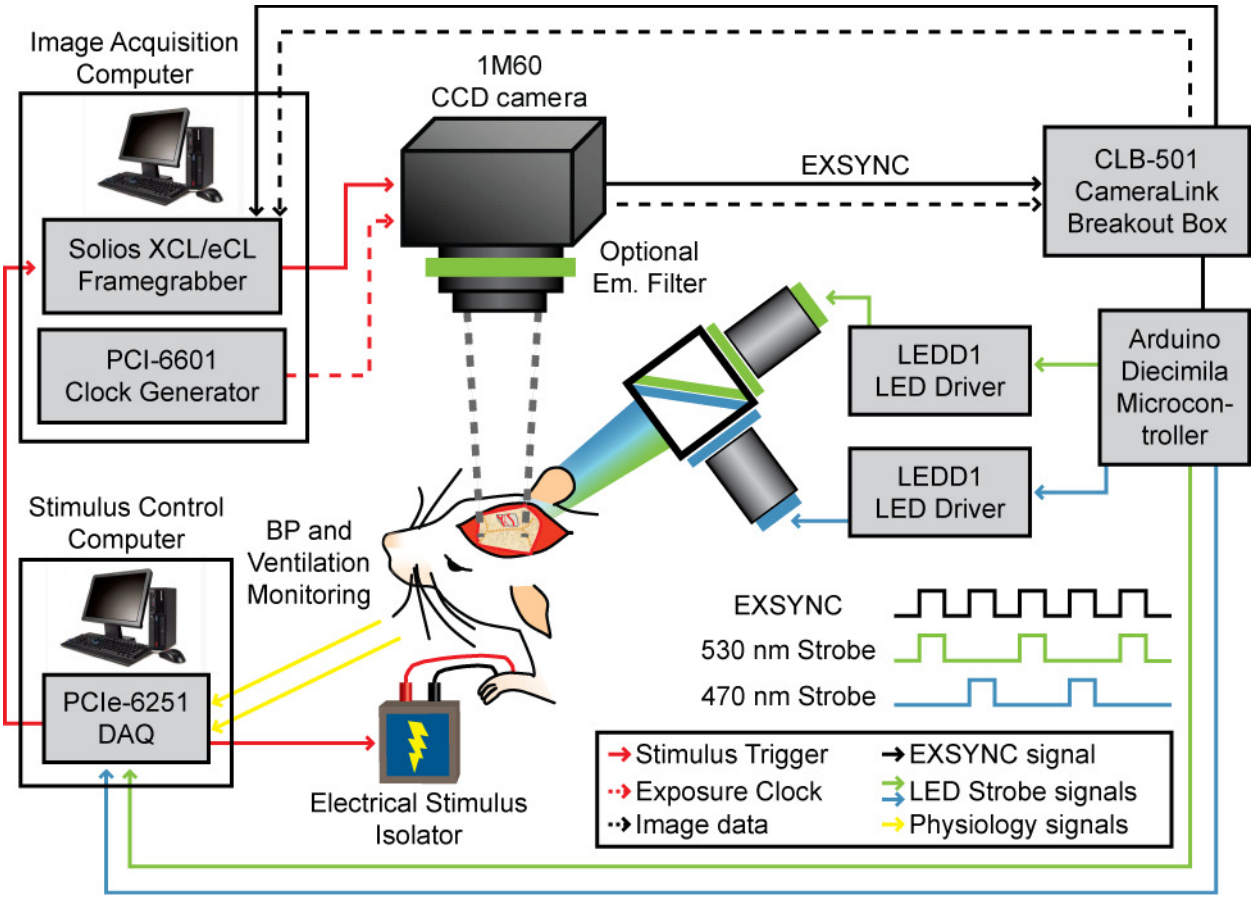

Figure 25: 1st generation high-speed, multispectral imaging system design. Multispectral image acquisition begins with a TTL Stimulus Trigger signal sent from the stimulus control computer to the trigger port of the clock generator (red arrow). The 1M60 CCD camera then begins acquiring frames according to the clock signal (dashed red arrow) generated by the clock generator. When the 1M60 acquires frames, it outputs the EXSYNC signal in real-time (black arrow), which is sent to the interrupt ports of the Arduino Diecimila microcontroller. Using a custom strobe function, downsampled strobe signals are generated by the Arduino and sent to the LED drivers which strobe the LEDs (green and blue arrows, example timing diagram shown bottom right). The strobe signals are recorded by the stimulus control computer, along with physiological signals such as blood pressure and ventilation signals from the animal in a neuroscience application (yellow arrows). System in figure is configured to quantify the concentrations of oxygenated hemoglobin (HbO_2), de-oxygenated hemoglobin (HbR), and total hemoglobin (HbT) while maintaining sensitivity to superficial vessels.

We utilized the TTL exposure integration signal (EXSYNC) generated by the camera as the master clock for image acquisition to synchronize LED modulation (black arrows, Figure 25). In Exposure Mode 4, the Pantera 1M60's exposure time is driven by a TTL pulse train generated by a PCI clock card (PCI-6601, National Instruments) internal to the image acquisition computer (red dashed arrows, Figure 25). This TTL pulse train instructs the camera when to

integrate signal on its sensor. The EXSYNC signal, generated internally by the camera to indicate when it is actively integrating signal, is routed to the interrupt input ports on the microcontroller (Arduino Diecimila, Sparkfun Electronics). A custom loop function written (Figure 24) to the microcontroller reads this TTL signal and serially strobes multiple LEDs locked to the edges of the EXSYNC signal (blue and green arrows, Figure 25). The EXSYNC signal is accessed via the CameraLink breakout box. Our Arduino control code can currently strobe up to three different LED in pre-programmed, arbitrary strobe sequences. With minor software and hardware modifications the system could strobe up to 54 light sources. Through utilization of the camera-generated EXSYNC signal, the camera is allowed to free-run at the user-defined framerate during image acquisition, unhindered by any external synchronization issues. In addition, because illumination is locked precisely to each frame acquisition, our system does not require any form of shuttering of the CCD sensor to avoid blooming artifacts. This reduces the cost and complexity of the required CCD camera, and reduces photobleaching and photodamage of the cortex by illuminating the sample for the minimum amount of time necessary. This system can acquire images at up to 220 fps (the camera's maximum frame rate), with 128 x 128 pixels (8 x 8 binning), or 160 fps with 256 x 256 pixels (4 x 4 binning). These image acquisition speeds allow complete dual-spectral image sets (a set of separate 470 and 530 nm illumination images, for example see Figure 25) to be acquired at 110 and 80 fps, respectively. This increased speed means that spectral analysis more accurately reflects the instantaneous state of the tissue. In addition, the speed and spatial resolution of our system also allows the motion of red blood cells to be discerned throughout the cortical vessels, thereby allowing the velocity of blood flow to be measured and mapped across the field of view using the same data (Bouchard et al. 2009, Chen et al. 2011, Kozberg et al. 2013).

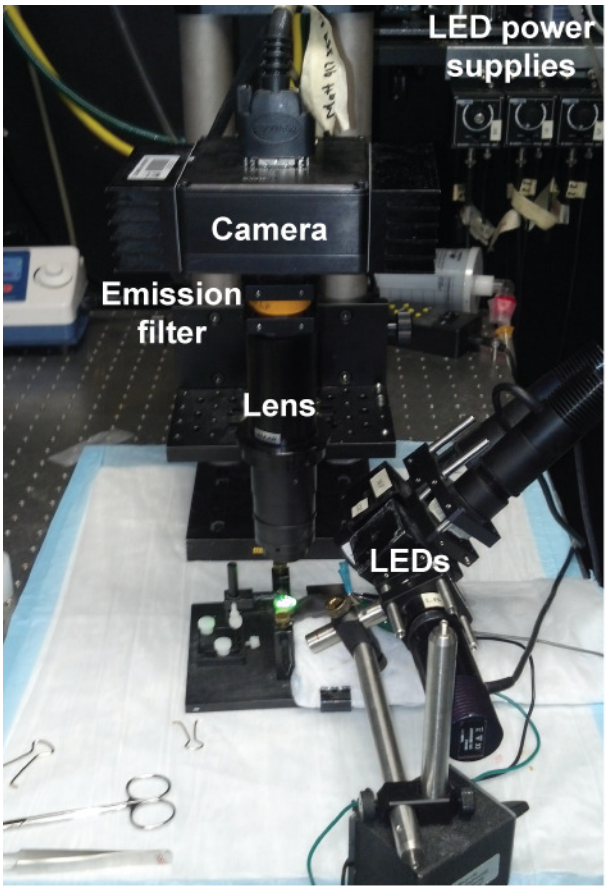

Figure 26: Photograph of 1st generation high-speed, multispectral optical imaging system.

2nd generation high-speed, multispectral optical imaging system: made portable and open source

Our 1st generation system was built from high-performance camera imaging hardware which required a relatively large equipment footprint in the laboratory. A high-speed CCD camera was connected to a high-data rate PCI-interface frame grabber in a desktop computer through a specialty CameraLink breakout box. Custom, non-portable GUI-based control code optimized for functional optical imaging experiments was developed for the specific hardware used. While this system architecture has proven successful as a workhorse instrument in our Laboratory, it also resulted in an inflexible, highly customized, expensive non-portable system.

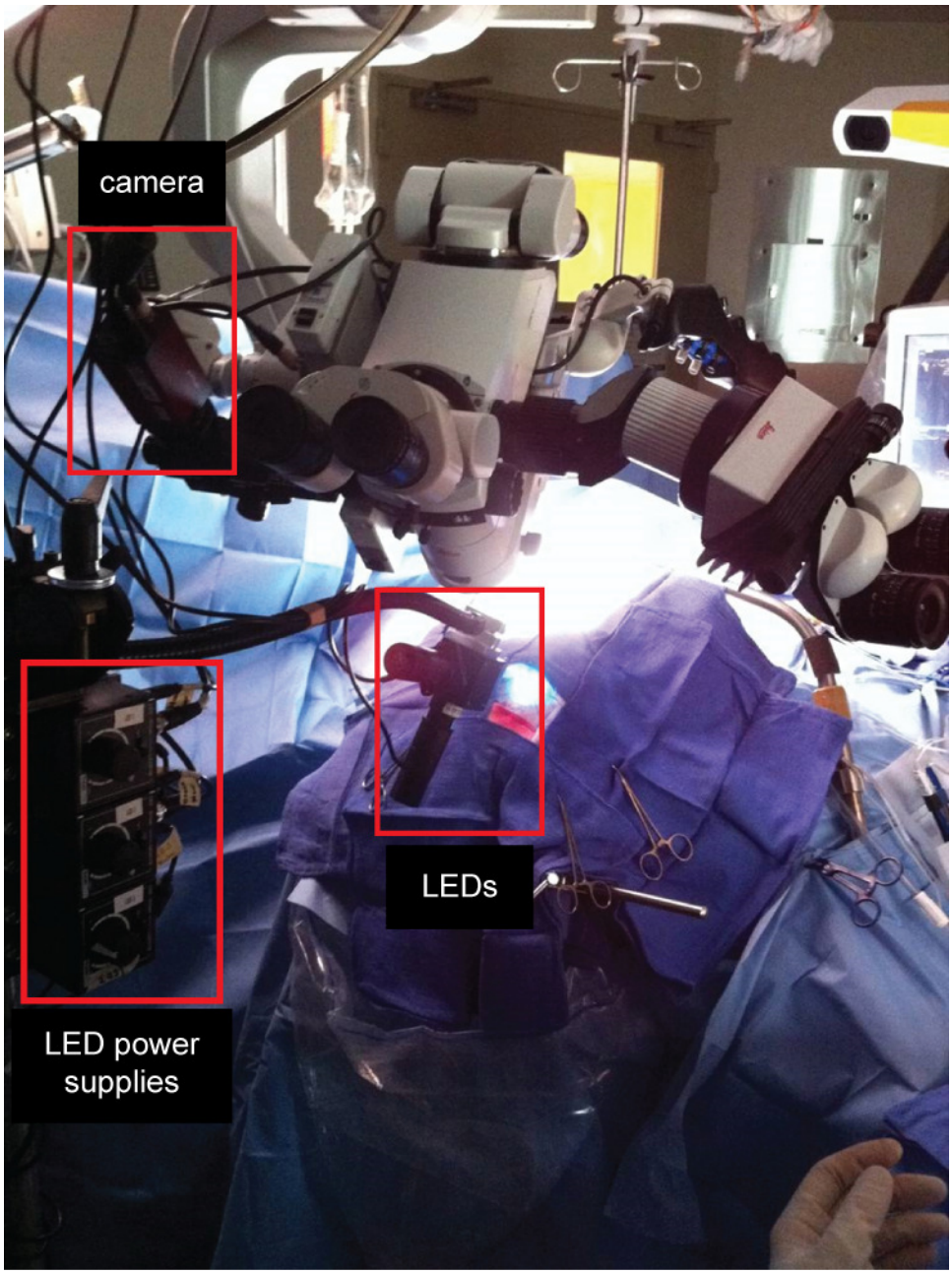

Figure 27: 2nd generation high-speed, portable multispectral optical imaging system. The system relies on three controlling elements: a monochrome, Firewire CCD camera, a microcontroller, and a laptop computer. Illumination is provided by strobed, high-power LEDs and appropriate bandpass optical filters. The camera and computer are non-specific parts and may be replaced by comparable substitutes.

Our 2nd generation system was designed to be compact, portable, low-cost, and utilize a modular design which could incorporate a wide range of CCD cameras into the system with minimal software modifications. The hardware architecture was simplified by utilizing cameras

which allow for direct access to their exposure signals and also communicate with the computer through the IEEE 1394 Firewire bus. This removed the need for the clock card and breakout box used in the 1st generation system. To control our 2nd generation system, we developed modular, open-source GUI software programmed in C which we have named SPLASSH (SPectral Light Acquisition Software for Signaling and Hemodynamics) (Sun et al. 2010, Sun et al. 2010). The modular software architecture which comprises SPLASSH provides a simple yet highly flexible framework for high-speed multispectral optical imaging. By releasing SPLASSH's source code to the research community we hoped to make high-speed multispectral and fluorescence imaging more accessible to a larger number of dynamic imaging applications, and foster further development of the software package.

We have currently implemented this system with an AVT Pike F-032B Firewire 1394b camera, Arduino Diecimila microcontroller (SparkFun Electronics), a HP EliteBook 8510p laptop PC, a Firewire 1394b ExpressCard (EC1394B2, StarTech), and LEDs from Thorlabs (MxLED series with LEDD1 controllers) for a total cost of approximately $5,000 USD (in 2010). With only four main components, this setup easily fits into a backpack and can be assembled relatively quickly (<10 minutes) (Figure 28). This system is capable of streaming images to disk at the Pike F-032B camera's full 480 x 640 (height x width) pixel resolution and 14-bit resolution at 90 frames per second. Large increases in frame rate are possible with spatial binning and/or reduced regions of interest. Additionally, desktop computers typically offer faster internal data transfer rates and faster hard drive write speeds at the same price point as laptops, making these systems faster and more economical for a loss of portability. The portability of this setup makes it ideal for clinical use or for imaging within sterile operating rooms or animal facilities.

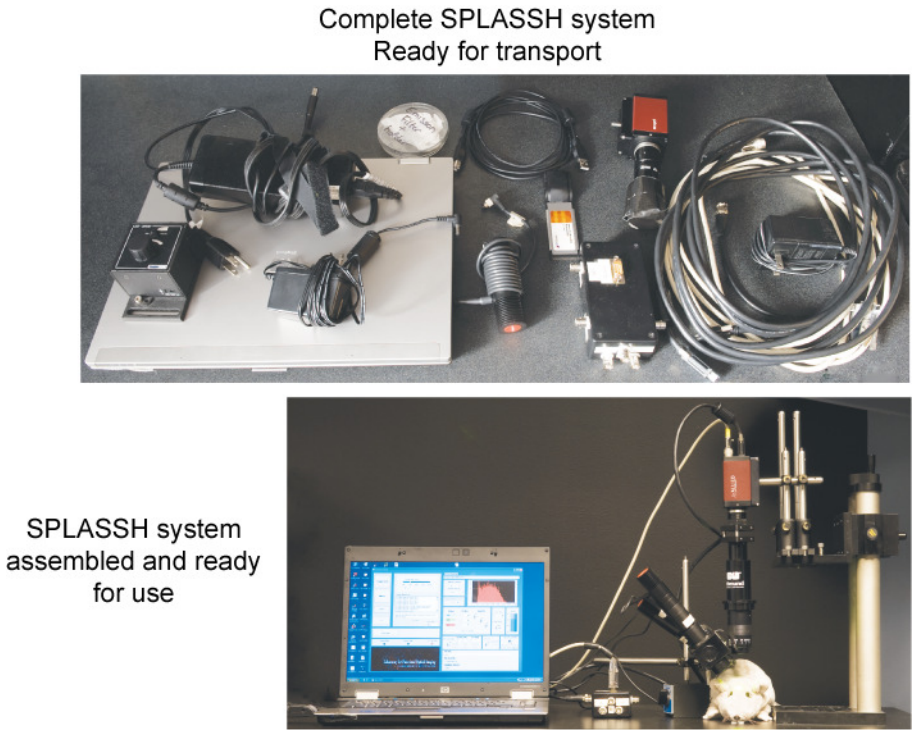

Figure 28: The complete laptop version of the SPLASSH system. (top) SPLASSH taken apart and ready for travel. (bottom) SPLASSH assembled for high-speed, multispectral wide-field 2D Optical Intrinsic Signal Imaging (OISI).

2.1.3 Release of open source system to scientific community

Part of the goal in developing SPLASSH was to create modular framework for building low-cost, ultrafast multispectral optical imaging systems. Before releasing the SPLASSH system to the worldwide science and engineering community, we developed highly commented source code and wrote a User's Manual which details all of the hardware and software necessary to replicate our system and published a paper on the system (Sun et al. 2010, Sun et al. 2010). As of this writing we have a worldwide community of 21 interdisciplinary academic and industrial users who have requested access to the SPLASSH system.

2.2 Applications of high-speed, multispectral wide-field imaging in the biosciences

We have successfully used both generations of our new high-speed, multispectral optical imaging in a wide range of functional imaging experiments. The systems have acquired data both on their own, as well as with other measurement techniques such as electrophysiology and real-time blood pressure monitoring. In this Section, we demonstrate example system configurations and the types of results produced by our systems in three typical functional imaging experiments.

2.2.1 Exposed cortex imaging in rodent brain in-vivo

While it is widely known that blood flow in discrete regions of the brain changes in response to external stimuli, the mechanisms underlying how and why this change occurs remain elusive. This poorly understood hemodynamic response underlies the popular Blood Oxygen Level Dependent (BOLD) Magnetic Resonance Imaging (MRI) technique (Kwong et al. 1992). Blood flow changes can be detected using a wide range of optical illumination wavelengths, yet the wavelength chosen can dramatically affect the conclusions that are drawn about the spatial extent and temporal evolution of the hemodynamic response (Sheth et al. 2005, Vanzetta et al. 2005, Hillman 2007, Hillman et al. 2007). This is because oxy- and deoxyhemoglobin (HbO_2 and HbR) have unique absorption spectra and exhibit different spatiotemporal responses in the vascular compartments within the cortex (arteries, veins, and capillaries) (Figure 9). A significant advance in recent years has been the use of multiple illumination wavelengths, allowing spectroscopic analysis and therefore direct estimation of the changes occurring in HbO_2 and HbR concentrations (Berwick et al. 2005, Sheth et al. 2005). High-speed spectroscopic imaging of the

exposed rodent brain allows unprecedented, simultaneous analysis of a wide range of functional parameters: 1) baseline oxygenation mapping, 2) hemoglobin oxygenation dynamics in single vessels, 3) blood vessel dilation dynamics, 4) blood flow velocity in each vessel, and 5) simultaneous imaging of hemodynamics and intracellular calcium activity (Bouchard et al. 2009, Chen et al. 2011, Kozberg et al. 2013).

A typical multispectral, wide-field 2D exposed cortex OISI experiment is shown in Figure 29. In these experiments the scalp of a rodent (typically a mouse or rat) is retracted, the skull thinned to be optically transparent (mouse, young rat) or removed completely (adult rat), and the dura (a membrane covering the brain) is removed to allow for direct observation of the brain (typical in the case of rats, atypical in the case of mice, young rats). Where the skull is removed a glass window is surgically cemented to the scalp of the animal to reduce brain swelling and brain motion artifacts (Bouchard et al. 2009, Chen et al. 2011, Kozberg et al. 2013). Somatosensory pathways in the brain are activated using electrical stimulation in the form of low current shocks (1.0 ± 0.1 mA) to the rodent fore- or hindpaw applied at low frequencies (typically 3 Hz for 0.3 – 3 ms). A stimulus control computer is used to synchronize electrical stimulation with camera image acquisition. A method to acquire spectrally resolved images of the cortex is used during camera image acquisition (See 1.2.5 for conventional methods, Section 2.1 for our new high-speed method). In experiments where only absorption measurements of hemoglobin are made, illumination wavelengths are chosen such that at least one of the wavelengths is preferentially absorbed by oxyhemoglobin, at least one by deoxyhemoglobin, and one at an “isobestic” point in the hemoglobin absorption spectra where both species of hemoglobin absorb equally (Figure 9). The Modified Beer-Lambert Law (MBLL) is then used to calculate the changing concentrations of the two hemoglobin species (Prahl 1999, Hillman

2007). In our experiments we chose 470 ± 10 nm light for oxyhemoglobin, 630 nm light for deoxyhemoglobin, and 530 ± 10 nm light for the isobestic point. The 470 nm and 530 nm wavelengths were chosen to accentuate surface vessels for our studies due to their low mean pathlength in brain tissue (LEDs: MBLED, MGLED, filters: FB470-10, FB530-10, Thorlabs). Total hemoglobin concentration changes are measured in order to calculate changes in tissue oxygen saturation ΔSO_2 (Hillman 2007).

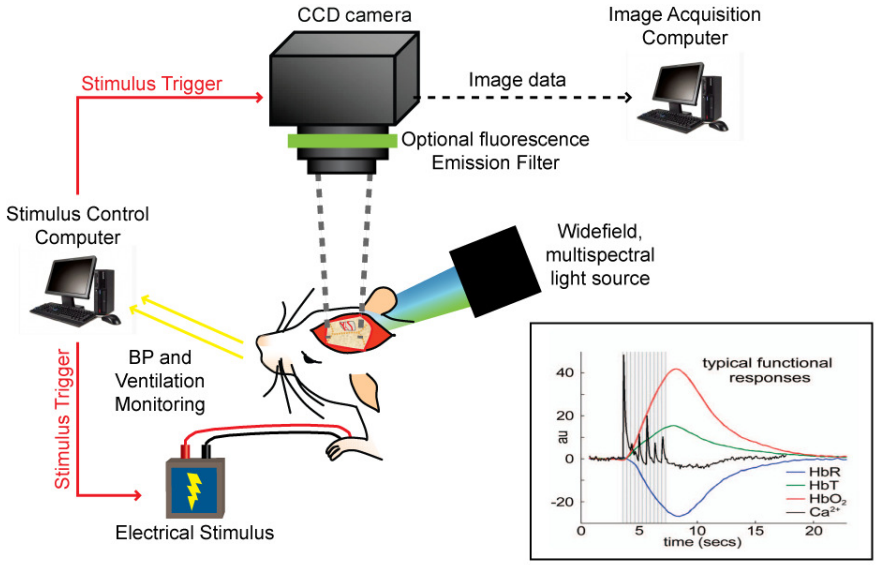

Figure 29: Optical Intrinsic Signal Imaging (OISI) experiment. In a typical OISI experiment the scalp of a rodent is retracted and the skull removed (typ. rat) or thinned (typ. mice). A wide-field, multispectral light source is used to illuminate the cortex. A camera synchronized to fore- or hind-paw electrical stimulation is used to acquire images of the cortex. At bottom right are typical functional hemodynamic and intracellular calcium responses to external stimulation. Deoxyhemoglobin (HbR), Total Hemoglobin (HbT), Oxyhemoglobin (HbO_2) and fluorescent intracellular calcium indicator. Figure modified from (Hillman 2007).

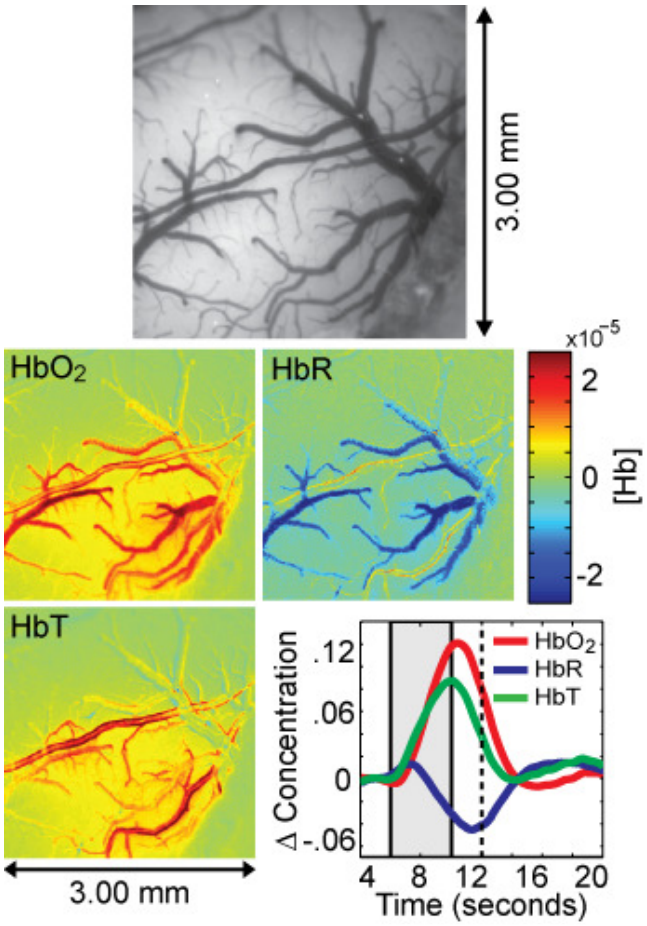

Figure 30: Example multispectral imaging of rodent cortex. Gray scale image of exposed rat somatosensory cortex. Images showing concentrations of HbO_2, HbR, and HbT at t = 11 seconds (corresponds to dotted line on time course). Time courses showing the average change in HbO_2, HbR, and HbT concentration across the entire field of view. Timing of hindpaw stimulus is shown in grey region.

To quantify the concentrations of HbO_2 and HbR we chose two LEDs with narrow bandpass filters centered at 470 and 530 nm to maximize multispectral image framerate (MBLED, MGLED, FB470-10, FB530-10, Thorlabs) (Hillman 2007) (Figure 20, Figure 30, and Figure 31). We selected shorter wavelengths than are usually chosen to accentuate the contributions of superficial pial vessels. To simultaneously image total hemoglobin (HbT = HbO_2 + HbR) and fluorescence from calcium sensitive dye Oregon Green 488 BAPTA-1 AM (Invitrogen), the 470 nm LED can be replaced with a broadband "cyan" LED fitted with a 460 ± 30 nm bandpass filter (corresponding to the excitation peak of Oregon Green), and a 500 nm

long pass dichroic filter is placed in front of the camera (MCLED Thorlabs and FF01-460/60-20, BLP01-488R-25, Semrock) (Figure 32). The 530 nm LED permits imaging of HbT responses since 530 nm is close to an isobestic point for HbO_2 and HbR. A third LED (e.g. red 630 nm center line, MRLED and FB630-10 Thorlabs) can also be incorporated into the illuminator to allow separation of HbO_2 and HbR signals as well as fluorescence imaging in parallel. Figure 32 demonstrates our system's ability to measure both hemodynamic and fluorescence dynamics in parallel. Figure 32a shows images of the exposed cortex injected with fluorescent calcium indicator Oregon Green 488 BAPTA 1-AM under 530 nm and 490 nm illumination (with a 500 nm long pass filter in front of the camera). Time courses of both calcium sensitive dye fluorescence and 530 nm reflectance for a selected region of the parenchyma can be extracted and plotted together to show the temporal relationship between neuronal activity and the hemodynamic response Figure 32b.

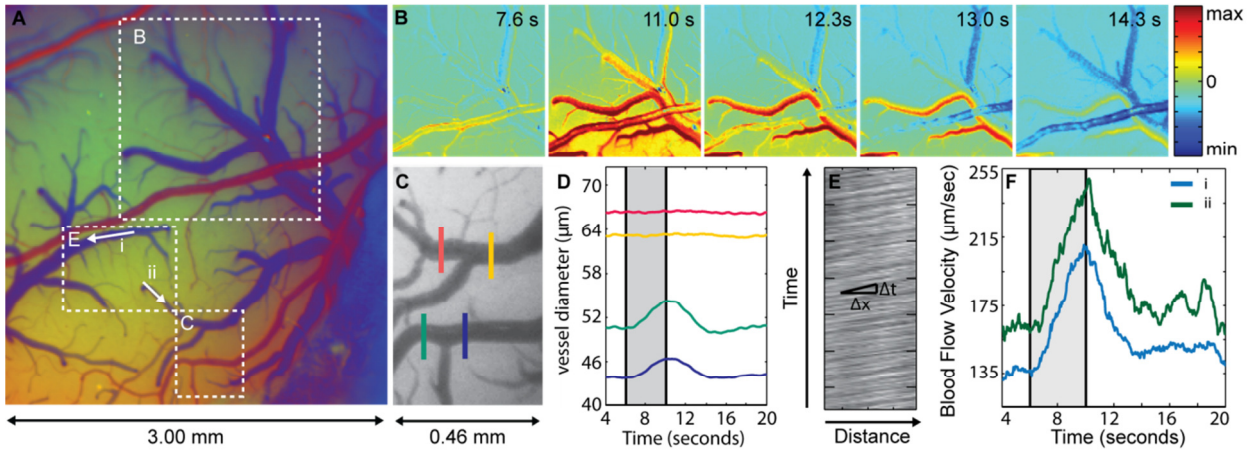

Figure 31: Examining the spatiotemporal dynamics of hemodynamic response with high-speed multispectral optical imaging. A.) RGB image created using baseline 470 nm and 530 nm images allow veins (blue) and arteries (red) to be easily distinguished. Selected regions are shown in more detail in B-F.). B.) Mixing of oxy- and deoxyhemoglobin from different vein branches combining into a single larger vein. C.) Cross sections of vein and artery used for vessel diameter analysis shown in D.). D.) Time courses of vessel diameters. E.) Matrix of line scans showing movement of red blood cells as dark stripes. F.) Time course of blood flow velocity in veins i and ii labeled in A.). Data was collected at 60 FPS and averaged across 20 trials. 4 sec stimulus started at t = 6 sec.

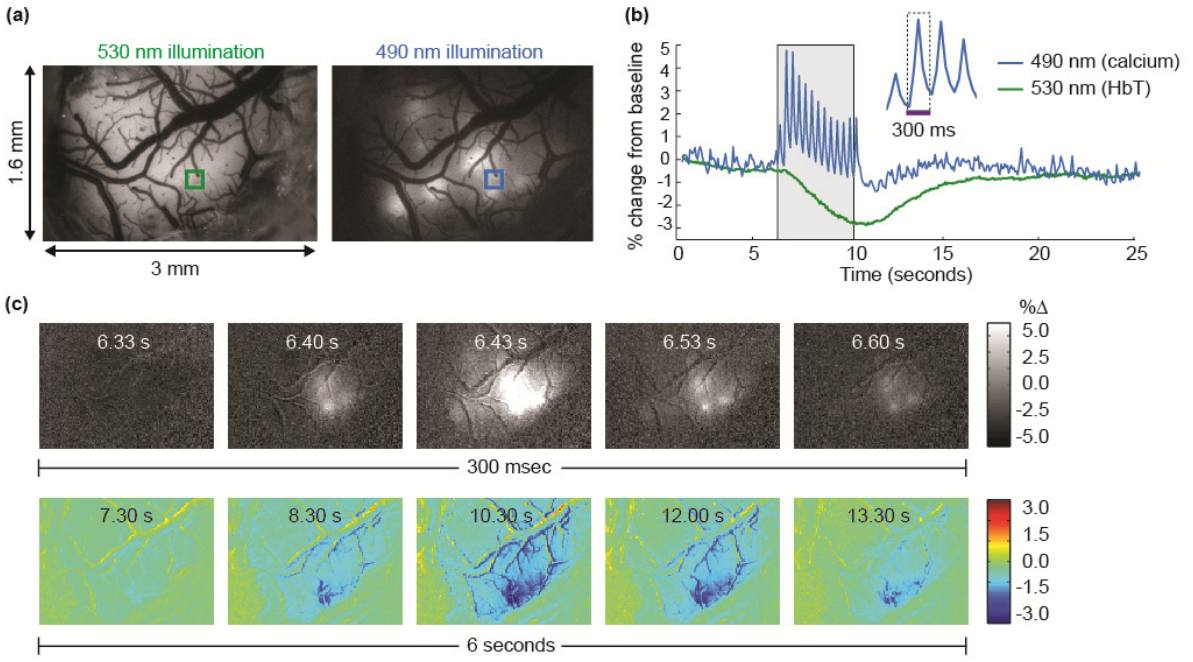

Figure 32: High speed hemodynamic and fluorescence imaging. (a) Left: Exposed somatosensory cortex under 530 nm illumination. Right: The same field of view under 490 nm illumination (with 500 nm long pass emission filter) showing fluorescence of Oregon Green 488 BAPTA-1 AM calcium indicator. The heterogeneity of the fluorescence signal is due to the discrete nature of the calcium indicator injection sites. (b) Time courses of the selected regions of the cortex indicated by green and blue boxes in (a). Duration of electrical hindpaw stimulation is shown in gray. Inset shows close-up of individual calcium "spikes". (Note that a signal decrease at 530 nm corresponds to an increase in HbT concentration) (c) Top: Images of the calcium indicator fluorescence during the evolution of the single calcium spike indicated in (b:inset) over a period of 270 ms. Bottom: Images of the change in HbT concentration calculated from the 530 nm reflectance signal showing the evolution of the hemodynamic response over a period of 6 seconds. Data was taken at 30 fps and 25 ms exposure, time averaged across 10 trials.

From these time courses, we can see rapid changes in calcium sensitive dye fluorescence that correspond to each electrical pulse delivered to the hindpaw at 3 Hz at 1.0 ± 0.1 mA, as well as the slow hemodynamic response that reaches its maximum amplitude at the end of the 4 sec stimulation period. The high temporal resolution of our system makes it possible to visualize the spatiotemporal evolution of both calcium and HbT dynamics on drastically different time scales. Figure 32c shows images of the full field of view during the evolution of a single calcium spike (over 270 ms) and the entire hemodynamic HbT response (over 6 seconds). For these images, the 530 nm signal was converted into HbT (under the approximation that 530 nm is an isobestic point for oxy- and deoxyhemoglobin). We note that the region of greatest activity during a

calcium spike co-localizes well with the region of greatest HbT change. This data set was collected with two LEDs at 30 fps with a 25 ms exposure time.

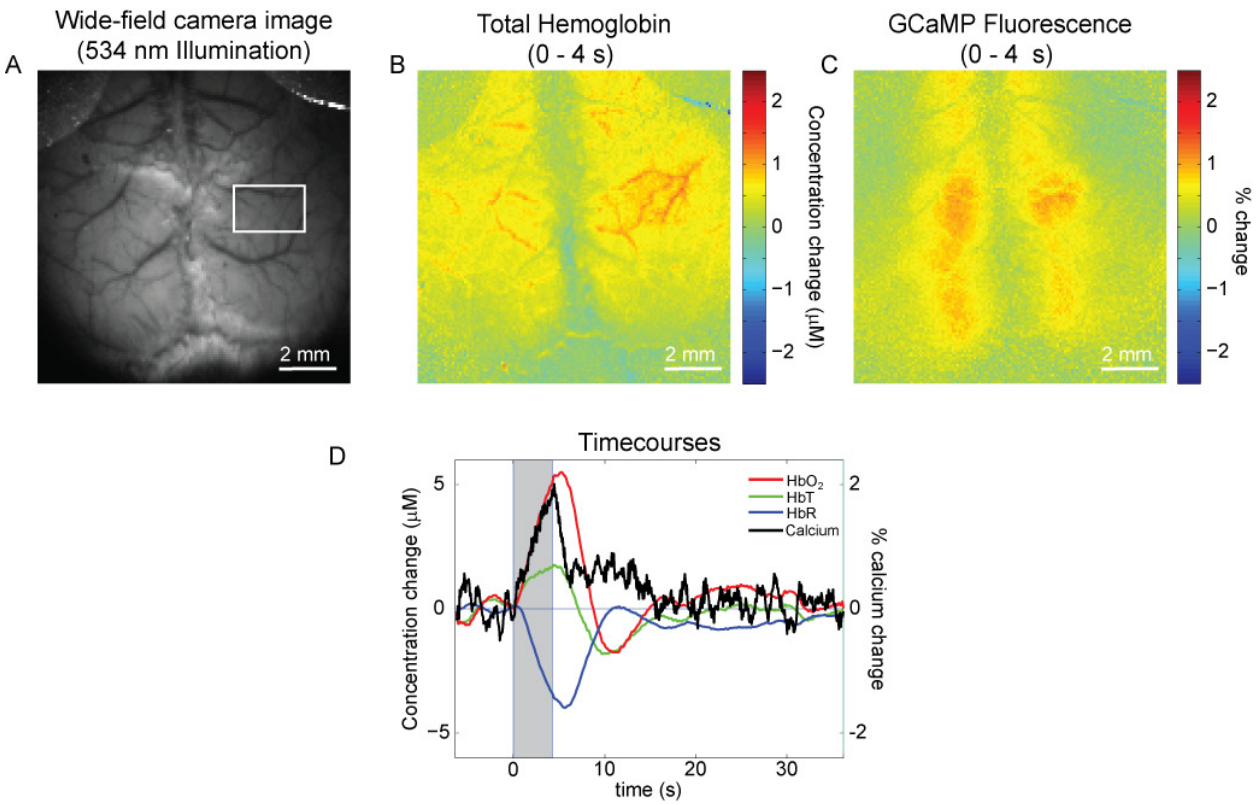

Figure 33: Imaging calcium activity in rodent cortex using a Genetically Encoded Calcium Indicator (GECI): GCaMP. A.) Image of exposed adult rat cortex taken with 530 nm center line LED light. Timecourses shown in D.) were taken from average of pixels in ROI indicated by white box located in the hindpaw region of the somatosensory cortex contralateral to the stimulated paw. B.) Difference map comparing total hemoglobin concentrations during the stimulation period to baseline concentrations. C.) Difference map comparing calcium fluorescence during the stimulation period to baseline fluorescence for the same trials. D.) Extracted timecourses of HbT, HbO_2, HbR, and GCaMP3 fluorescence taken from white box in A.). All data shown average of n = 11 trials. Stimulus parameters: 4 seconds of stimulus at 3 Hz with 3 ms stim widths and 0.7-0.8 mA amplitude. GCaMP3 imaging performed under 490 nm excitation and 500 LP emission. Thanks to M. Kozberg for data and analysis.

Recently Genetically Encoded Calcium Indicators (GECIs) have been developed which introduce active fluorophores directly into cells (Section 1.2.2). We utilized transgenic GCaMP3 rats to visualize intracellular calcium activity in response to hindpaw somatosensory stimulation (Figure 33). We provided electrical stimulation at 3 Hz with 3 ms pulse widths for 4 seconds

with 0.7 – 0.8 mA amplitude. In Figure 33A we show a wide-field camera image of the exposed somatosensory cortex under 534 nm illumination. This image is equally sensitive to both oxygenation states of hemoglobin. Figure 33B-C show difference maps between the average concentration of total hemoglobin for the 4 seconds before the stimulus and the 4 seconds of stimulus (Panel B) and the GCaMP3 fluorescence signal (Panel C). Timecourses from the ROI shown as a white box in Figure 33A are shown in Figure 33D. All time resolved data in Figure 33 are the average of 11 trials.

2.2.2 Clinical exposed cortex imaging in human brain to guide surgical planning

Functional magnetic resonance imaging (fMRI) is increasingly being used for pre-operative planning for neurosurgery. However, intra-operative MRI is expensive, obtrusive, and rarely available in most operating theatres. We used our 1st generation high-speed multispectral imaging system to demonstrate that exposed-cortex optical imaging in rodents can provide dynamic information that is equivalent to fMRI measures, and, additionally, provides information about blood flow and oxygenation dynamics that fMRI cannot. We hypothesize that the combination of pre-operative fMRI and intra-operative optical neuroimaging will allow improved identification of cortical areas critical to language and motor function and potentially for delineation of disease. This knowledge could maximize the extent of resection of brain lesions, while limiting injury to critical structures.

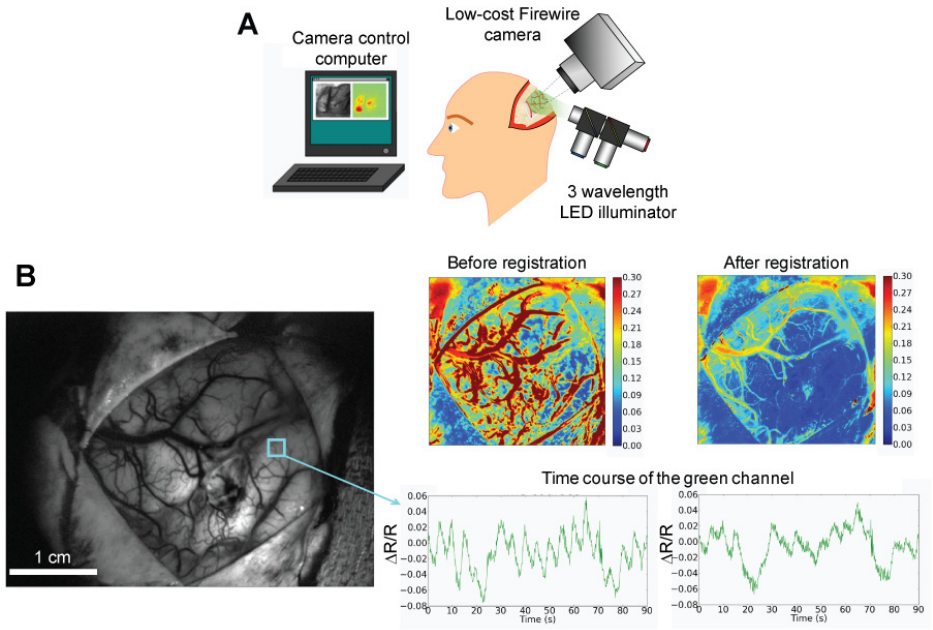

Figure 34: Clinical human neuroimaging with the SPLASSH system. a) The SPLASSH system was adapted for clinical neuroimaging by integrating the camera into a standard surgical stereomicroscope and construction of a custom mount for the LED illuminator. B) Brain motion is a significant challenge in human exposed cortex imaging. The high spatiotemporal resolution possible with the SPLASSH system due to its high framerate camera and strobed light sources enabled us to use open-source image registration software to correct for brain motion. (left) example image of exposed human cortex under 530 nm illumination. (right) images and timecourses comparing image motion artifacts before and after image registration. ΔR/R is the percent change in reflectance signal over the baseline mean signal from the first 10 images.

While intra-operative optical neuroimaging has been performed previously, it was hindered by several major practical limitations. The most significant problem was brain motion during imaging, leading to the highly invasive, time-consuming, and rarely used approach of placing a glass block on the brain to restrict movement (Haglund et al. 1992). Slow imaging speeds compounded motion problems (H. J. Noordmans et al. 2007). Our 2nd generation high-speed multispectral imaging system was designed to be highly portable. Its speed and portability enabled a much simpler approach to clinical neuroimaging. Our system allowed us to quantify and correct for motion artifacts common to exposed cortex imaging in humans using open-source co-registration software to correct for unavoidable motions using non-rigid transformation techniques. The same LED wavelengths were selected for quantification of oxy- and

deoxyhemoglobin concentration dynamics at the cortical surface as used in the rodent neuroimaging experiments (470 nm for HbO_2 and 530 nm for HbT). The SPLASSH system's portability allowed it to integrate easily with the camera port on a standard surgical stereomicroscope (Figure 35). A custom rolling mount for the LED illuminator was constructed allowing the illuminator to be positioned at any angle (Figure 34). Imaging was non-contact with a working distance ~200 mm. We have thus far measured 13 patients undergoing surgical resection of brain tumors. After the site of the tumor was localized, a craniotomy was performed and the dura reflected prior to multispectral imaging. Recent work using this system has included direct intraoperative observation of ~0.1 Hz hemodynamic oscillations in the awake human cortex, a result which has significant implications for fMRI due to its slow spatial sampling rate (Rayshubskiy et al. 2013).

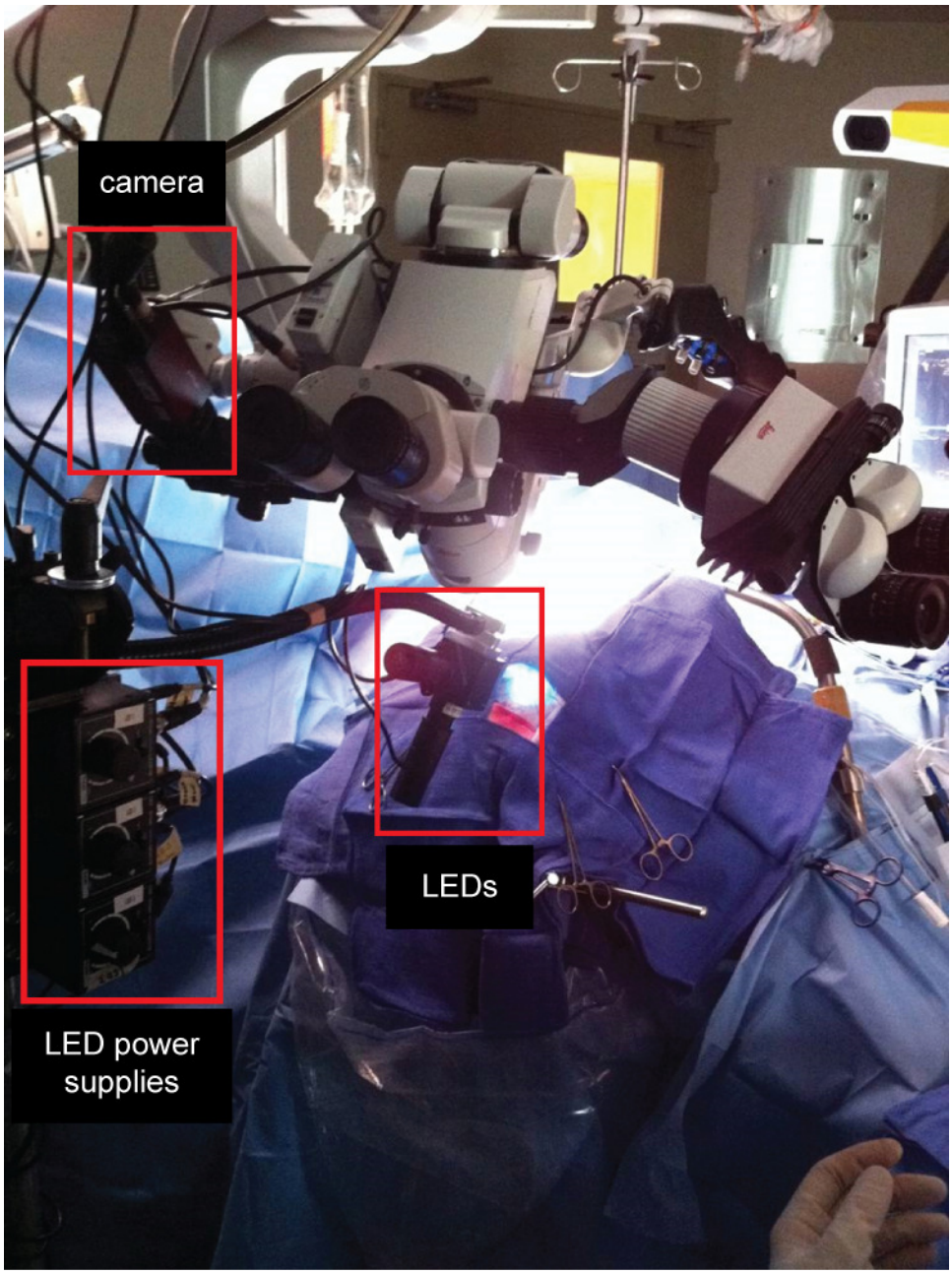

Figure 35: SPLASSH system attached to a surgical stereomicroscope in the neurosurgical operating room. The SPLASSH monochromatic camera was attached to the standard camera port on the microscope. Our high-speed LEDs were positioned using a custom illuminator arm to fill the surgical field with light.

2.2.3 High-speed imaging of cardiac stem cells

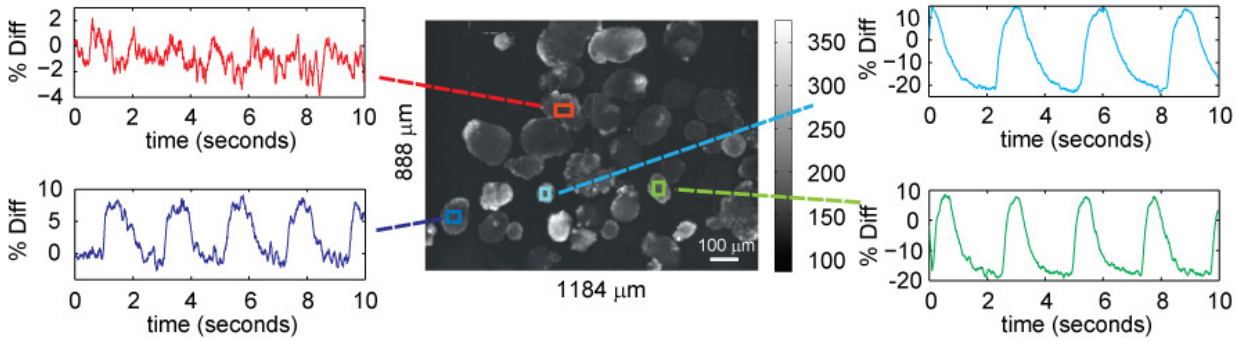

Figure 36: Imaging of intracellular calcium dynamics with high-speed functional optical imaging system. Center image shows mean calcium fluorescence from of cardiac embryoid (EB) stem cell bodies across a 10 second movie acquired at 100 frames per second. % difference timecourses show intracellular calcium dynamics from spontaneously beating EBs. Ex: 460-490 nm, Em: 515-550 nm.

Our high-speed multispectral imaging system is not limited to functional imaging of exposed cortices. The system can also be used to image at the single-cell level by mounting the camera on commercially available fluorescence microscopes (Figure 36). The broadband white light source common to most fluorescence microscopes can be used for high-speed, single channel imaging. If multispectral imaging is required, the high-power, strobed LEDs can be integrated into commercial microscopes with proper lenses and dichroic mirrors. The data shown in Figure 36 was acquired by mounting our 2nd generation system on an Olympus IX81 fluorescence microscope in collaboration with Professor Vunjak-Novakovic's Laboratory to study the calcium activity of cardiac embryoid (EB) cell bodies (Figure 37). These EBs had undergone paced electrical stimulation during development in an attempt to develop more mature tissues. Wide-field measurement of calcium activity in these EBs in the absence of stimulation can be used to determine whether the EBs "remembered" their pacing frequency across a large number of cells. Electrophysiological techniques could be used for the same measurement but they only measure the activity of single cells a time, making the experiment more time consuming and tedious. The

calcium indicator Fluo-4 was used to label the cells and a white-light source and Olympus filter cube was used to image the cells (Ex: 460-490 nm, Em: 515-550 nm). The central image shows a mean fluorescence image of cardiac embryoid (EB) stem cell bodies from a 10 second movie acquired at 100 frames per second. The percent difference timecourses show spontaneous intracellular calcium activity of beating EBs (timecourses moving averaged across 11 pixels).

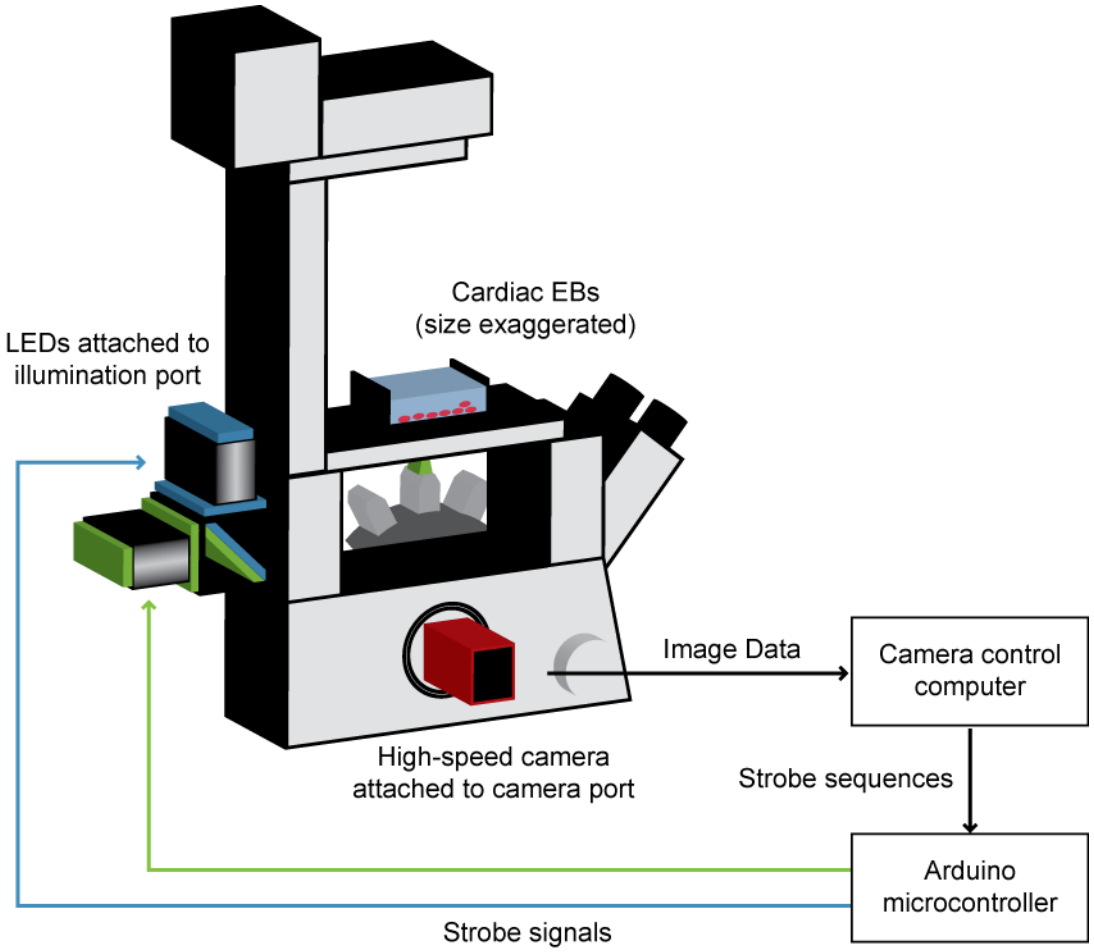

Figure 37: SPLASSH multispectral imaging system attached to commercial microscope. The SPLASSH camera attaches to the standard camera port while the multispectral LED illuminator attaches to the microscope's standard illumination port. The camera control computer and the Arduino microcontroller connect to the camera and LEDs in the same configuration as used in the functional imaging experiments. High-speed, wide-field 2D multispectral images at microscope resolutions can then be acquired using the SPLASSH control software.

2.3 Summary

We have designed, constructed, and applied two generations of our new high-speed, multispectral optical imaging system. These systems have been used to acquire optical imaging data of both absorption and fluorescence contrasts across a wide range of functional imaging experiments such as pre-clinical exposed rodent cortex neuroimaging, clinical exposed human cortex neuroimaging, and high-speed intracellular calcium dynamics. Previous multispectral imaging systems achieved published acquisition rates of 5 multispectral frames per second. Our newly developed systems can provide similar multispectral data at sustained framerates > 45 frames per second. Our 1st generation workhorse instrument has been in daily use within the Laboratory for Functional Optical Imaging since 2008 and has contributed to at least 27 journal articles and conference papers thus far. This instrument provides a functional optical imaging platform which can be easily integrated with simultaneous electrophysiological recordings as well as perform speckle flow imaging. The 2nd generation system was developed to provide a low-cost (<$5,000 total cost), portable, open-source multispectral imaging system that could be easily transported and integrated into functional imaging experiments. This system can be easily transported in a normal backpack and has been used in functional experiments ranging from clinical neuroimaging to studying calcium signaling dynamics in cardiac stem cells *in-vivo*. Both versions of the system have been used for Dynamic Contrast Enhanced imaging, a powerful small animal molecular imaging technique (Hillman and Moore 2007). As of this writing 21 interdisciplinary academic and industrial users worldwide have downloaded the open-source SPLASSH system, spurring further innovation and research into and applications of high-speed, high-resolution functional optical imaging systems.

Chapter 3 High speed, volumetric optical imaging

As evolving transgenic techniques and active contrast agents provide dynamic fluorescent markers of in-vivo processes, there is a growing need for high-speed, 3D volumetric optical microscopy methods that can capture these events *in-vivo*. *In-vivo* confocal and two-photon laser scanning microscopies have revolutionized biomedical research, but require sequential scanning to generate volumetric images at depth, intrinsically limiting their 3D imaging speeds (Holekamp et al. 2008, Grewe et al. 2010). Recent technologies such as selective plane illumination microscopy (SPIM), objective coupled planar imaging microscopy (OCPI), digital scanned laser light sheet microscopy (DSLM) have employed light-sheet illumination to great success (Figure 17). These new techniques have been used to perform diffraction-limited 3D imaging of small or transparent samples, capturing processes such as cell division and migration during early embryogenesis. Optical sectioning is achieved by illuminating the sample from the side using a thin 2D sheet of light and acquiring images using an orthogonal camera focused on the illuminated plane (Dodt et al. 2007, Holekamp et al. 2008, Huisken and Stainier 2009, Keller et al. 2010). Light sheet illumination parallelizes volumetric image acquisition and constrains photobleaching and photodamage to the plane being imaged. However, despite the parallelization provided by light-sheet illumination, even the most recent 'high speed' embodiments of SPIM have only achieved volumetric frame rates of around 0.1 – 0.05 VPS (one

volume per 10-20 seconds) (Krzic et al. 2012, Tomer et al. 2012). The main limitation on volumetric light-sheet imaging speed to date is the perceived need for mechanical translation of the sample relative to the imaging system in discrete, micron sized steps, owing to the orthogonal alignment of the illumination and imaging optics.

Additionally, the combined need for translation and side-on illumination makes sample mounting and positioning highly challenging, limiting the types of samples that can be imaged (Dunsby 2008). Furthermore, in scattering samples, an orthogonal light-sheet does not remain thin, and in some cases cannot propagate completely across the sample for full illumination (Dodt et al. 2007, Krzic et al. 2012, Tomer et al. 2012). Tissue clearing can reduce scattering, but is time-consuming and necessarily kills the specimen (Dodt et al. 2007, Hama et al. 2011, Chung and Deisseroth 2013). The alternative approach is to acquire multiple views of the sample by rotating it, or using multiple objectives to illuminate and image from different sides to generate isotropic illumination (Krzic et al. 2012, Tomer et al. 2012). However, these approaches further slow volumetric acquisition speeds, and severely restrict the size and shape of samples that can be mounted and imaged, and significantly increase system complexity and cost. Even with these limitations in mind we were intrigued by the relative simplicity of these systems and the exquisite images they were able to produce of living biological systems.

We started development of the Laser-Scanning Intersecting Plane Tomography (L-SIPT, Figure 39) because we wanted to explore the use of light-sheet illumination for high-speed functional imaging, specifically cortical brain imaging (Section 1.3.2). L-SIPT uses a novel combination of light-sheet illumination and off-axis detection to provide *en-face* 3D imaging of samples. L-SIPT allows samples to move freely in their native environments, enabling a range of experiments not possible with previous 3D optical imaging techniques. The constructed system

is capable of acquiring 3D images at rates >20 volumes per second (VPS) with volume resolutions of 1400 x 50 x 150 pixels for the lateral, scan, and depth axes, respectively, over a 200 fold increase over typical laser scanning microscopes. Spatial resolution is set by choice of telescope design. We developed custom opto-mechanical components, computer raytracing models to guide system design and to characterize the technique's fundamental resolution limits, and phantoms and biological samples to refine the system's performance capabilities. We developed initial applications of the system including the measurement of *ex-vivo* and *in-vivo* transgenic *Drosophila Melanogaster* larvae, intracellular calcium activity in acute murine brain slices, and neurovascular activity in exposed rodent cortex.

3.1 State of the art for volumetric optical imaging

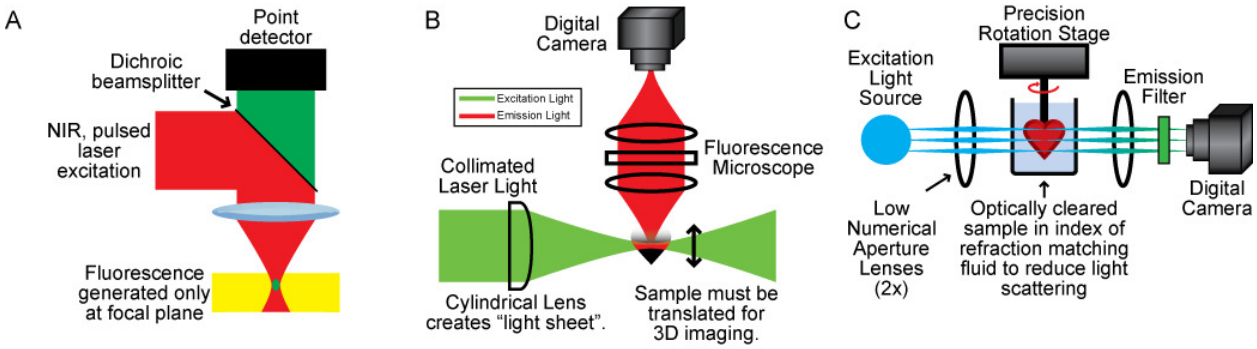

Advantages
- Diffraction limited 3D resolution
- *en-face* imaging geometry
- Multiple sources of contrast available

Disadvantages
- Voxel-by-voxel image construction typical.
- Multi-spot approaches limit depth and resolution
- Random scanning approaches reduce and bias field-of-view
- Increased rates of photobleaching and photodamage

Advantages
- Diffraction limited 3D resolution
- Increased volumetric acquisition rates
- Constrains photobleaching and photodamage to imaged plane

Disadvantages
- Imaging geometry restricts types of samples which can be imaged
- Requires translation of sample relative to imaging system
- Only sensitive to fluorescence
- Cannot image freely moving samples
- Requires optical clearing for large and/or scattering samples

Advantages
- Mesoscopic resolution (~10 μm^3)
- Sensitive to both absorption and fluorescence
- Samples preserved for subsequent histology

Disadvantages
- Requires optical clearing for large and/or scattering samples
- Limited to samples ~1 cm3 in size
- Requires ~400 images per acquisition
- Cannot image freely moving samples

Figure 38: State of the art for volumetric optical imaging. Three approaches to volumetric optical imaging, their advantages and disadvantages for functional optical imaging. A.) laser-scanning two photon fluorescence microscopy. B.) Light-sheet illumination microscopy. C.) Optical Projection Tomography.

Any optical imaging technique which can isolate optical signal(s) from precise locations in 3D space to create volumetric images performs optical sectioning. A variety of different imaging techniques can perform optical sectioning. Within volumetric functional optical imaging laser-scanning microscopy is the most well-established technique. New techniques such as the light-sheet illumination geometries SPIM, DSLM, OCPI, OPM, and others, as well as the optical analogue to x-ray computed tomography, Optical Projection Tomography (OPT), have made

new advances in the size of and the speed with which volumes can be imaged. However, each technique imposes theoretical and practical limits on image acquisition speeds, the types of samples which can be imaged, and the types of experiments which can be practically performed.

Laser-scanning microscopies: Confocal and non-linear microscopies

Laser-scanning microscopy is a mature, well corrected optical imaging technique which can provide diffraction limited 3D images of samples *in-vivo* at depths greater than 500 μm (two photon fluorescence) and utilizes simpler *en-face*, illumination. This imaging geometry is ideal for functional cortical imaging experiments because illumination and detection light are delivered via the sample objective. Additional modes of contrast including Fluorescence Lifetime Imaging Microscopy FLIM), Fluorescence Resonance Energy Transfer (FRET), and multispectral techniques are commercially available and widely utilized. However, laser-scanning is most commonly implemented via sequential scanning in which the image is constructed pixel by pixel. Sequential scanning intrinsically limits their 3D imaging rates, increases rates of photobleaching and photodamage, and limits their ability to perform real-time volumetric imaging of samples *in-vivo* (Holekamp et al. 2008, Grewe et al. 2010). For example, common laser scanning microscopes can acquire pixels at a rate of 1,000,000 per second, meaning a volume discretized into 100 x 100 x 100 pixels can be acquired with a volumetric framerate of 1 Hz, not fast enough to measure dynamic *in-vivo* processes such as intracellular calcium signaling (Bouchard et al. 2009). Multi-spot imaging approaches can increase their volumetric framerates at the cost of reduced depth penetration, reduced spatial resolution, and increased instrumentation complexity (Bahlmann et al. 2007).

Light-sheet volumetric imaging

Light-sheet volumetric imaging techniques (Section 1.3.1) achieve optical sectioning by illuminating minimally- to non-scattering fluorescent samples with a thin sheet of excitation light (~1 μm). A fluorescence microscope oriented normal to the light-sheet acquires 2D optically sectioned images of the sample. Volumetric images are constructed from 2D of images of the sample as it is translated through the light sheet in micron sized steps (Dodt et al. 2007). Some implementations additionally construct the sheet by scanning a line through the sample at each depth plane to improve spatial resolution by avoiding resolution losses due to scattering (Keller et al. 2010). Diffraction limited resolution can be achieved throughout the sampled volume with the addition of multiview imaging to the image acquisition protocol (Verveer et al. 2007, Krzic et al. 2012, Tomer et al. 2012). Light-sheet imaging techniques can acquire volumetric data faster than laser-scanning microscopy because they inherently parallelize data acquisition. For each "measurement" in light-sheet imaging a full plane is acquired whereas in each measurement in laser-scanning microscopy a single voxel is acquired, meaning the sampling time per voxel is increased many thousand fold in the case of light-sheet imaging. However, despite this parallelization, even the most recent 'high speed' embodiments of SPIM have only achieved volumetric frame rates of around 0.1 – 0.05 VPS (one volume per 10-20 seconds) (Krzic et al. 2012, Tomer et al. 2012). The main limitation on volumetric light-sheet imaging speed to date is the perceived need for mechanical translation of the sample relative to the imaging system in discrete, micron sized steps, owing to the orthogonal alignment of illumination and imaging optics (Dodt et al. 2007, Verveer et al. 2007, Holekamp et al. 2008, Keller et al. 2010). Additionally, the combined need for translation and side-on illumination makes sample mounting and positioning highly challenging, limiting the types of samples that can be imaged (Dunsby

2008). Furthermore, in scattering samples, an orthogonal light-sheet does not remain thin, and in some cases cannot propagate completely across the sample for full illumination (Dodt et al. 2007, Krzic et al. 2012, Tomer et al. 2012). Tissue clearing can reduce scattering, but is time-consuming and necessarily kills the specimen (Dodt et al. 2007). The alternative approach is to acquire multiple views of the sample by rotating it, or using multiple objectives to illuminate and image from different sides to generate isotropic illumination (Krzic et al. 2012, Tomer et al. 2012). However, these approaches further slow volumetric acquisition speeds, and severely restrict the size and shape of samples that can be mounted and imaged (samples must be constrained to the imaged volume), and significantly increase system complexity and cost.

Optical Projection Tomography: visible light computed tomography (CT)

Optical projection tomography (Section 1.3.1) is the visible light-analogue to x-ray computed tomography. It acquires projection images of samples and reconstructs 3D volumes using backprojection reconstruction algorithms. It can be used to acquire optically sectioned images of both absorption and fluorescence contrast, has been implemented using Fluorescence Lifetime Imaging Microscopy (FLIM), provides mesoscopic resolution (~10 μm^3), and the imaged samples are preserved for subsequent histology (Sharpe et al. 2002, Sharpe 2003). However, OPT requires scattering samples to undergo complex chemical optical clearing procedures to render them transparent or nearly transparent for imaging (~2 days). Even with optical clearing procedures, OPT has been limited to samples ~1 cm^3 in size. Typical OPT acquisition sequences acquire ~400 projection images per reconstruction, precluding the use of OPT to image dynamic samples *in-vivo*.

3.2 Laser-Scanning Intersecting Plane Tomography

Laser-Scanning Intersecting Plane Tomography (L-SIPT) is our novel approach to volumetric optical imaging (Figure 39). Its laser-scanned, single lens, *en-face*, non-contact, theta imaging geometry is unique among the new light-sheet imaging techniques and enables high-speed volumetric optical imaging orders of magnitude faster than existing technologies (>20 VPS for volumes 1400 x 50 x 150 pixels^3 in size for the lateral, scan, and depth axes, respectively). L-SIPT uses off-axis detection optics to acquire fluorescence data from laser-scanned oblique illumination planes through a single lens. This means that high resolution imaging can be achieved in superficial layers of the sample's top surface in scattering samples, to the depth limit at which the sheet remains thin and the detected light can emerge without significant distortion. While this means that isotropic resolution is not achieved (as in multi-view SPIM), far fewer limits are imposed on the type and size of intact samples that can be imaged. We used home-built custom raytracing code and a commercially available optical design software package to guide understanding of the L-SIPT imaging principle and to drive optimization of the system's imaging optics. We incorporated a commercial image splitter device originally designed for epi-fluorescence microscopes to acquire simultaneously two spectrally separated fluorescence channels without a loss in spatial resolution. In this Section we describe the design and implementation of the L-SIPT system.

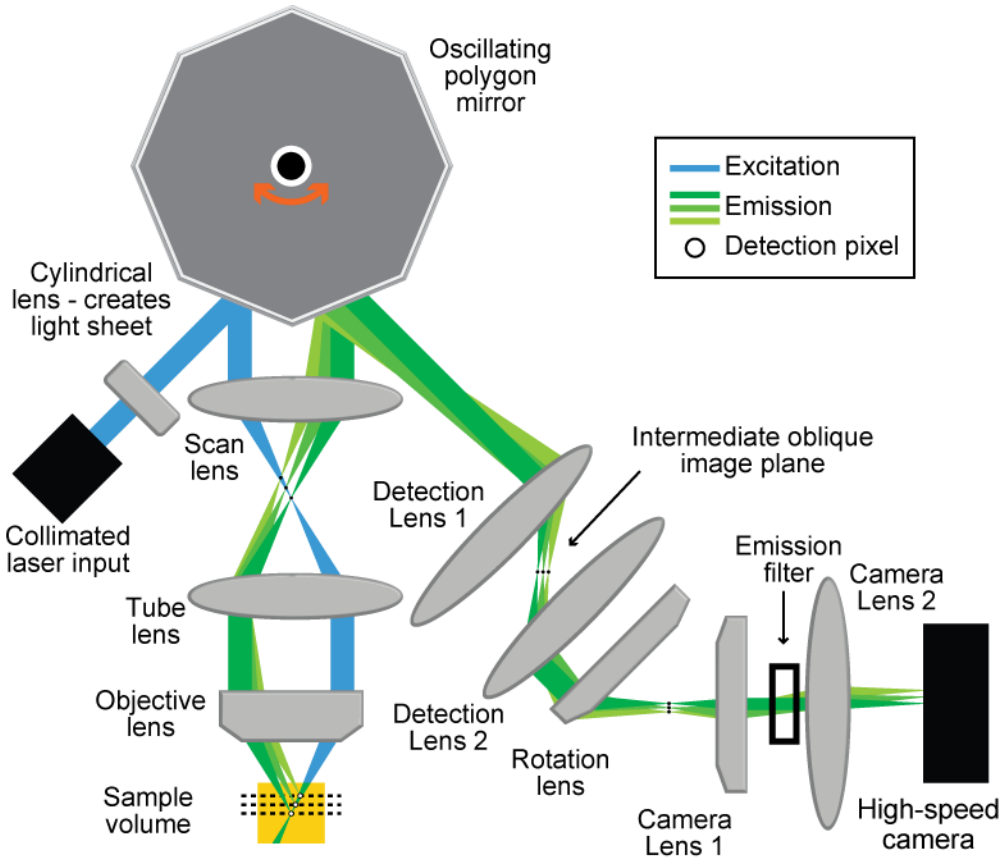

Figure 39: Single-channel Laser-Scanning Intersecting Plane Tomography system geometry. L-SIPT is similar to a single-lens, line-scanning confocal theta microscope. An oscillating polygon mirror (or other scanning element) scans an oblique fluorescence excitation light-sheet through the sample volume (blue rays), and de-scans returning light such that images of the moving fluorescence plane (green rays) remain focused on a stationary 2D detector array. The only moving component is the polygon mirror. The sample can be fixed or freely moving within the scanned volume. Inset: close-up of oblique illumination and measurement geometry, a full 3D volume is created from a stack of oblique planes acquired during a single sweep of the scanner's facet. This means that raw L-SIPT data has a non-Cartesian coordinate system defined by the major axes of the illumination light sheet and its translation axis through space. Here, we define these coordinate axes as 'lateral', 'depth' and 'scan' axes. All data shown here is in this L-SIPT 'raw' coordinate system, although scan pattern-related distortions can be mapped back into Cartesian space using ray-tracing models.

3.2.1 Fundamental concept

The Objective-Coupled Planar Illumination (OCPI) microscopy system was the first of the light-sheet technologies to image exposed cortex *in-vivo* (Figure 40) (Holekamp et al. 2008, Turaga and Holy 2012). The OCPI system rigidly couples the illumination optics to the objective lens. This assembly is then mounted on a high-speed piezoelectric translation stage, creating a

relatively cumbersome instrument (Figure 40A-C). OCPI has largely been used to acquire images of oblique illumination planes at high speeds (>200 fps) and not full volumetric images which would allow for analysis of complete neurovascular circuits (Figure 40D). Even so, we were inspired by OCPI's ability to image high-speed neuronal signaling in oblique depth planes in living cortex. We sought an imaging geometry which could take advantage of the significant parallelization of data acquisition offered by light-sheet illumination but also maintain the relative simplicity of the non-contact, *en-face* imaging geometry used by laser scanning microscopy.

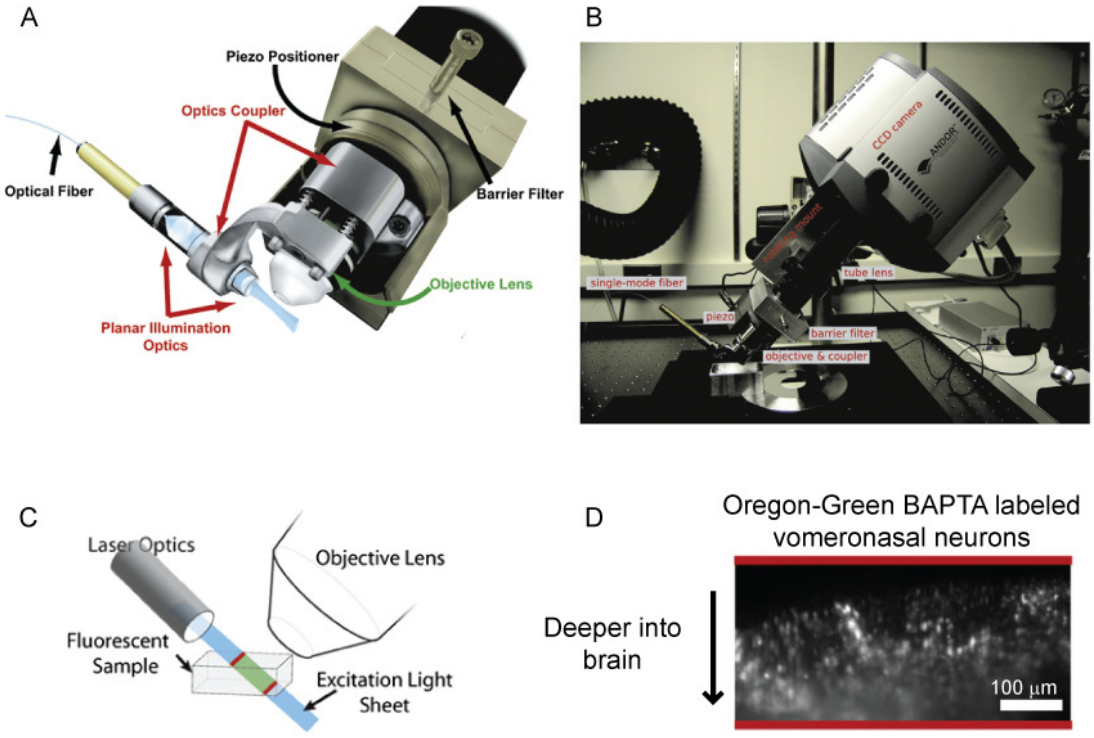

Figure 40: Objective Coupled Planar Illumination (OCPI) microscopy. A.) OCPI rigidly couples the illumination light sheet (delivered via fiber-coupled illumination) to the objective lens. The objective lens/illumination assembly is attached to a piezoelectric translation stage which moves the sheet/objective lens assembly relative to the sample to acquire volumetric image stacks. B.) Photograph of completed system. C.) OCPI's illumination geometry was developed to image in the exposed cortex *in-vivo*. D.) Example oblique depth plane of vomeronasal neurons labeled with Oregon-Green BAPTA, an exogenous, active fluorophore sensitive to intracellular calcium concentration changes. Figure adapted from (Holekamp et al. 2008).

The line-scanning confocal theta microscope (LSCTM) uses a single lens, *en-face*, non-contact imaging geometry with separate illumination and detection paths to improve the axial resolution over standard, single path confocal microscopy (inset, Figure 41). This is accomplished by overlapping distinct line spread functions (Dwyer et al. 2006, Dwyer et al. 2007). LSCTM uses a cylindrical lens placed before the objective lens to create a focused line in the objective's focal plane. A dual-faceted prism mirror is used to direct scanned light to one side of the objective lens (not shown in Figure 41). Detected light originating from the focused line which travels a path symmetrical to the illumination light is collected by the objective and descanned by the second facet of the scanning mirror before being focused onto a linear slit spatial filter to perform confocal optical sectioning. The axis of the linear detector is out of the page. We recognized the similarities in the illumination paths between the new light sheet microscopies and the line-scanning confocal theta microscope. Both systems generate a plane of fluorescence; the light-sheet systems detect the entire plane while the confocal theta microscope restricts itself only to the best focused part of the plane.

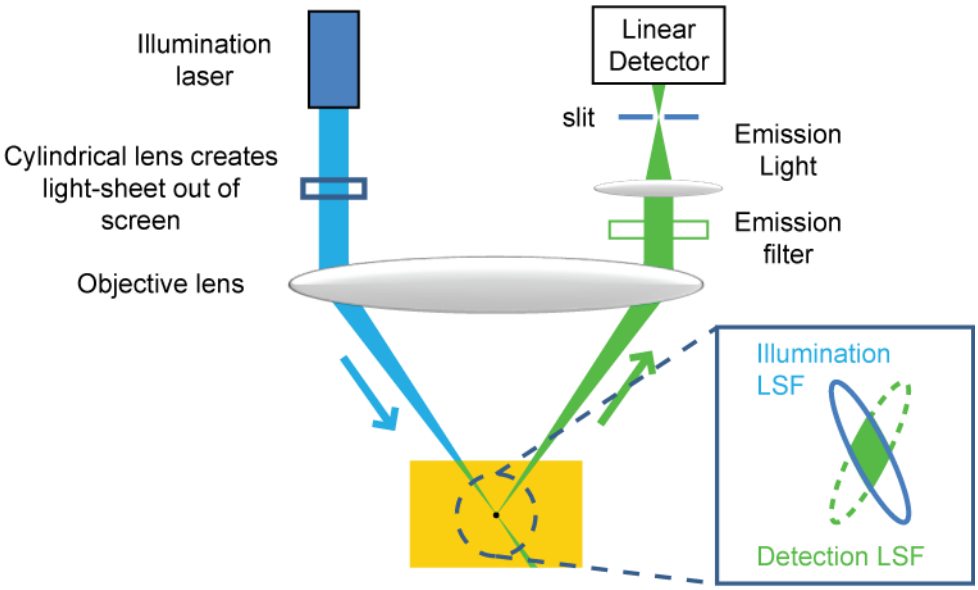

Figure 41: Line-scanning confocal theta microscopy imaging geometry. Line-scanning confocal theta microscopy (LSCTM) uses separate illumination and detection paths to improve its axial resolution over standard single lens confocal microscopy. A cylindrical lens placed before the objective lens creates a focused line in the focal plane of the objective lens (line out of the page). Collected emission which travels a path symmetrical to the illumination beam is focused onto a linear slit spatial filter and detected using a linear detector array. A prismatic mirror mounted on a single axis galvanometric scanner (not shown) is used to scan the line across the objective lens' focal plane to construct 2D images.

We wondered what would happen if you removed the spatial filter slit from in front of the line detector and rotated the detector 90° such that the plane of the detector was in line with the plane of the page. To complete this thought experiment, we considered what would happen when imaging a 2D fluorescent object and traced light rays originating from adjacent positions to the focused line in the focal plane back along the detection arm and found that they mapped to different lateral positions on the detector (Figure 42). Because these detection paths intersected the illumination plane, light originating from depths above the objective's focal plane can be detected by a single linear array detector. Incorporating a cylindrical lens to generate a plane of light out of the sheet of the paper, we can replace the linear detector array with a 2-dimensional detector array (like a CCD camera) to detect an oblique plane of fluorescence in the sample. However, the emission light originating from planes away from the focal plane becomes

progressively harder to detect due to the broader point spread functions of both the illumination and detection arms where they intersect. This effect would be manifested as a loss in imaging resolution and loss of signal to noise from emission sources away from the focal plane.

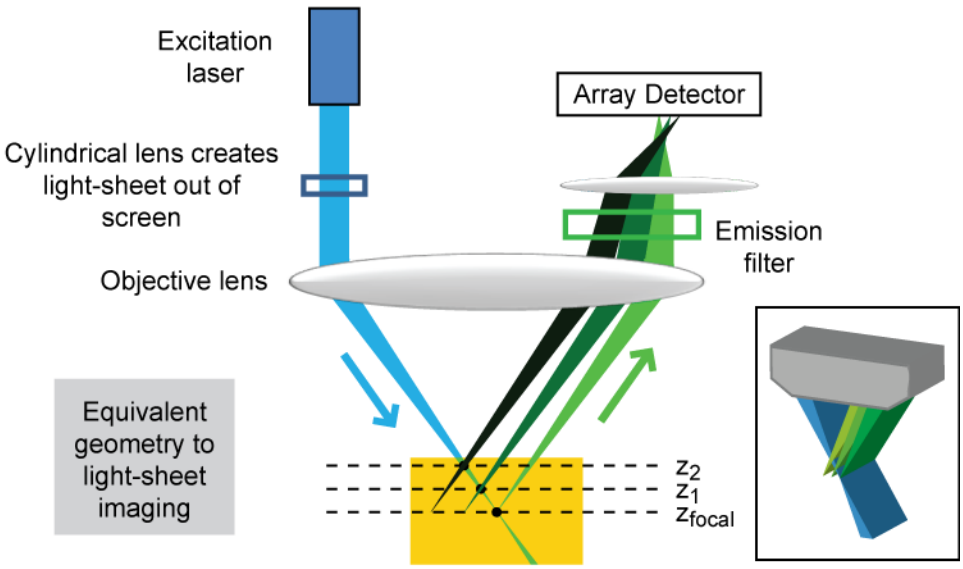

Figure 42: Basic, unoptimized L-SIPT imaging principle. Signal from an oblique illumination plane can be detected by removing the slit spatial filter used in laser-scanning confocal theta microscopy and replacing it with an array detector. However, signal originating from depths away from the objective lens' focal plane (z_{focal}) will be of reduced image quality due to the larger size of the overlapping line spread functions. (inset) 3D rendering of imaging geometry showing overlap between excitation plane (blue) and emission light originating from locations adjacent to the center of the focal plane (green).

3.2.2 Geometrical raytrace modeling and first L-SIPT images

Even though the signal originating from planes away from the objective lens' focal plane would likely be of low imaging quality (reduced resolution and reduced SNR), we set out to determine whether the illumination and detection planes would overlap when the illumination beam was scanned. To answer this question we developed custom geometric raytracing software in MATLAB based around a graphical user interface (GUI) which allows the user to modify all system design properties. Raytracing was performed with knowledge of the positioning of all optical surfaces in the model, including the size and shape of lenses' surfaces and lenses' index

of refraction. The refraction angles of each ray at each lenses' surface were calculated using Snell's Law. Reflection at mirror surfaces was calculated using the Law of Reflection.

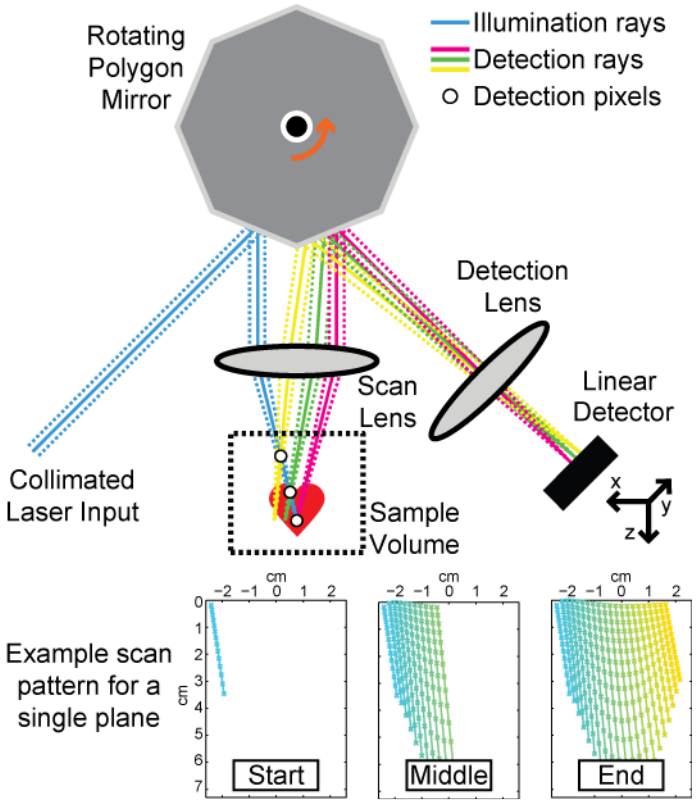

Figure 43: First L-SIPT system design modeled with custom raytracing software. This system only scanned 2D planes (parallel to the page). (bottom): Example scan pattern modeled using geometric raytracing software shows evolution of L-SIPT sweep. Each line corresponds to the mapped location in the sample of the linear detector.

Initially we simplified this model by modeling L-SIPT as a single plane scanning system and leaving the cylindrical lens out (Figure 43). We included the minimum number of lenses necessary to perform L-SIPT: a single scan lens and a single detection lens. The LSCTM used a custom prism-mounted galvanometric scanner to scan its illumination beam (90° wedge prism) (Dwyer et al. 2006, Dwyer et al. 2007). This prism had two rigidly mounted mirror image surfaces which were used to scan the illumination beam and de-scan the detection beam. We chose to use an 8 sided polygon scanner because it was commercially available and offered the similar rigidly mounted mirror image surfaces as the custom prism scanner with the additional

benefit of compacting the reflected image of the illumination beam along the scan lens' optical axis. This property is important in the full version of L-SIPT which utilizes a scanning telescope to meet the telecentric condition (Tsai et al. 2002). As the polygon mirror is rotated about its rotation axis, the illumination beam is scanned. To model the intersection between the illumination and detection planes we launched rays from two locations in the model: collimated rays from the input laser beam and divergent rays from the detector plane (which was located one focal length away from the detection lens). We recorded detector pixel locations where the Central Ray for each detector intersected the Central Ray for the illumination beam at a given scan angle (shown as a 3 step progression for a full sweep in Figure 43, bottom). Each detector pixel location at a given sweep angle is indicated by a cross. The map constructed in this way models the full L-SIPT scan pattern for a single plane. This forward model coordinate transform revealed that this configuration of L-SIPT has a non-regular scan pattern; however, it could allow us to map acquired data, which is in scan angle / detector-separation space to a Cartesian coordinate system. To test this hypothesis we generated a synthetic L-SIPT phantom in MATLAB (Figure 44, left), modeled what the phantom would look like in L-SIPT scan space by running it through the forward model (Figure 44, middle), and then reconstructed the synthetically scanned data (Figure 44, right), achieving an accurate reconstruction of the original phantom. This exercise demonstrated the reconstruction procedure L-SIPT data will need to undergo to be transformed from the raw L-SIPT, non-Cartesian coordinate system to the Cartesian laboratory system. However, later experiments showed that for small samples raw L-SIPT data retains Cartesian behavior and suitable images can be rendered without remapping (Figure 45).

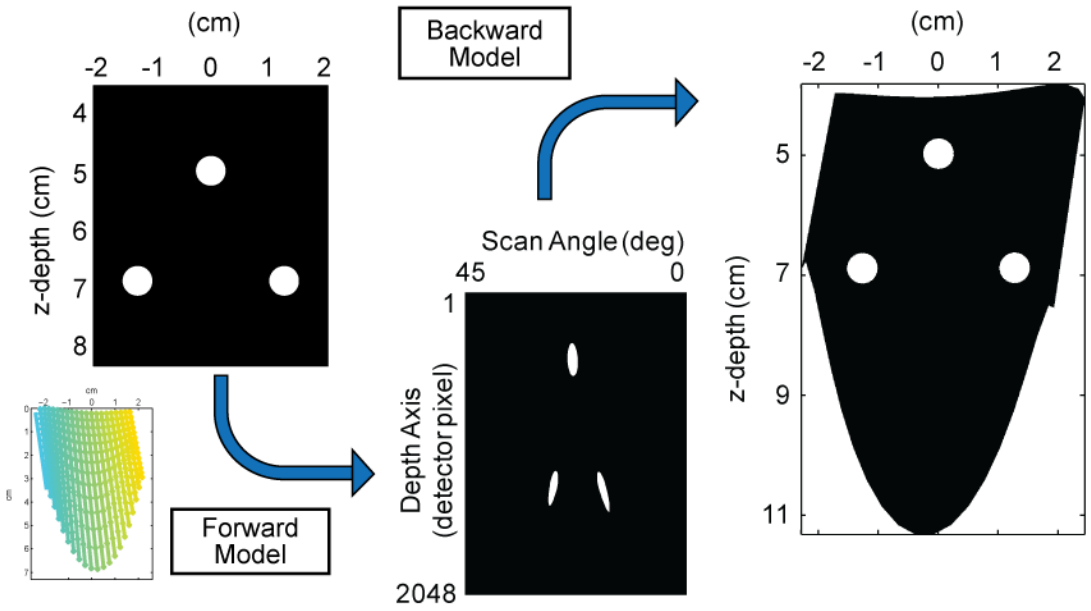

Figure 44: Computer simulated fluorescent phantom data "scanned" using L-SIPT's forward model developed from a geometric raytrace. (left). Simulated raw L-SIPT data exists in a scan angle/depth axis coordinate system (middle). Reconstructed data using backward model accurately reconstructs phantom positions. (right).

3.2.3 Scanning an oblique illumination plane: first L-SIPT images

With the raytracing model showing that L-SIPT scans a single plane, we next built a prototype version of the system following the same schematic in Figure 43. We used off the shelf components largely from Thorlabs to construct the system. Two achromatic doublets with focal lengths of 75 mm (AC508-075-A1, Thorlabs) were used initially as the scan and detection lenses due to their high Numerical Apertures (NAs) for 2" diameter lenses. We chose large lenses to minimize off-axis aberrations such as spherical and comatic aberrations. A 675 nm laser diode was used for illumination. We first scanned a single plane of a "mesoscale" sample consisting of thin polyethylene tubes filled with a Near-Infrared (NIR) fluorescent dye arranged in the 3D arrangement shown in Figure 45A left. Figure 45A center shows a hand drawn schematic of the sample in MATLAB while Figure 45A right shows the L-SIPT reconstruction of the scanned sample using the forward model developed from our raytracing model. Comparison of the hand

drawn schematic and the reconstruction shows that L-SIPT was able to accurately reconstruct the 2D distribution of the fluorescent tubes. We next scanned a single plane of a "microscale" sample consisting of 0.07 mm thick piece of fluorescent plastic arranged in the shape of the letter M (Figure 45B left). For this sample we used a commercial 4x objective lens (effective focal length 45 mm). Figure 45B center shows a hand drawn schematic of the phantom while Figure 45B right shows the raw L-SIPT scan data. This image intrigued us due to its striking resemblance to the real shape of the phantom. This result implied that for microscale imaging L-SIPT's scan pattern had Cartesian qualities to it, at least for regions near the objective's focal plane.

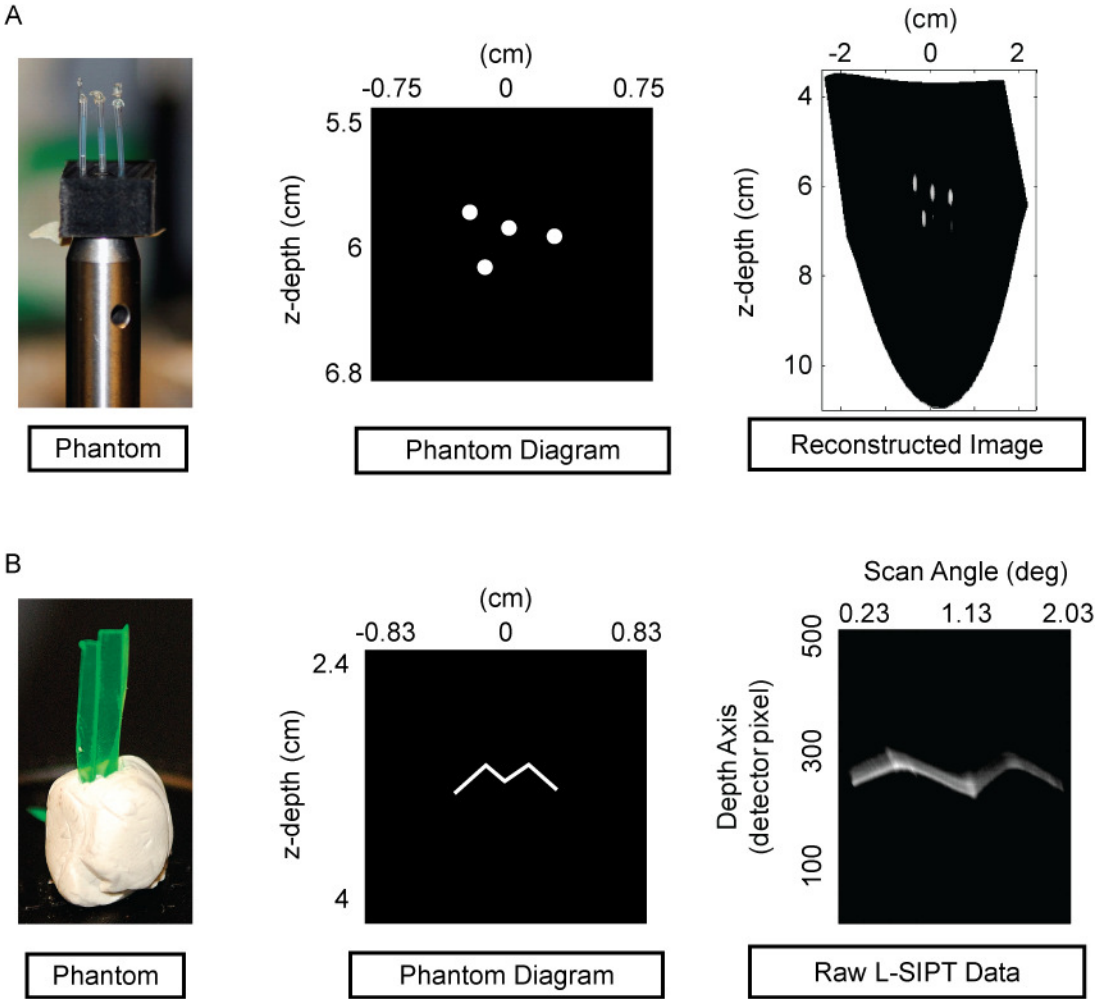

Figure 45: First planar L-SIPT results. A.) phantom consisting of 0.6 mm outer diameter polyethylene tubes filled with a NIR fluorophore was imaged using a macroscale lens configuration (1x magnification). Image was reconstructed using our forward model. B.) A 0.07 mm thick piece of fluorescent plastic in the shape of the letter M was imaged using a 4x microscope objective, illustrating microscale depth discrimination. Image at right is raw L-SIPT data.

Now that we had demonstrated that L-SIPT was able to accurately image meso- and microscale samples in 2D we next sought to demonstrate that L-SIPT could resolve objects in 3D. Since our prototype system had a linear array detector we performed a proof of concept experiment in which we acquired a series of planar images as we translated an object through the scan plane in discrete to build a 3D image (top left, Figure 46). We used the L-SIPT reconstruction procedure detailed in Figure 44 and cropped the resulting images for Figure 46.

Two polyethylene tubes were filled with differing concentrations of a NIR fluorophore (one twice the concentration of the other) to identify them via their signal strengths. 38 scans were acquired with a 0.127 mm x-step size and were stitched together via post-processing using Amira (top right, Figure 46). In the bottom row of Figure 46 we show select depth planes from the 3D stack which shows the tubes coming together at the middle of the "X" shape. Where the tubes cross (plane x_3) we see that one tube disappears from the image because it was shadowed by the other. This is an effect common to optical imaging techniques whereby an absorbing and/or scattering object prevents light from reaching deeper depths in samples.

The accurate reconstruction of the 3D shape of the phantom demonstrated L-SIPT's ability to image in 3D. However, this demonstration required serial translation of the object along the lateral L-SIPT axis and multiple sweeps of the scanner to build a 3D image. To perform true high speed 3D imaging of freely moving objects we wanted to be able to acquire a full 3D image with a single sweep of the scanner. We next modified the L-SIPT prototype system to see if this were possible using light-sheet illumination.

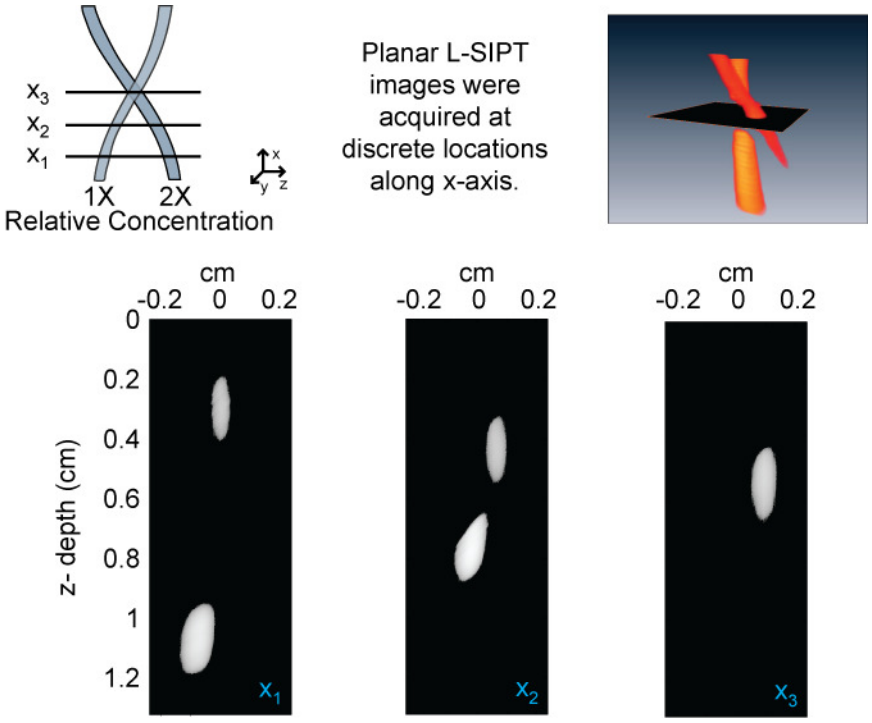

Figure 46: First 3D L-SIPT demonstration. We performed a proof of concept experiment using the 2D scan version of L-SIPT. Two polyethylene tubes were filled with a NIR fluorophore and serially translated along the x-axis through L-SIPT's planar scan field with a L-SIPT scan performed at each x plane. One tube was filled with twice the concentration of fluorophore as the other. 38 scans were acquired with a 0.127 mm x-step size were stitched together via post-processing using Amira and demonstrate L-SIPT's ability to image in 3D.

First demonstration of L-SIPT's single sweep 3D imaging principle

Collimated light incident on a cylindrical lens placed before an objective lens becomes a focused light sheet after the objective lens. The waist of the sheet is thinnest at the focal plane of the objective lens. Our raytrace model and 2D proof of concept experiments with a prototype L-SIPT system showed that this sheet of light could be scanned through the sample and detected by a stationary detector. To demonstrate single sweep 3D imaging without requiring sample translation we modified our prototype system by placing a cylindrical lens (f = 50 mm) in the path of the illumination beam before the polygon scanner. The cylindrical lens focuses light along a single axis (perpendicular to the cylinder axis) while leaving the other axis collimated (Figure 47A). The focused line created by the cylindrical lens was placed in the back focal plane

of the scan lens to create the sharpest line in the scan lens focal plane (Dwyer et al. 2006, Dwyer et al. 2007). To detect the sheet of fluorescence in a single sweep we further modified the prototype system by switching the linear array detector we had been using with the low-cost 2D CCD camera we had used to develop the SPLASSH system in Chapter 2. Using the SPLASSH control software we were able to acquire L-SIPT data while the polygon was rotated with a precision rotation stage.

The first sample we scanned was a homebuilt phantom laser cut from fluorescent plastic (Figure 47B). We placed the letters "L-SIPT" at two different heights to simulate objects at different depths. We imaged the phantom using a 30 mm focal length scan lens with the phantom in water to minimize index of refraction mismatch between the fluorescent plastic and air (to increase image quality, Figure 40C). As Figure 47D-G shows we were able to achieve a reasonable reconstruction of the phantom, accurately displaying the objects at different depths.

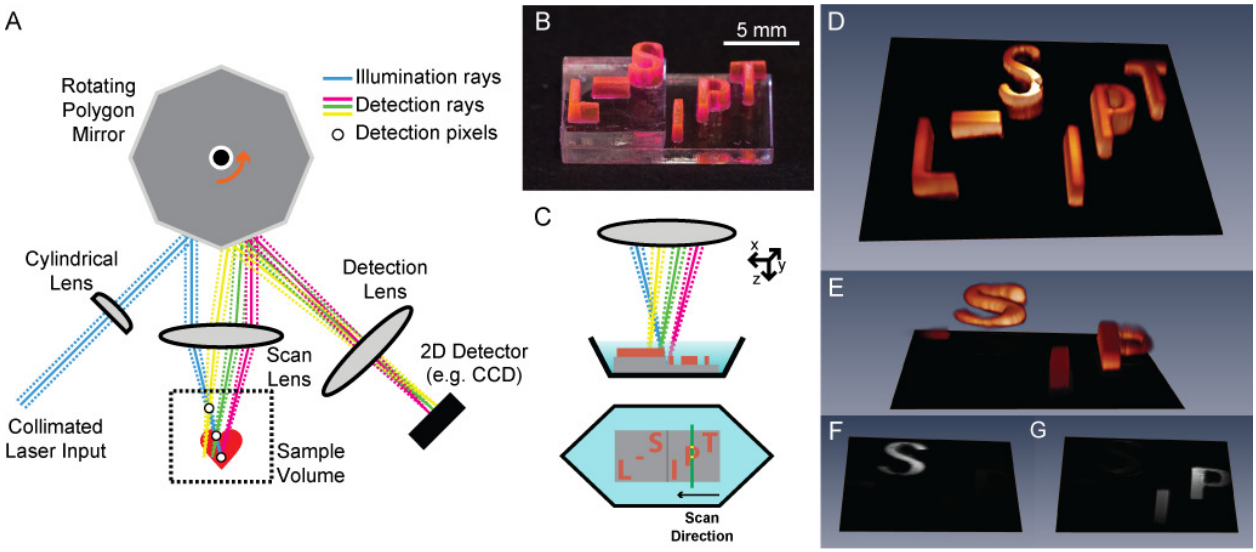

Figure 47: First demonstration of translationless 3D optical imaging using L-SIPT. A) System diagram incorporating a cylindrical lens to create a light sheet and 2D detector array to capture images of swept light-sheet. B) Photo of 3D phantom made from fluorescent plastic. C) L-SIPT imaging geometry. The sample remained stationary while L-SIPT's co-aligned illumination and detection planes were scanned across it. D) A single sweep resolved full 3D structure of phantom. E) Smaller volume of interest scan of center of phantom shows L-SIPT's ability to resolve objects at located different depths (the "-"and the "S" were at a shallower depth on the phantom while the "I" and the "P" were at a deeper depth). F). Individual θ-y image slices at a shallow, G) A θ-y image slice at a deeper depth.

Emboldened by L-SIPT's ability to image an object in 3D with a single sweep of its scanner, we sought a more challenging biological sample test the system on. We settled on *ex-vivo*, optically cleared transgenic adult *Drosophila* because they provided a strong fluorescent sample, were relatively easy to work with, and had complex 3D structure (Verveer et al. 2007). We first scanned a full adult body which had been cleared with wintergreen oil with a 30 mm scan lens (Figure 48A1-2) achieving a striking 3D image of the surface features of the sample. We next replaced the scan lens with a 20x water dipping objective lens with a high numerical aperture and scanned a surgically separated adult *Drosophila* head in glycerol to minimize refractive index mismatch between the sample and the immersion media (XLUMPlanFl 20x/0.95NA), shown in (Figure 48B1-2). With the high magnification lens we were able to acquire a 3D volumetric image of the eye of the Drosophila. These results demonstrated that L-SIPT was capable of imaging complex 3D biological structures with a single sweep of the polygon scanner without requiring sample translation. This result confirmed our design hypothesis that samples scanned with L-SIPT could be left free to move within the scanned volume.

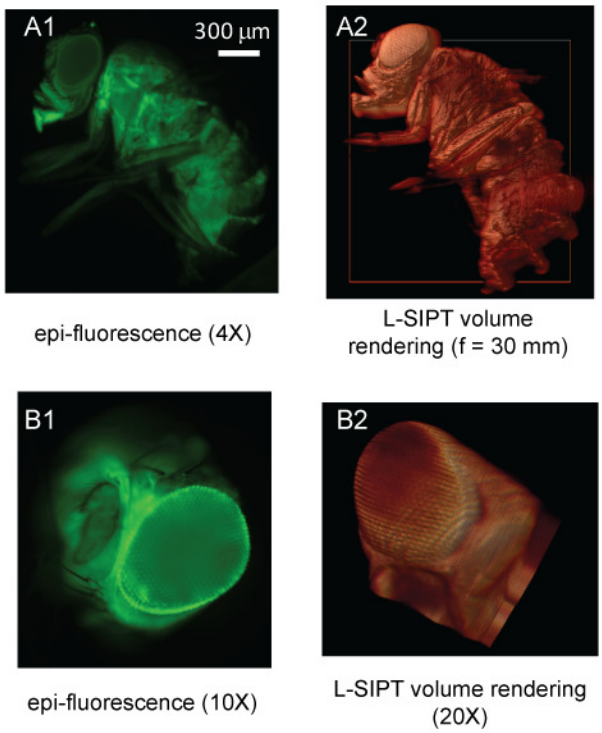

Figure 48: First biological sample imaged with L-SIPT. Full 3D volumetric images acquired from a single sweep of the polygon scanner. A1) 4x epifluorescence image of an optically cleared adult transgenic *Drosophila* A2) L-SIPT volume rendering reconstruction of same sample shows 3D measurement of surface features of sample (f = 30 mm scan lens). B1) 10x epifluorescence image of surgically separate *Drosophila* head. B2) L-SIPT volume rendering reconstruction of same sample using 20X scan lens shows 3D microscale features.

3.2.4 Improving resolution: off-axis detection of oblique illumination plane

The first L-SIPT prototypes (Section 3.2.3) established that L-SIPT is capable of acquiring full 3D images of biological samples without requiring sample translation relative to the imaging system with a single sweep of the scanner. This ability distinguishes the L-SIPT system from all other light-sheet volumetric imaging techniques to date. L-SIPT's *en-face*, single objective, non-contact imaging geometry allows for a significant increase in sample diversity over existing volumetric optical imaging technologies and holds the potential for allowing high-speed 3D imaging because light sheets can be rapidly scanned. While the images produced by the

prototype L-SIPT systems appeared very striking and did display the characteristics of optical sectioning (the ability to resolve objects in 3D), L-SIPT's depth axis resolution (comparable to axial resolution in typical microscopies) was very poor. This was due to the poor alignment of the illumination and detection sheets (Figure 43). In the initial L-SIPT prototypes, the detection sheet was aligned with the scan lens focal plane and not the illumination sheet. Proper alignment of the sheets would improve spatial resolution by minimizing the overlap between the illumination and detection point spread functions. The best resolution is achieved when the illumination and detection sheets are orthogonal to each other as in SPIM.

One method to align the two sheets would be to rotate the plane of the camera to align it with the oblique image formed by the detection lens (Figure 49). This method would suffer from spherical and comatic aberrations. Another method was developed by Dunsby 2008 as Oblique Planar Microscopy (OPM) using a pair of telescopes to rotate the image of an oblique illumination plan so that it images directly onto the plane of the camera (Dunsby 2008). In the OPM system illumination light is delivered to the objective similarly to L-SIPT; however the illumination light is not scanned. Off-axis detection is used to rotate the detection plane minimizing spherical and comatic aberrations and losses at the camera detection plane. To build 3D images, the OPM system acquires images of the sample as it is translated relative to the system. We hypothesized that the OPM detection geometry could be applied to L-SIPT because the detected light after being de-scanned by the polygon scanner is stationary in space. Additionally, the results of the raytrace simulations and initial prototype systems indicated that the detection plane overlaps the illumination plane throughout a sweep. The hand drawn raytrace in (Figure 39) shows OPM's off-axis detection scheme integrated into the L-SIPT system.

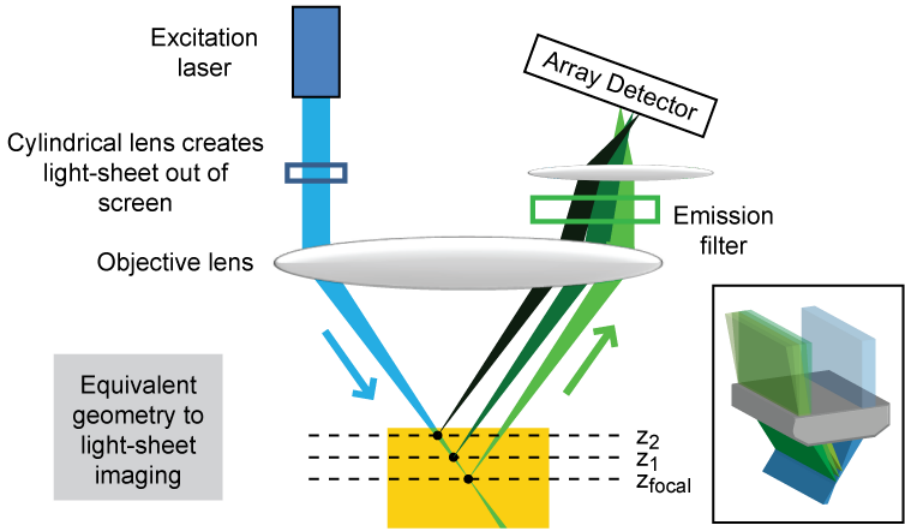

Figure 49: Rotation of camera plane could allow for improved L-SIPT spatial resolution. However this method suffers from spherical and comatic aberrations as well as losses at camera plane.

The illumination beam is incident on a single facet of the polygon scanner such that it reflects to be incident on the left half of a scan telescope. The scan telescope consists of two achromatic doublet lenses (Thorlabs) used to image the scanned beam onto the back aperture of a commercially available objective lens (XLUMPlanFL 20x/0.95W, Olympus). The lateral magnification of the telescope is chosen to image the scanned beam onto the edge of the back aperture of the objective lens to maximize the angle between the illumination and detection sheets. To create the illumination light sheet, a cylindrical lens is placed in the illumination path before the polygon scanner. The effective lens created by the combination of the cylindrical lens with the objective lens creates a light sheet similar to those created in SPIM-type imaging systems. In Figure 39 the plane of the light sheet lies out of the page and is centered along the solid blue line of the illumination beam path. In minimally to non-scattering samples, light originating from the illumination plane, indicated by open circles in Figure 39 travels along paths indicated by the shaded green paths. The detection light is reflected off the polygon facet adjacent to the illumination facet before entering the off-axis detection telescope. The detection

telescope is formed from two achromatic doublet lenses and a commercially available objective lens (doublets Thorlabs, UPlanSApo 20x/0.75NA, Olympus). The lenses comprising the detection telescope were chosen to match the lateral and axial magnifications of the detection path in the scan telescope so that the rotated image formed after the detection telescope maintains a 1:1 aspect ratio. A camera telescope then images the rotated plane onto the camera. The magnification of the camera telescope can be modified simply by changing the ratio of the camera telescope's lenses focal lengths. As shown by the detection beam paths in Figure 39, light from positions at different depths in the sample are focused onto different columns on the camera array, and so are acquired simultaneously. Furthermore, since the second polygon reflection serves to de-scan the remitted light, these adjacent positions on the detector will always correspond to points along the illumination plane. Light from different lateral positions (out of the page) on the light sheet are focused onto different rows on the camera array creating an image of an obliquely illuminated plane in the sample. The use of two facets of the same polygon scanner eliminates beam positioning errors due to scanner jitter which could occur using two decoupled scanners (Dwyer et al. 2007). We defined the coordinate axes of the raw L-SIPT data as the 'lateral', 'scan', and 'depth' axes (Figure 39, right). For all data shown from this system, a 488 nm laser was used for illumination and a 500 nm long pass emission filter was placed in front of the camera. Data acquired using this system is shown in Section 3.3.

Determining field rotation angle using commercial optical design software

The plane of fluorescence generated by the scanning illumination plane is descanned by the detection facet of the polygon mirror and imaged to a single, stationary plane after the rotation lens. Ideally, this rotated image plane is imaged onto the camera's detection plane. For the best

resolution the camera telescope should be oriented normally to the rotated image plane. The angle of the image plane can be modeled to a first approximation using the thin lens equation. Early versions of L-SIPT used image angles predicted using this model. However, the commercial microscopy lenses used by L-SIPT for its objective lens (XLUMPlanFL 20x/0.95NA W, Olympus) and rotation lenses (LCPlanFL 20x/0.40NA first generation system and UPlanSApo 20X/0.75NA second generation, Olympus) are complex, multi-element lenses with short focal lengths whose ray angles were difficult to model accurately with the thin-lens equation. To further refine L-SIPT's imaging performance a more realistic model was needed.

We built a model of L-SIPT using the OpTaliX (Optenso) commercially available optical design software package (Figure 50). OpTaliX can perform geometrical raytracing similar to that performed by our custom MATLAB raytracing codes. Additionally, OpTaliX is capable of calculating optical power distributions before and after lenses, apertures, and filters. This capability can be used to model L-SIPT's theoretical best PSF to determine L-SIPT's best resolution performance. Lens formulae were acquired from the lens manufacturers' websites in the case of Thorlabs lenses and patent literature in the case of Olympus lens. The scanning telescope was configured to meet the telecentric condition (Tsai et al. 2002) and the detection telescope was configured to provide a 1 : 1 lateral vs. axial magnification at the image plane formed by the rotation lens. Two models of L-SIPT were constructed: one for the illumination path and one for the detection path. The illumination path model was used to determine the angle of the oblique illumination plane in the sample volume. This plane was then used as input to the detection path model to determine the angle of the rotated image plane after the rotation lens. Collimated light rays 1 mm in diameter were launched towards the illumination facet of the polygon such that the reflected rays travelled parallel to the scanning telescope's optical axis.

The central ray of the illumination model was used as the input object to the detection path model. Rays were launched from discrete positions along the illumination central ray and allowed to travel through L-SIPT to model the oblique detection plane. These positions were located at different depths within the sample volume. The intersection points of the rays after the rotation lens were used to determine the rotated image plane. The angle of this plane relative to the optical axis of the rotation lens was then determined. Multiple scan angles of the polygon mirror were used and the average angle of the image plane after the rotation lens was used to position the camera telescope. The rotated image plane for the L-SIPT configuration described by Table 3 was found to be 34.5° relative to the optical axis of rotation lens.

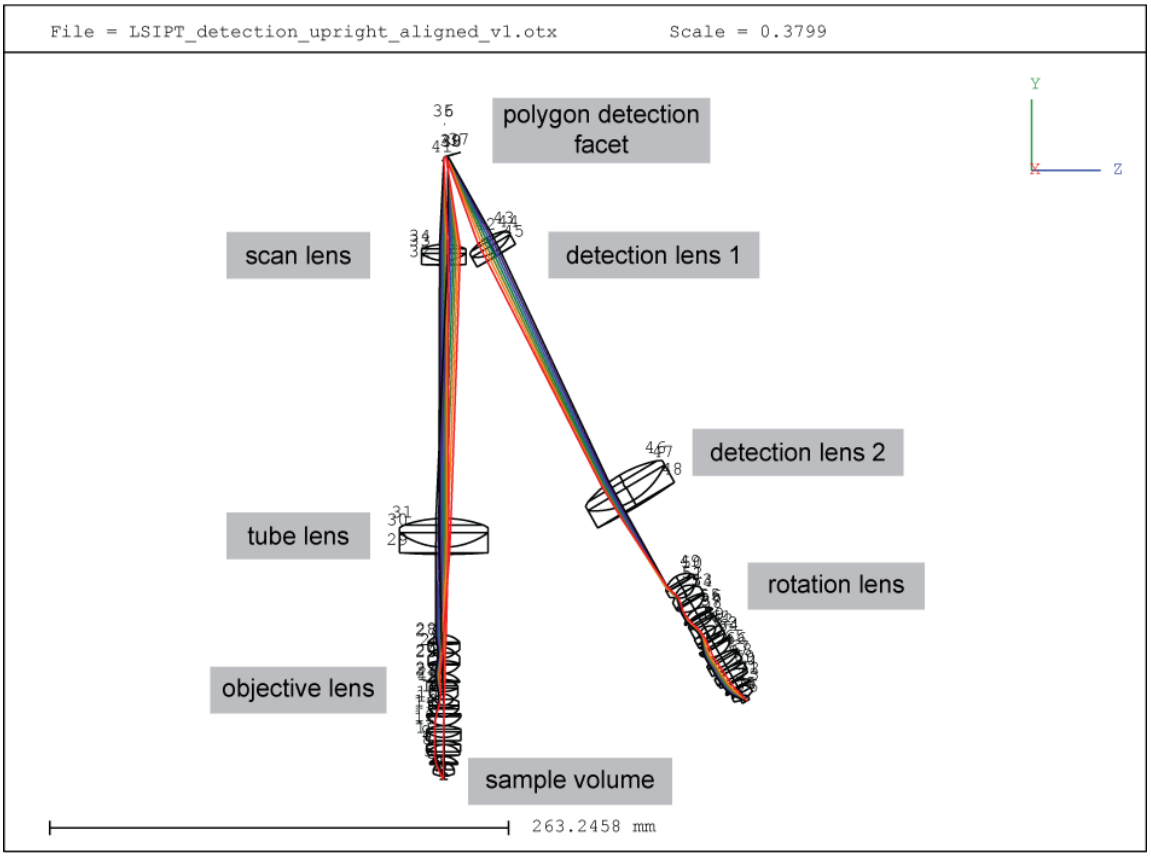

Figure 50: Modeling the L-SIPT detection optics using a commercially available optical design software package. We used OpTaliX (Optenso) to provide a full geometrical raytrace model of the L-SIPT system. Optical design values for our commercially available objective lens (XLUMPlanFl 20x/0.95NA W, Olympus) were found from the patent literature (Kasahara 2002). Here we show a screen grab of the software package modeling the paths of rays originating from the illumination plane and the image they form after the field rotation lens. Annotations added after screen grab was acquired.

Factors influencing L-SIPT's volumetric scan rate

The inherent volumetric scan rate speed increase provided by L-SIPT is due to its translation-free, *en-face* non-contact scanning geometry and its use of light-sheet imaging's significant parallelization of data acquisition. L-SIPT's volumetric scan rate (in Volumes per Second) is given by VPS = (camera frame rate / angles per volume) with the angles per volume determined by the desired scan axis resolution (roughly equivalent to y-axis resolution in traditional scanning microscopies). Figure 51 shows the range of volumetric scan rates achievable using a high-performance camera versus the low-cost firewire camera used in our prototype L-SIPT system.

To achieve the stated volumetric scan rates, the polygonal scanner must sweep at (60 x VPS/N_p) RPM where N_p is the number of polygon facets. For an 8-sided polygon, a VPS of 10 equates to a unidirectional polygon rotation rate of 75 RPM (most off-the-shelf polygon scanners are configured to rotate at > 1000 RPM). However, a limitation of this calculation is the duty cycle of each scan (the percentage of time during a single sweep of the polygon where imaging data is collected = $^{\text{usable scan angle}}$ / $_{\text{full polygon sweep angle}}$). In L-SIPT, this is typically less than 100%, particularly for polygons with a small number of facets and therefore a large sweep angle. This leads to redundancy or 'dead time' in the scan, and requires the camera frame rate to be increased to maintain the same scan axis resolution for a given VPS. To avoid this duty cycle problem in our current system, we used bi-directional scanning, whereby the polygon mirrors used in the prototype system were rotated back and forth by either an oscillating motor, a custom cam-follower scanner, or a high-speed single-axis galvanometric scanner. In this configuration only two facets are actually used. Oscillating the mirror at half of the rotational rate of the unidirectionally scanned polygon allows data to be acquired with a near perfect duty cycle. In

our case, this approach introduced direction-dependent effects due to motor acceleration that needed to be corrected using offline calibrations as described above. Our single-axis galvanometric scanner allows for near perfect duty cycles. MEMs-based scanners could also be used to achieve this performance characteristic. Since L-SIPT acquires a full 3D volume for each sweep of the scanning element, none of these choices would face problems due to speed limitations.

The above analysis demonstrates that the rate limiting element of L-SIPT is the camera used to acquire images of the obliquely swept plane. However, while high-speed cameras are available that, in principle, can acquire at up to 200,000 fps (Figure 51), the ultimate limit will be the signal-to-noise achievable in images sampled at the very low integration times required for such high frame rates. Performance will therefore be a trade-off between the camera's sensitivity and noise levels, the efficiency of the fluorophore in the sample, and the ability of the sample to withstand illumination intensities high enough to yield images of sufficient quality. The ultimate limit of L-SIPT volumetric scan rates is therefore sample dependent, and will be determined by the chosen application of the system. This sample dependent fundamental volumetric scan rate limit applies to all optical imaging systems, although L-SIPT shares the feature of all light-sheet imaging approaches in that it minimizes photodamage compared to confocal and wide-field fluorescence imaging. We therefore anticipate that using high performance, cooled cameras with larger pixel sizes will enable practical volumetric scan rates in the range of 60 or more VPS in typical biological samples.

Volumetric scan rates for NAC Image Technology Memrecam HX-3

oblique plane pixel resolution	# of scan angles per scan: 100	200	500
2560 x 1920 (2000 fps)	20	10	4
384 x 288 (75,000 fps)	750	375	150
384 x 96 (200,000 fps)	2,000	1,000	400

Volumetric scan rates for Andor Technology Zyla sCMOS

oblique plane pixel resolution	# of scan angles per scan: 100	200	500
2560 x 1920 (112 fps)	1.12	0.56	0.22
2560 x 288 (726 fps)	7.26	3.63	1.45
2560 x 96 (2041 fps)	20.41	10.20	4.08

Volumetric scan rates for Allied Vision Technologies Pike-F-032/B

oblique plane pixel resolution	# of scan angles per scan: 100	200	500
640 x 480 (104 fps)	1.04	0.52	0.21
640 x 288 (178 fps)	1.78	0.89	0.36
640 x 96 (532 fps)	5.32	2.66	1.06

Figure 51: L-SIPT volumetric scan rates are directly affected by choice of camera. L-SIPT's translationless imaging geometry provides a significant improvement in volumetric scan rates over traditional scanning microscopies (confocal and two photon) and newer light-sheet imaging technologies (Ultramicroscopy, SPIM, DSLM, and OCPI). L-SIPT's volumetric scan rate is determined by the framerate of the 2D camera used, and the desired angular resolution of the scanned volume (see Online Methods section for an in-depth discussion of experimental considerations limiting practical L-SIPT volumetric scan rates). Each raw image acquired by L-SIPT is of an obliquely illuminated plane of fluorescence. As this plane is swept through the sample a stack of oblique illumination planes is acquired and a 3D volume is sampled. Here we compare the volumetric scan rates possible with three different cameras; one high performance and high cost (NAC Image Technology Memrecam HX-3), one medium performance and medium cost (Andor Technology, Zyla sCMOS), and one low-cost (Allied Vision Technologies Pike F-032/B). We compare volumetric scan rate as a function of oblique plane pixel resolution and scan axis pixel resolution. For a comparable number of 'depth' slices the high performance camera provides over a factor of 421 times improvement in volumetric scan rates over the low-cost camera. The medium performance camera provides over a 4 times improvement over the low-cost camera. For comparison, a traditional, serial scanning microscopy acquiring pixels at 1 MHz would acquire a 384 x 288 x 200 pixel volume at 0.045 volumes per second (VPS) while the high performance camera can acquire the same resolved volume at 375 VPS.

3.2.5 Adding simultaneous multichannel detection

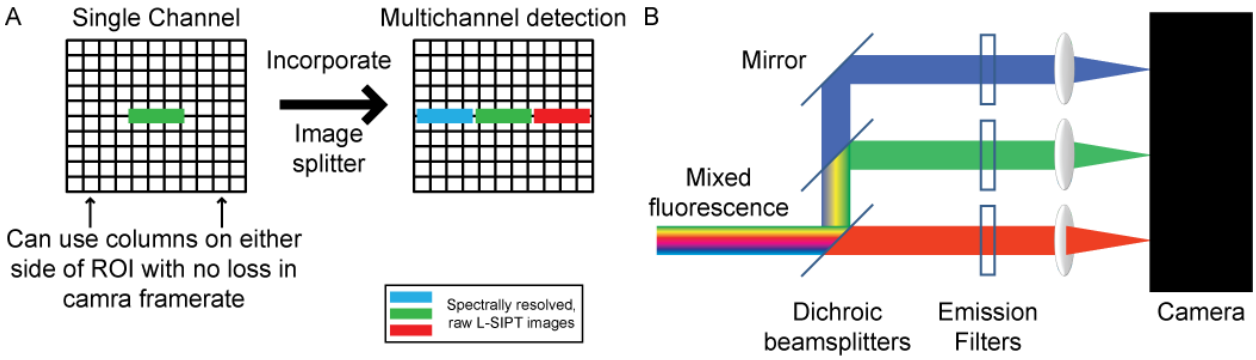

Figure 52: Simultaneous multichannel fluorescence detection for L-SIPT. A.) Reduced Regions of Interest (ROIs) are used to increase camera framerates when acquiring high-speed L-SIPT data. Camera framerates can be increased by reducing the number of rows in the image. There is no increase in framerate for reducing the number of columns. Current L-SIPT ROIs use ~1/3 of the available rows on our current high-speed camera, shown in green on left (Zyla sCMOS, Andor). An optical device known as an image splitter can be used to spatially separate mixed fluorescence light in equivalently sized images, shown in blue, green, and red on right. B.) Simplified optical layout for an image splitter. Mixed fluorescence enters from left. A series of dichroic beamsplitters and emission filters are used to spectrally separate the light. Focusing optics are then used to create images on the camera sensor.

Many different types of experiments are significantly improved when they can acquire data from multiple fluorophores simultaneously, making it possible to capture dynamic, single-trial *in-vivo* events such as measuring the neuromuscular system in freely crawling drosophila larvae. Neurons can be labeled with GCaMP6 intracellular calcium indicator and myosin in muscles can be labeled with Texas Red (data not shown). The most obvious solution to this problem is to buy two cameras and use the exposure signal of one to synchronize frame acquisition between them. However this is an expensive and complex solution because it requires two cameras and most likely two separate computers to implement successfully. Additionally, precise pixel-to-pixel alignment between the cameras is difficult to achieve.

Another option is shown in Figure 52B. Detected fluorescence light is split into individual wavelength channels using a series of dichroic mirrors and clean up emission filters. We can utilize this design because to acquire images at the framerates necessary for high-speed

L-SIPT we have been using reduced Regions of Interest (ROI). Camera framerates can be increased by reducing the number of rows in the image to be read. There is no increase in framerates for reducing the number of columns in the image. To fit the image of the illumination plane on the camera while maintaining a fast enough framerate for 3D image acquisition, we have chosen a camera telescope magnification to use a ROI approximately 800 x 80 pixels (columns x rows) in size for 7 μm square pixels. For the Andor Zyla camera in our current implementation of L-SIPT, this ROI only uses approximately 1/3 of the available columns on the sensor (Figure 52A). The simplistic image splitter design is shown in Figure 52B could be used to spectrally separate the mixed fluorescence ROI shown in Figure 52A (left) into three color channels shown in Figure 52A (right).

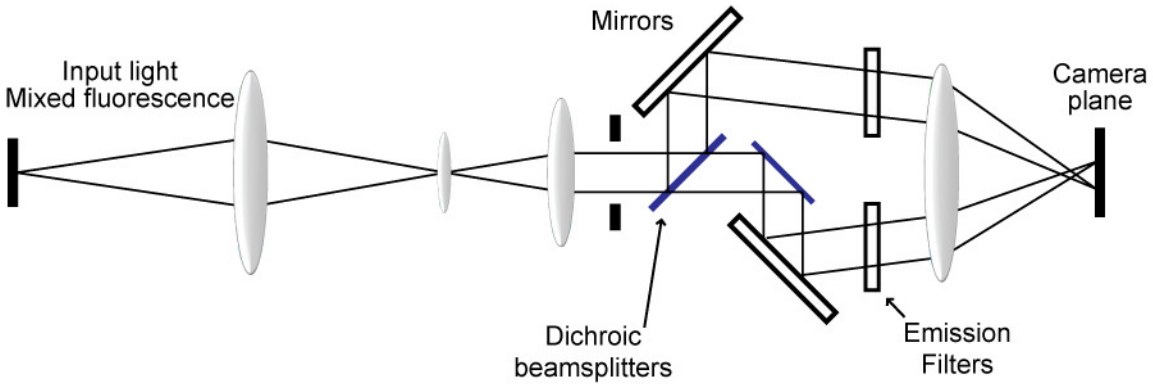

Figure 53: Commercial image splitter optical layout. From Photometrics DV2 (Photometrics 2013).

Commercially available image splitter designs for fluorescence microscopes exist (Figure 53) and can be directly incorporated into L-SIPT to take advantage of the extra columns we are currently not using on the camera (Figure 54) (Photometrics 2013). Individual lenses are used to focus the channels onto discrete regions of the camera sensor and allow for rough alignment between color channels. Sub-pixel alignment is achieved using post-processing of images. This

design has the advantage that all wavelength channels are acquired simultaneously meaning a single scan can be used to acquire multiple, co-registered color channels.

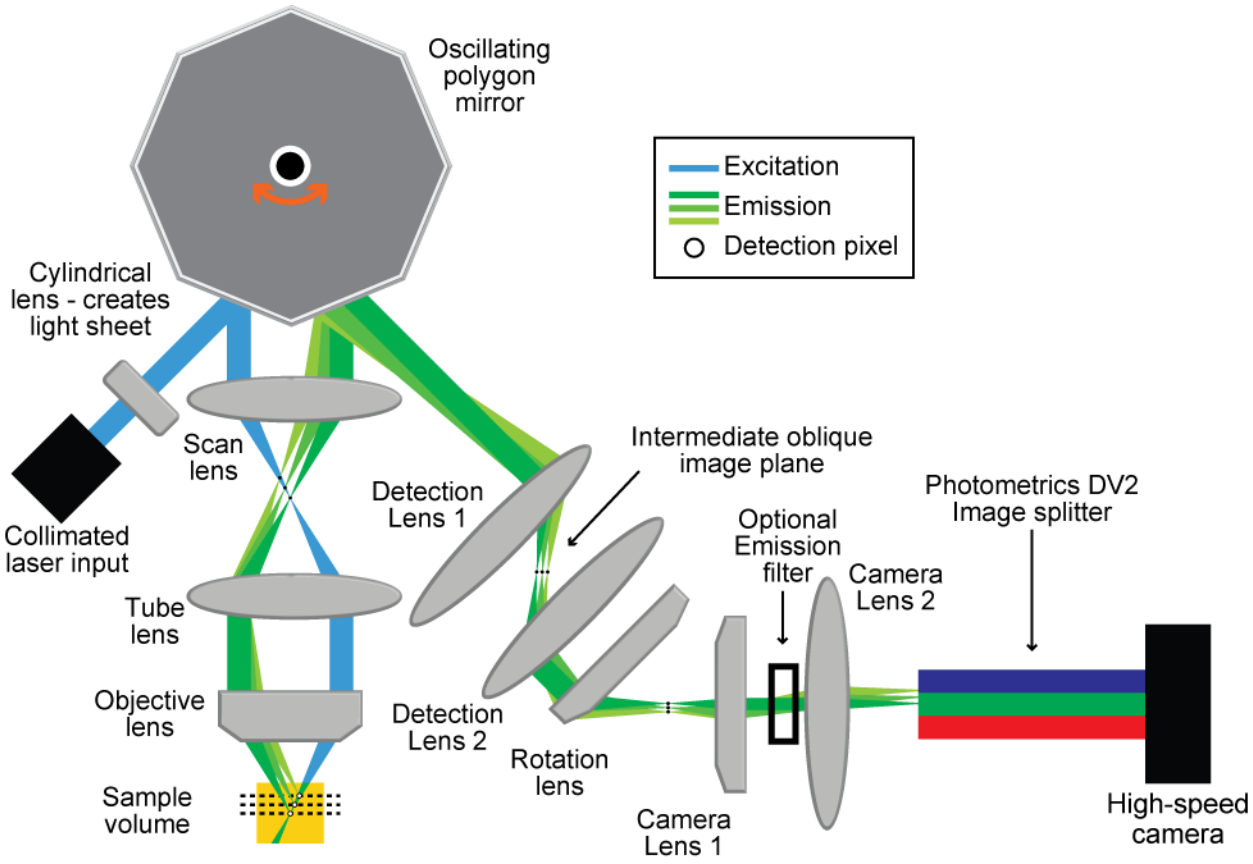

Figure 54: Addition of commercial image splitter to L-SIPT system. The Photometrics DV2 image splitter splits mixed fluorescence into two side-by-side spectrally separated fluorescence images. The DV2 can be inserted directly into the L-SIPT optical train as shown. The DV2 is currently implemented with two fluorescence channels 525 ± 22.5 nm and 600 ± 25 nm (emission filters: 86984 and 84785, Edmund Optics, beamsplitter: 565dcxr, Chroma), though it is relatively straightforward to change the spectral properties of the filter by incorporating different dichroic beamsplitters and emission filters.

We scanned a dual transgenically labeled *Drosophila* line (NompfCQF,QUAStdTom; ppk, UASCD8GFP) kindly provided by the laboratory of Dr. Wesley Grueber at Columbia University (Figure 55). This line expressed GFP in its class IV sensory neurons and tdTomato in its class III sensory neurons. These neurons are 2 members of the 4 member class of dendritic arborization sensory neurons (Grueber et al. 2003). Dendritic arborization neurons tile the exterior tissues of *Drosophila* larva and develop progressively larger dendritic fields and

complex branching patterns as their class level increases. Class III neurons are distinct however in that they show short terminal branches extending from their main dendritic trunks (Grueber et al. 2003). GFP and tdTomato are well spectrally separated in their emission channels when excited with our 488 nm laser (peak emissions approximately GFP: 500 – 525 nm tdTomato: 560 – 650 nm). The data shown in Figure 55C-D was acquired from a single scan of an *ex vivo* sample (sacrificed in ethanol for 5 minutes before imaging). A 1st instar larva was placed in a 4% agar in PBS chamber for scanning. Epifluorescence images acquired immediately prior to L-SIPT imaging are shown in Figure 55B. Two L-SIPT fluorescence channels were acquired simultaneously for GFP and tdTomato using bandpass fluorescence emission filters (525 ± 25 nm and 600 ± 25 nm, 86984 and 84785, Edmund Optics, respectively) and a dichroic beamsplitter installed in the DV2 (565dcxr, Chroma). Figure 55C shows two L-SIPT depth slices approximately 9 microns apart. Different sets of neurons and their projections are clearly visible. At right are the two color RGB merge of the two channels allows for direct visual comparison of the different neuronal classes' morphologies. Two different views of a 3D dual-channel RGB merge volume rendering of the dataset are shown in Figure 55D showing the 3D structure of the neurons.

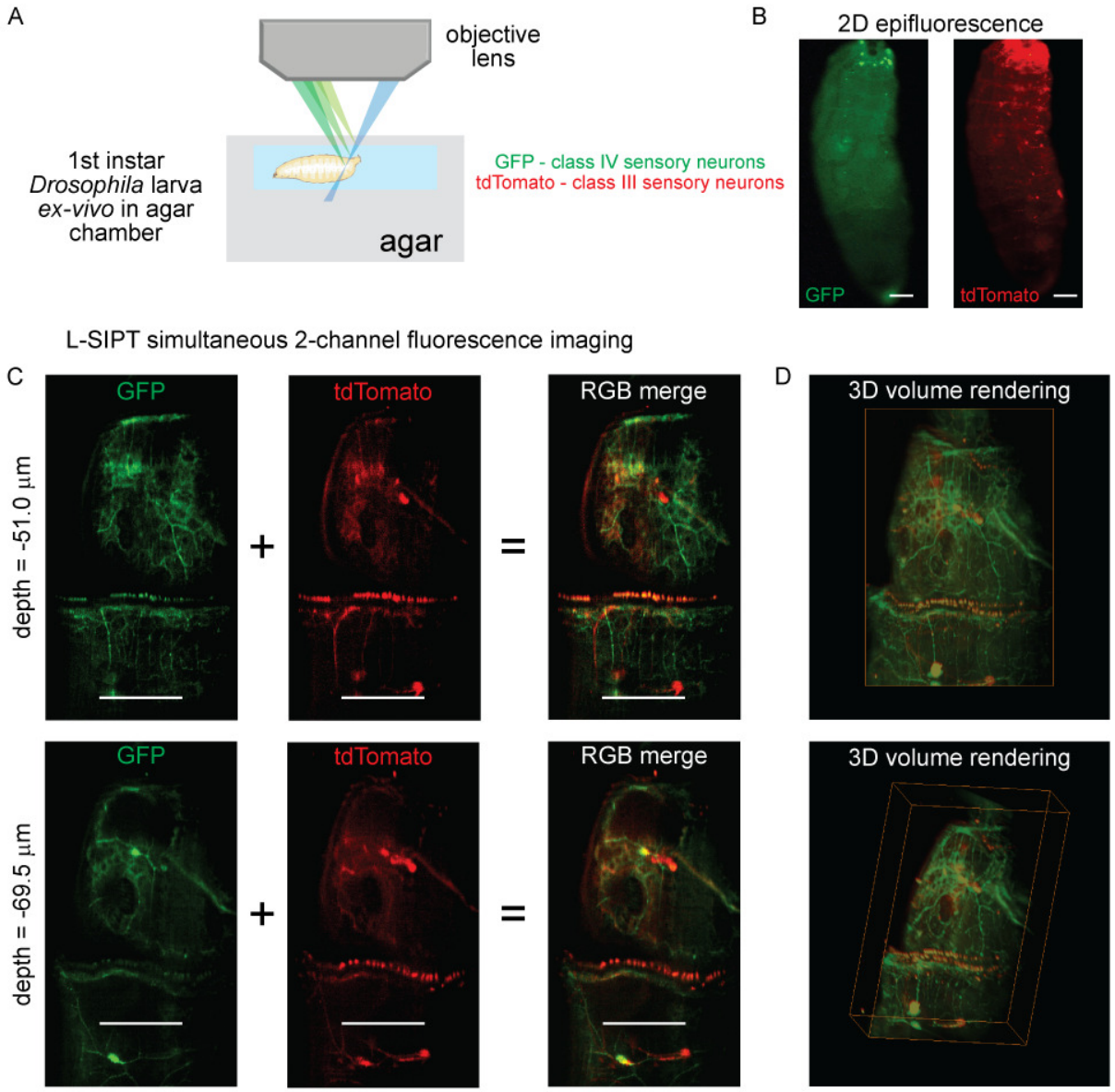

Figure 55: Simultaneous dual-color L-SIPT imaging of transgenic Drosophila larva ex vivo. A.) A 1st instar larva was sacrificed in ethanol for 5 minutes prior to imaging. L-SIPT imaging was performed while larva was in an 4 % agar in PBS chamber and saline solution. Class IV and class III dendritic arborization neurons were labeled with GFP and tdTomato, respectively. B.) Epifluorescence images of the larva prior to L-SIPT imaging. C.) L-SIPT depth slices from two distinct depths of the larva show distinct patterns of fluorescence expression clearly showing the distinct neuron types. Dual-channel RGB merges allow for direct visual inspection of the differing morphologies of the neuron classes. D.) 3D, dual-channel RGB volume rendering of the same data allows for direct visual inspection of the 3D morphology of the larva. All scale bars 200 µm. Larva cartoon in A.) adapted from (Staveley).

3.3 Developing applications of high-speed, volumetric imaging

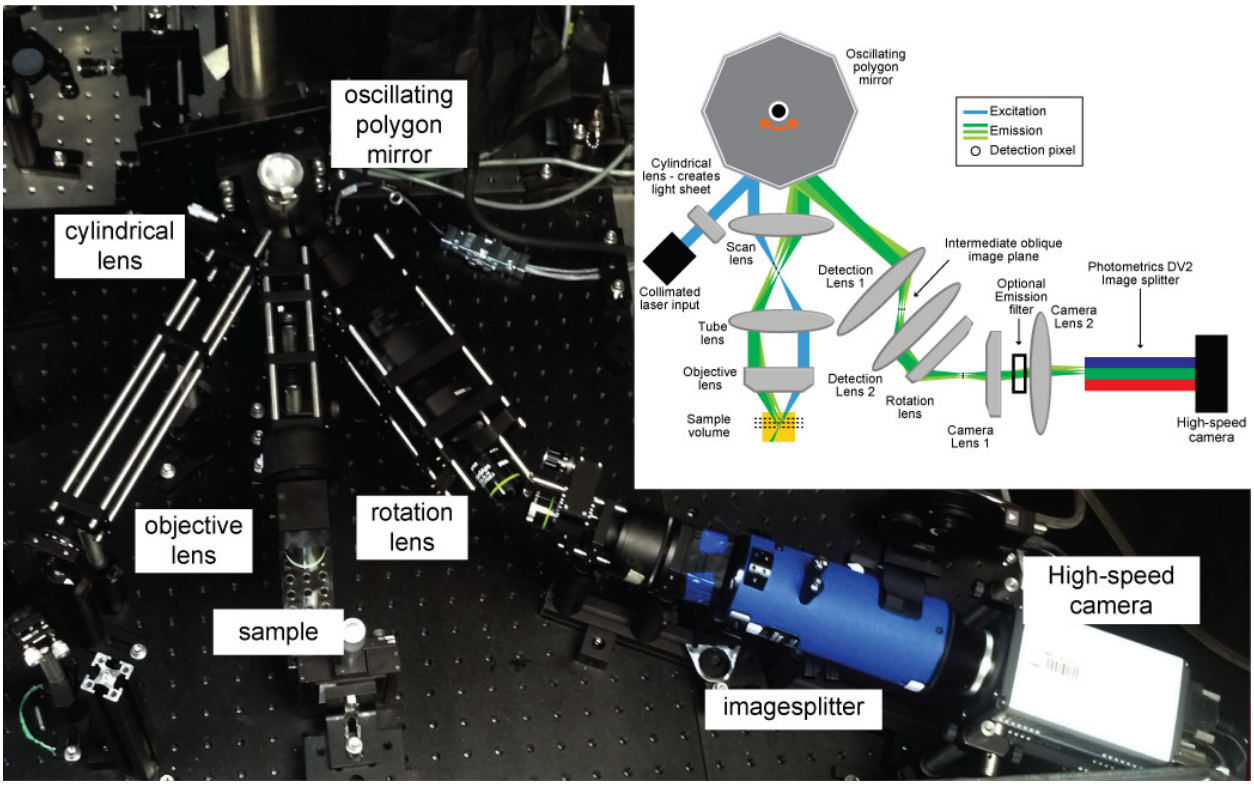

Figure 56: Complete L-SIPT system. The current L-SIPT system utilizes a 12-sided polygon mirror mounted on a single axis galvanometric scanner (6240H, Cambridge Technology), a high-speed sCMOS camera (Zyla, Andor), a two channel image splitter (DV2, Photometrics), and a series of lenses from Thorlabs and Olympus.

L-SIPT offers the unique ability to acquire volumetric data at volumetric scan rates >20 VPS. L-SIPT achieves this ability by rapidly scanning co-aligned illumination and detection planes through the sample using a single-lens, *en-face* imaging geometry. The sample is not translated relative to the imaging system to acquire volumetric data, meaning the sample can be allowed to exist in its native environment. In the case of cortical imaging in rodents the animal (Section 3.3.4) is allowed to remain in its surgical restraint. In the case of freely moving samples such as crawling *Drosophila* larvae, L-SIPT is uniquely able to track larval motion as it executes normal locomotion. Previous studies using existing volumetric imaging techniques (light sheet

illumination) are forced to create fictitious environments for their moving samples (Ahrens et al. 2013). In this Section we provide results from imaging experiments where we explored the use of L-SIPT's translationless imaging geometry to image fixed, *ex-vivo* samples (Section 3.3.1), freely moving samples *in-vivo* (Section 3.3.2), high-speed intracellular calcium activity in acute murine brain slices (Section 3.3.3), and *in-vivo* cortical brain imaging in mice and rats (Section 3.3.4).

The data shown in this Section were acquired with two different versions of the L-SIPT system shown in Figure 56. Early versions of the system used an 8-sided polygon mirror (SOS-BB10, Lincoln Laser) driven by a precision rotation stage (PRM1Z8, Thorlabs). A low-cost high-speed camera was used to acquire images (Pike F-032B, AVT). This system was limited to volumetric scans rates of ~2 Hz, except for the data shown in Section 3.3.3 which used a home-built motor driven cam scanner to achieve volumetric scan rates of ~7 Hz. This scanner was subject to significant image degrading mechanical vibrations. The configuration of the major elements of this system is listed in Table 2. The second version of L-SPIT used a 12-sided polygon (2-2-3340-160-00, Lincoln Laser) custom mounted to a single-axis, high-speed galvanometric scanner (6240H, Cambridge Technology). A sCMOS camera was used to acquire images (Zyla, Andor). The galvanometric scanner provides scan rates exceeding 100 scans per second. At suitable resolutions this system is capable of acquiring data at volumetric scan rates > 20 VPS. The configuration of the major elements of this system is listed in Table 3.

We chose a single-axis galvanometric scanner to provide both complete control over the size and shape of the scanned volume as well as high scan rates (>40 VPS) with near perfect duty cycles. To integrate a single-axis galvanometer into L-SIPT a multi-faceted mirror was custom mounted to the galvanometer drive shaft. Two design considerations were taken into account

when optimizing the size and shape of the multi-faceted mirror for L-SIPT: A.) beam walk was minimized at the back aperture of the infinity-corrected objective lens and B.) lateral magnification of the scanned beam was matched for maximum use of the objective lens' numerical aperture to optimize the system's spatial resolution (Tsai et al. 2002). To achieve optimal imaging performance in any laser scanning system using infinity corrected objectives, the "imaging condition" must be met. The imaging condition maintains constant illumination power at the back aperture of the objective by minimizing beam walking at the back aperture of the objective (Tsai et al. 2002). This is important to maintain consistent illumination power throughout the scanned volume. Under the imaging condition, the scanning telescope relays an image of scanned beam on the scanner to the back aperture of the objective lens. The second design consideration optimizes the spatial resolution by ensuring the maximum angle between the illumination light sheets and detection plane. To achieve this, the illumination beam must be imaged onto the edge of the back aperture of the objective lens. The lateral and axial magnifications of the scanning telescope, set by the ratio of the telescope's two lenses and the distance between the scanner and the first telescope lens, affect the scanned beam quality.

3.3.1 Imaging fixed samples *ex-vivo*

We built a prototype system according to the system layout in Figure 39 and then reimaged the optically cleared *ex-vivo* adult *Drosophila* samples to provide a comparison between the original L-SIPT system performance and the new "full" L-SIPT system design. Figure 57A shows an epifluorescence image (4x, FITC cube) of an uncleared OK371-gal4;UAS-CD8:GFP transgenic adult *Drosophila* alongside a 3D volume rendering of raw L-SIPT data of the same sample (acquired using a f = 30 mm achromatic doublet as the objective lens) (Mahr and Aberle 2006).

Figure 57B shows an epifluorescence image (4x, FITC cube) and L-SIPT volume rendering of the head of a 477-gal4;UAS-CD8:GFP transgenic *Drosophila*, that was optically cleared using a protocol similar to Dodt et al. and acquired using a 20x objective lens (Grueber et al. 2003, Dodt et al. 2007). Figure 57C shows select 'depth' slices from raw L-SIPT data demonstrating its optical sectioning capabilities. Similar penetration and sectioning was seen when the same sample was imaged using two-photon microscopy (Figure 58). In all of these samples, signal detected by L-SIPT is a combination of GFP and autofluorescence.

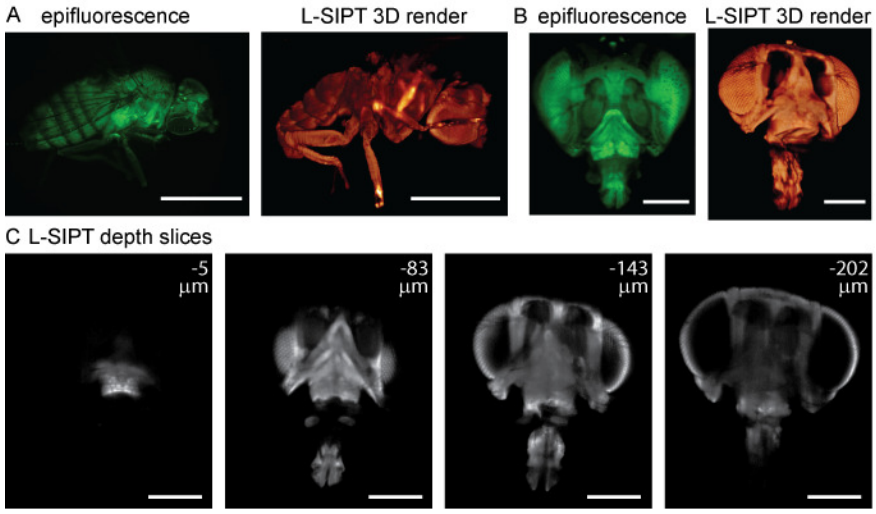

Figure 57: Ex-vivo L-SIPT 3D volumetric imaging of adult Drosophila. A.) Epifluorescence image (4x, FITC cube) of adult OK371-gal4;UAS-CD8:GFP (left) and L-SIPT 3D volume render of raw data (right). B.) Epifluorescence image (4x, FITC cube) of isolated, optically cleared adult 477-gal4; UAS-CD8:GFP head (left) and L-SIPT volume render (right). C.) A series of raw L-SIPT 'depth' slices from image volume rendered in B.), depths estimated from 2 photon data (data not shown). Scale bars: A.) 1 mm, B and C.) 200 µm.

To provide comparison images, two-photon stacks of the optically cleared 477-gal4; UAS-CD8:GFP strain and the mhc-gal4;UAS-CD8:GFP larva were acquired using our home-built two-photon microscopy system and visualized using custom MATLAB code (Schuster et al. 1996, Grueber et al. 2003, Radosevich et al. 2008). Signal from three emission channels were acquired using three separate photomultipler tube (PMT) detectors (350 – 505 nm (blue), 505 – 560 nm (green), and 560 – 700 nm (red)). RGB image stacks were acquired with an excitation

wavelength of 800 nm using a Mai-Tai HP Deep-See Ti:Sapphire laser (Spectra-Physics). RGB color images were created by using the MATLAB functions stretchlim and imadjust to threshold and optimize image contrast for each color channel before they were combined into an RGB image.

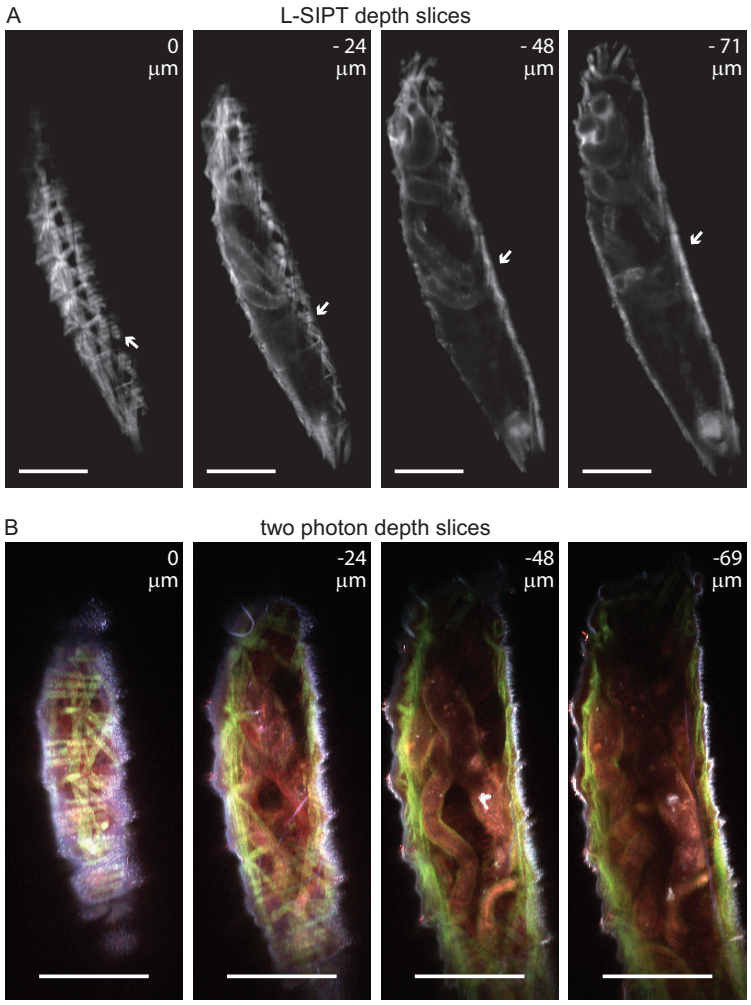

Figure 58: Comparison of high-resolution L-SIPT scans to a two-photon microscopy images of a Drosophila larva. All data was acquired ex-vivo from the same 1st instar mhc-gal4;UAS-CD8:GFP *Drosophila* larva after the dynamic in-vivo data shown in Figure 61 was acquired. This larva expressed GFP fluorescence in its muscles, and exhibited autofluorescence in its gut (Schuster et al. 1996). A.) L-SIPT 'depth' slices demonstrate that both the exterior muscle structure (arrows) and interior autofluorescence from the animal's digestive tract can be visualized in the intact animal. B.) 3 color two photon 'depth' slices show the same exterior and interior structures visualized with L-SIPT, with the exterior muscle structure signal originating from GFP expressed in larval muscles under the control of the myosin heavy chain promoter and autofluorescence from the interior digestive tract structures. The external waxy cuticle is visualized by the blue second harmonic generation signal. Scale bars 200 µm.

Experiment protocol

The uncleared transgenic adult *Drosophila* (genotype: OK371-gal4;UAS-CD8:GFP) shown in Figure 57A was placed in a freezer for 5 minutes and then euthanized in 100% ethanol for 5 minutes. The samples were imaged in glycerol through a glass coverslip in an inverted geometry using an f = 30mm achromatic doublet objective lens (Thorlabs, AC254-030-A1). 3D images with 640 x 480 x 1500 voxels (lateral, depth, scan axes, respectively) were acquired at a 0.04 °/s scan rate for a 2.4° scan, and a 40 ms exposure time. Images were cropped for the optimized zone and sample size in post-processing. This transgenic strain labeled glutamatergic neurons with GFP, although most of the signal visualized with L-SIPT was due to autofluorescence from the body of the fly.

The optically cleared transgenic adult *Drosophila* head samples shown in Figure 57B-C (genotype: 477-gal4;UAS-CD8:GFP) were prepared following a protocol similar to that described in Dodt et al. (Grueber et al. 2003, Dodt et al. 2007). Specifically, flies were anesthetized for 5 minutes in a freezer, euthanized in 100% ethanol, washed in 4% paraformaldehyde for 20 minutes three times, washed in phosphate buffered solution (PBS) for 10 minutes two times, and then dehydrated in a graded ethanol series for 2 hours at each concentration with the samples left to sit in the final concentration overnight (50%, 70%, 80%, 96%, and 100% two times). The samples were then placed in wintergreen oil (Fisher Scientific, O3695-500) for 2 days to complete the clearing process. In some cases, heads were then surgically removed from the body for ease of imaging from anterior and posterior views. Imaging was performed in an inverted geometry with the samples in mineral oil baths through a glass coverslip. 3D images with 640 x 480 x 1500 voxels (lateral, depth, scan axes, respectively) were acquired at a 0.04 °/s scan rate for a 2.4° scan, and a 40 ms exposure time. Images were

cropped for the optimized zone and sample size in post-processing. Mineral oil was chosen to minimize refractive index mismatches between the sample and the illumination sheet. The 477-gal4; UAS-CD8:GFP strain labels sensory neurons and central brain neurons with GFP, however most of the signal visualized with L-SIPT was due to autofluorescence resulting from the fixing procedure used to optically clear the sample.

Live 1st instar larvae as shown in Figure 58 (genotype: mhc-gal4;UAS-CD8:GFP) were imaged *in-vivo* to demonstrate L-SIPT's ability to image live, freely moving samples (Schuster et al. 1996). Larvae were selected by visual inspection, washed in saline to remove surface debris, and placed in a drop of saline on top of a glass slide. Saline was chosen to minimize refractive index mismatches between the sample and the illumination sheet while keeping the sample alive. ~1mm thick spacers were used to loosely support a glass coverslip over the sample such that the upright Olympus, XLUMPlanFL 20x/0.95W objective could be immersed in a drop of water on top of the coverslip without disturbing the sample. For each 3D 'movie' 132 images were acquired at 1.72 volumes per second (VPS) using a bi-directional sweep scan with a resolution of 320 x 80 x 132 pixels and a CCD exposure time of 2.8 ms. The bi-directional sweep produced distorted images due to the non-linear trajectory of our motor at high scan rates. To correct for this distortion we imaged a triangular registration target. When imaged with L-SIPT, the edges of this triangle appear curved, with the shape of the curve dependent on the speed of the motor and the direction of the sweep. A pair of distortion calibration curves was generated for the two sweep directions by measuring the location of the edges of the triangle averaged over 100 scans using the same acquisition parameters used to image the larvae in-vivo. 2D image interpolation was then used to correct the image distortion before images were rendered.

Once in-vivo imaging of the larvae was completed, they were euthanized in 100% ethanol for 10 minutes and then imaged post-mortem in saline. 3D images with 640 x 480 x 1500 pixels (lateral, depth, scan axes, respectively) were acquired at a 0.04 °/s scan rate for a 2.4° scan, and a 40 ms exposure time. Images were cropped to their optimized zone and sample size in post-processing.

Quantitative evaluation of L-SIPT spatial resolution

To quantitatively evaluate this system's spatial resolution we imaged a phantom composed of 1 micron diameter fluorescent beads in a low concentration agar gel (Figure 59). The 3D bead phantom was made by suspending 1 micron diameter fluorescent polystyrene beads (Invitrogen, F-8852) in 1.5% by weight agarose gel (Acros Organics, 400420250). The phantom was imaged using a water dipping objective (Olympus, XLUMPlanFL 20x/0.95W). The bead diameter was selected to provide sub-resolution point sources of light to sample L-SIPT's point spread function (PSF). As with other light sheet imaging techniques, the thinnest part of the incident light sheet provides the best resolution. For L-SIPT's geometry, this optimized zone corresponds to a range of depths, with resolution degrading above and below. Using an Olympus XLUMPlanFL 20x/0.95W objective, our optimized zone for this system spanned a depth of approximately 315 microns, within which our 'lateral', 'scan' and 'depth' axis point spread functions are 4.84 ± 1.30, 4.10 ± 1.10 and 12.06 ± 3.42 microns, respectively. LSIPT's non-linear scan pattern results in scaling of between 2.6 and 3.2 microns per pixel along its 'depth' axis within this zone. PSFs were determined along each of L-SIPT's 3 raw data axes (lateral, depth, and scan axes, respectively). Individual beads were located by eye, and then fitted to a Gaussian along each of the raw L-SIPT axis dimensions to determine respective PSFs (using

MATLAB). PSF resolution values reported here are the full width at half maximum (FWHM) of the Gaussian fit. The profiles from 29 beads were averaged before Gaussian fitting to determine the PSF values. To determine the pixel size along the lateral and depth axes, a fluorescent object was imaged while being translated step-wise through a fixed distance, yielding a pixel-to-distance scaling factor. To determine the pixel size along the scan axis, an L-SIPT scan of a planar target of a known size was acquired and compared to a spatially calibrated epi-fluorescence image of the same sample.

These values were measured with the first prototype L-SIPT system which incorporated off-axis detection optics. The specific lens configuration for this system is shown in Table 2. Figure 39 shows the labels applied to each lens in L-SIPT. This system was not corrected for coma, spherical aberrations, or field curvature. Additionally, the mismatch between the NA's of the objective lens and the field rotation lens resulted in a loss of light (and therefore SNR and a reduced focusing power) at the field rotated plane. In a later version of the L-SIPT prototype (Table 3) we more closely matched the NA's of these lenses and found an improvement in the scan axis resolution but not the depth axis resolution. This result could be due to poor angular alignment of the camera telescope to the rotated field plane. In Section 3.2.4 we utilized commercial optical design software (OpTalix, Optenso) to model the full L-SIPT prototype. Using this model we determined the optimal angle between the camera telescope and the field rotation lens' optical axis to be 34.5° for the L-SIPT configuration given in Table 3. After implementing the prototype using this angle we noticed an improvement in contrast in the raw L-SIPT images over previous implementations of the system with arbitrary angles.

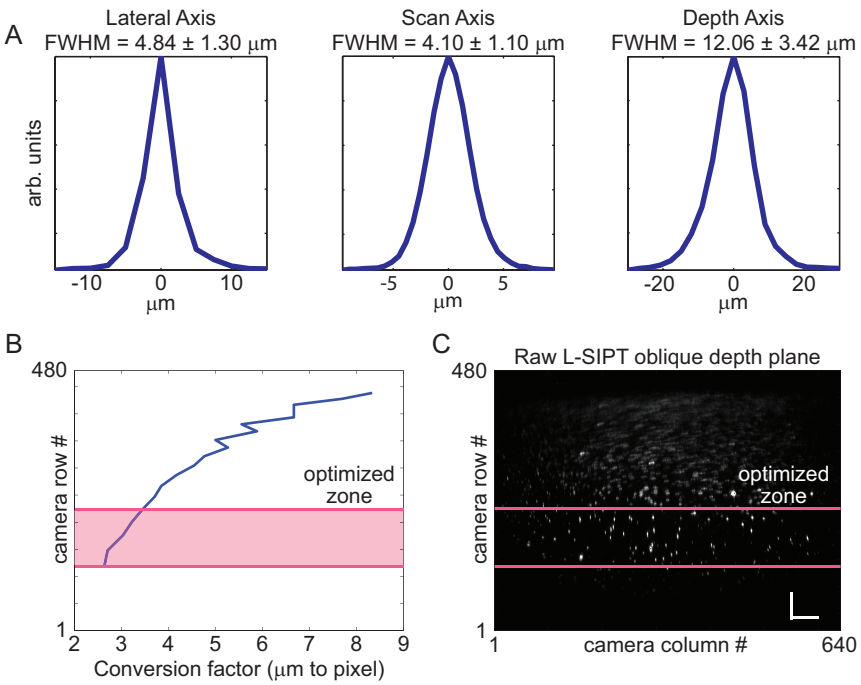

Figure 59: Quantitative evaluation of full L-SIPT's spatial resolution. A.) Point spread function (PSF) measurements along L-SIPT's coordinate axes acquired from 1 μm diameter polystyrene beads suspended in a 1.5% agarose gel. B.) System magnification varies along the depth axis. To quantify this we translated an object step-wise through a fixed distance and calculated the pixel-to-distance scaling factor as a function of depth. The 'optimized zone' for imaging (~315 μm for our 20x objective, indicated by pink shading) has the smallest conversion factor (2.6 - 3.2 μm per pixel). For dynamic scans only pixels within the optimized zone were read from the camera to yield the fastest possible volumetric scan rates. C.) Example raw L-SIPT oblique depth plane of 1 micron fluorescent microspheres suspended in an agarose phantom showing the varying magnification and imaging resolution of our prototype L-SIPT system. Scale bars 125 micron along lateral axis, 148.5 micron along depth axis. Pink lines illustrate the same optimized zone as indicated in B.).

polygon mirror	8 sided, 1.818” inscribed circle (SOS-BB10, Lincoln Laser)
camera	Pike F-032B (640 x 480, 104 fps) (AVT)
cylindrical lens	f = 50 mm (LJ1695RM-A)
scan lens	f = 100 mm (AC508-100-A1)
tube lens	f = 75 mm (AC508-075-A1)
objective lens	XLUMPlanFL 20X/0.95NA (Olympus)
detection lens 1	f = 100 mm (AC508-100-A1)
detection lens 2	f = 75 mm (AC508-075-A1)
rotation lens	LCPlanFL 20x/0.40NA (Olympus)
camera lens 1	UPlanFL N 10x/0.30NA Ph1 (Olympus)
camera lens 2	f = 75 mm (AC508-075-A1)

Table 2: Configuration of major optical elements in first L-SIPT prototype using off-axis detection. All lenses from Thorlabs unless stated otherwise.

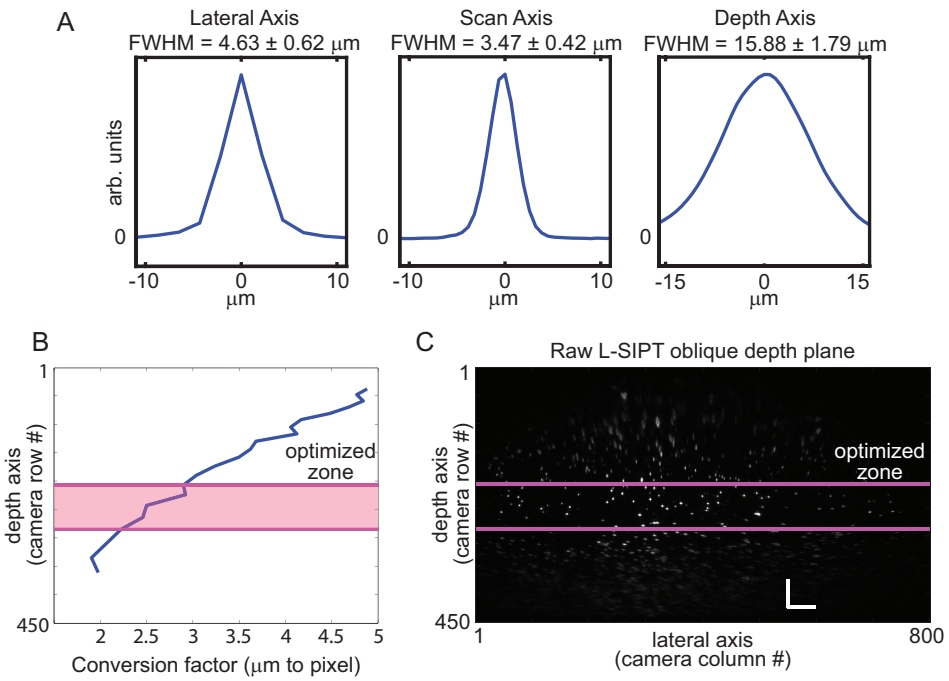

Figure 60 Quantitative evaluation of full L-SIPT's spatial resolution with improved detection optics. We improved L-SIPT's spatial resolution by using a commercially available objective lens to rotate the detection plane (UPlanSApo 20X/0.75NA, Olympus). The results shown here can be directly compared to those shown in Figure 59. A.) Point spread function (PSF) measurements along L-SIPT's coordinate axes acquired from 1 μm diameter polystyrene beads suspended in a 1.5% agarose gel. B.) System magnification varies along the depth axis. To quantify this we translated an object step-wise through a fixed distance and calculated the pixel-to-distance scaling factor as a function of depth. The 'optimized zone' for imaging (~260 μm for our 20x objective, indicated by pink shading) has the smallest conversion factor (2.2 – 2.9 μm per pixel). For dynamic scans only pixels within the optimized zone were read from the camera to yield the fastest possible volumetric scan rates. C.) Example raw L-SIPT oblique depth plane of 1 micron fluorescent microspheres suspended in an agarose phantom showing the varying magnification and imaging resolution of our prototype L-SIPT system. Scale bars 108.5 micron along lateral axis, 130 micron along depth axis. Pink lines illustrate the same optimized zone as indicated in B.).

polygon mirror	12 sided, 1.35" inscribed circle (2-2-3340-160-00, Lincoln Laser)
camera	Zyla (2560 x 2160, 100 fps) (Andor)
cylindrical lens	f = 50 mm (LJ1695RM-A)
scan lens	f = 50 mm (AC254-050-A1)
tube lens	f = 100 mm (AC508-100-A1)
objective lens	XLUMPlanFL 20X/0.95NA
detection lens 1	f = 50 mm (AC254-050-A1)
detection lens 2	f = 100 mm (AC508-100-A1)
rotation lens	UPlanSApo 20X/0.75NA (Olympus)
camera lens 1	UPlanFL N 10x/0.30NA Ph1 or LCPlanFL 20x/0.40NA (Olympus)
camera lens 2	f = 75 mm (AC508-075-A1)

Table 3: Configuration of major optical elements in second L-SIPT prototype using off-axis detection. All lenses from Thorlabs unless stated otherwise.

3.3.2 Imaging freely moving samples in-vivo

After improving L-SIPT's spatial resolution we tested the "full" L-SIPT system's ability to imaging freely moving objects in 3D. The polygon scanner we were using was driven by a precision rotation stage (PRM1Z8, Thorlabs) which allowed for a maximum 1.7 Volumes per Second scan rate over a volume approximately 1600 x 896 x 475 μm^3 in size. Based on our work with the adult *Drosophila* we noticed that 1st instar *Drosophila* larvae are small, relatively slow moving, relatively transparent, and the transgenic lines we were using were strongly fluorescent. We selected the mhc-gal4;UAS-CD8:GFP line because it strongly expressed GFP in its external muscles under the control of the myosin heavy chain promoter (Schuster et al. 1996). Figure 61A shows a 4x epifluorescence image (FITC cube) of the larva. Figure 61B shows a volume rendering from a high-resolution L-SIPT scan, while Figure 61C shows selected 'depth' slices from the same L-SIPT scan. Signal from GFP from the animals exterior muscle structure

(arrows) as well autofluorescence from the animal's interior digestive track can be visualized in the intact animal. Dynamic L-SIPT data was acquired on this sample while it was allowed to move freely on a microscope slide in saline at room temperature. Dynamic volumetric scans were acquired at 1.72 volumes per second (VPS) over 58 seconds using an Olympus XLUMPlanFL 20x/0.95W objective in an upright configuration. Figure 61D shows two depth planes from five consecutive L-SIPT volume scans across a 2.3 second window. The larva can be seen to be moving dynamically while both its external surface and internal organs are captured in 3D *in-vivo*. Note that this data was acquired using an inexpensive low-end camera, limiting the achievable volumetric scan rate.

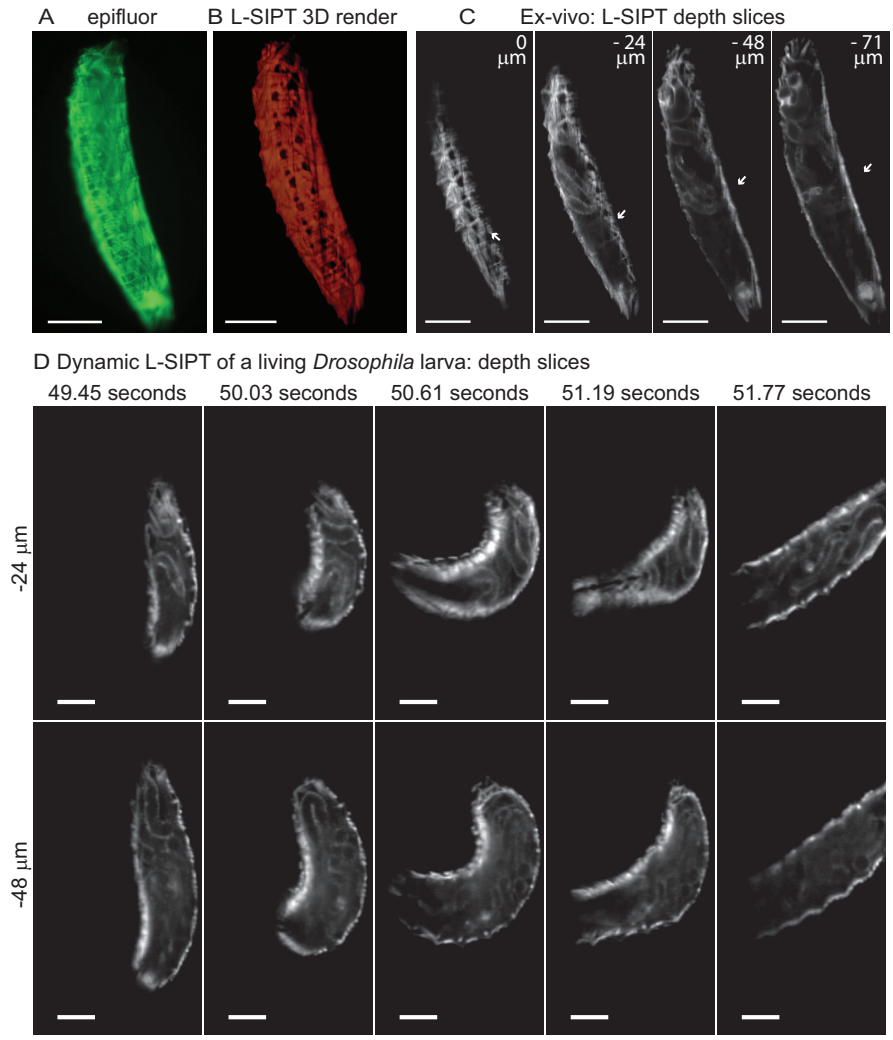

Figure 61: *In-vivo* L-SIPT imaging of a single 1st instar Drosophila larva expressing GFP in circumferential muscles under the control of the myosin heavy chain promoter. A.) 4x epifluorescence image (FITC cube) and B.) L-SIPT 3D volume render. C.) L-SIPT 'depth' slices demonstrate that both the exterior muscles (arrows) and interior autofluorescence from the digestive tract can be visualized in the intact animal. D.) Dynamic L-SIPT 'depth' slices from a 3D timelapse movie of the larva acquired *in-vivo* at 1.72 volumes per second. The larva was allowed to freely move in a drop of saline at room temperature while scanned. Scale bars 200 µm. A-C.) were acquired postmortem.

We repeated this experiment with our improved version of L-SIPT capable of volumetric scan rates > 20 VPS (Table 3) and a transgenic *Drosophila* larva strain with upregulated GFP signal in its external muscles (MHCtauGFP) (Maqbool et al. 2006). This strain has GFP expression patterns similar to the strain shown in Figure 61. The 1st instar larva was allowed to crawl freely in a molded agar chamber (4% agar in PBS) while it was rapidly scanned with L-

SIPT (Figure 55A). The 10x Olympus lens in Table 3 was used for camera lens 1. Two L-SIPT depth planes approximately 16 microns apart are shown across three consecutive frames acquired with 0.05 s time resolution. The improved spatiotemporal resolution of the second generation L-SIPT system is evident. The larva's heart is clearly visible inside the intact animal. With the volumetric scan speeds possible with L-SIPT we are able to capture the 3D dynamics of the heartbeat. This sample provided enough signal to allow for increased volumetric scan rates which would allow for improved tracking of heart and muscular dynamics. The ability to image freely moving organisms in 3D cross-section opens up myriad new possibilities for studying the biology of motion, and of non-stationary organs such as the heart.

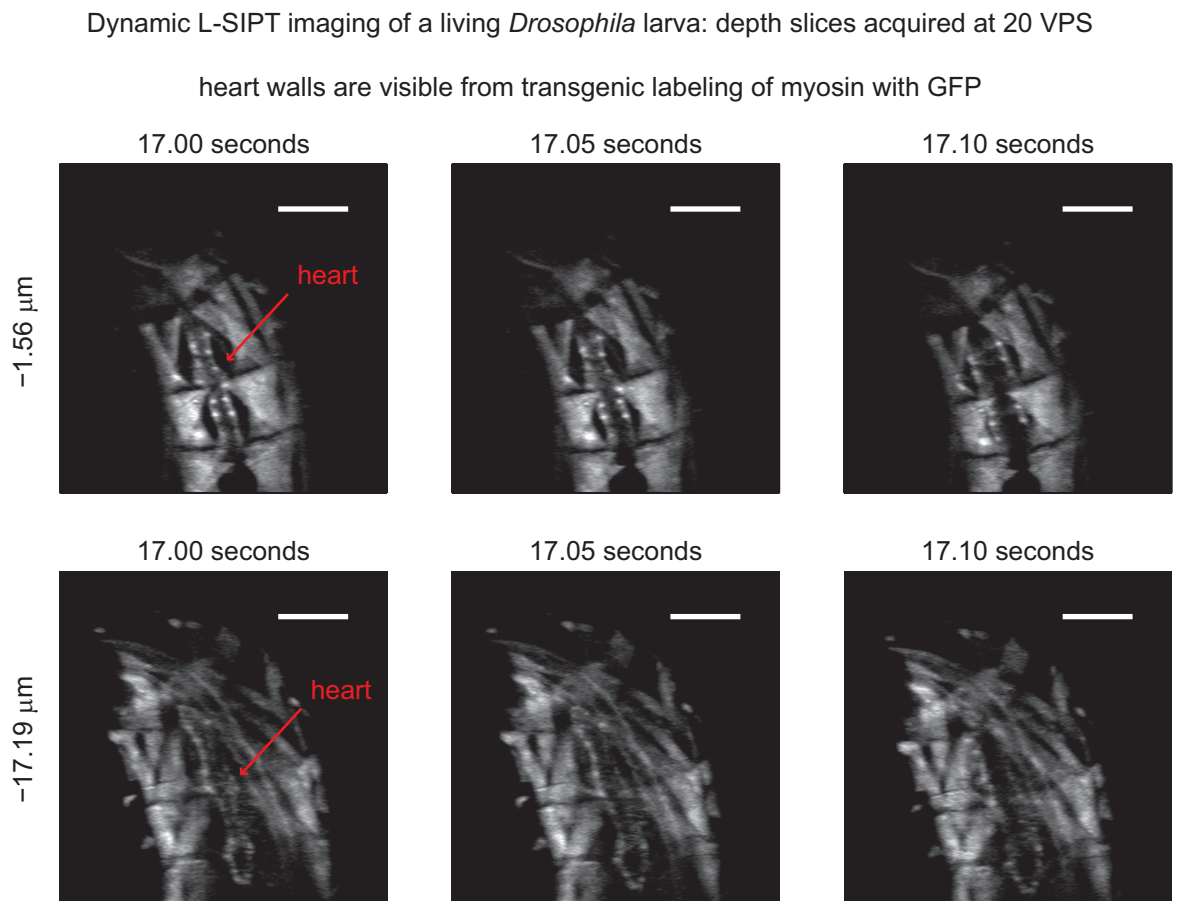

Figure 62: Improved *In-vivo* L-SIPT imaging of a single 1st instar Drosophila larva expressing GFP in circumferential muscles under the control of the myosin heavy chain promoter. After implementing a single-axis galvanometric scanner and high-speed camera we imaged a strain of larva with upregulated GFP labeling myosin heavy chain (MHCtauGFP). Here we show dynamic L-SIPT 'depth' slices from a 3D timelapse movie of the larva acquired *in-vivo* at 20 volumes per second. The larva was allowed to freely move in a drop of saline within a 4% agar in PBS chamber at room temperature while scanned. The 3D dynamics of the beating heart are well resolved with L-SIPT. Scale bars 200 µm. Data was smoothed using MATLAB's interp2 function with an interpolation factor of 2. Scale bars 200 µm.

3.3.3 Imaging calcium activity in an acute murine brain slice

Using the L-SIPT system configured according to Table 2, we imaged acute mouse brain slices transfected with GCaMP5G a genetically encoded calcium sensitive fluorescent protein (Akerboom et al. 2012). This experiment demonstrated L-SIPT's ability to track dynamic *in-vivo* processes at high temporal resolutions while maintaining the ability to resolve 3D objects as small as individual neurons. The slice was prepared and maintained according to established

protocols. The data in shown Figure 63 was acquired during a 30 second acquisition at 7 VPS over a volume of approximately 1100 x 1400 x 220 microns (scan, lateral, depth, respectively), and did not require any *a-priori* selection of neurons to observe (as a laser-scanning random sampling or reduced ROI scan technique would). An electrical stimulus was applied to the acute brain slice at t = 5 seconds by the bipolar electrode visible in the L-SIPT images (Figure 63B-C). Examining the resulting volumetric data, we observed a marked response to stimulation throughout the neuropil at all depths and across most locations of the slice. However, we also observed specific cells that, distinct from their surroundings or adjacent, shallower or deeper cells, exhibited spontaneous firing during the course of the acquisition. Figure 63A shows a 4x epifluorescence image (FITC cube) image of the brain slice following L-SIPT acquisition. Figure 63B shows selected planes from the L-SIPT volume with ROIs corresponding to the cells examined shown on their closest plane. Figure 63C shows a maximum intensity projection of the L-SIPT volume with each of 9 regions of interest labeled and color coded. Figure 63D shows the time-courses extracted from these regions of interest, with traces on the left showing the time-course of signal at each lateral ROI at a depth of -200 microns relative to the first image plane. The traces on the right show the signal in the same lateral ROIs, but at specific depths corresponding to the presence of spontaneously active (or temporally distinct) cells. This clearly demonstrates L-SIPT's ability to provide depth-sectioned data that is uncontaminated by deeper or shallower layers. Data shown is single-trial with no averaging or filtering. Figure 63E shows a magnified, pixel-wise interpolated region of interest at three different depths, at times corresponding to just prior to, and during spontaneous events. Arrows point to the tiny (but measurable) increases in fluorescence, demonstrating that responses are not due to out of plane or lateral motion artifacts. It is important to note that none of these 3 cells was visible in the

image prior to activation (a characteristic of GCaMP5G), such that these cells would have been overlooked in studies requiring pre-selection of regions of interest. Figure 63F illustrates the 3D locations of the regions of interest within the slice.

Experiment protocol

C57BL/6 mice aged postnatal day (P) 21 or older received intracortical injection of 60 nL of AAV2/1-*hsyn1-GCaMP5G* viruses at a rate of 60 nL/min, into two sites of the primary visual cortex at a depth of 200 μm from the pial surface, using a UMP3 microsyringe pump (World Precision Instruments). Mice of both sexes were used, housed and maintained in a temperature-controlled environment on a 12-h light-dark cycle, with *ad libitum* food and water. 2-6 weeks after the infection, acute slices, 400 μm thick, were prepared from mice around P60, using a HM 650V Vibrating-Blade Microtome (Thermo Scientific) after cardiac perfusion with ice-cold sucrose solution containing the following (in mM): 27 $NaHCO_3$, 1.5 NaH_2O_4, 222 sucrose, 2.6 KCl, 3 $MgSO_4$ and 1 $CaCl_2$. Slices were incubated at 37 °C for 30 min in ACSF containing (in mM): 126 NaCl, 26 $NaHCO_3$, 1.1 NaH_2O_4, 10 glucose, 3 KCl, 2 $MgSO_4$ and 2 $CaCl_2$. Sucrose and ACSF solutions were saturated with 95% O2 and 5% CO2. Experiments were performed in the ACSF. Electrical stimuli of cortical circuits was applied by bipolar platinum-iridium electrodes (Frederick Haer Co.), and were 2 ms in duration, 150 - 300 μA in amplitude, and applied as a train of 7 or 15 stimuli, each separated by 25 ms (40 Hz). All procedures were reviewed by the Columbia University Institutional Animal Care and Use Committee.

3D L-SIPT images were acquired with an Andor Imaging Zyla sCMOS continuously capturing images 800 x 80 pixels in size (lateral and depth, respectively) with a 416 microsecond

exposure time. Bidirectional scanning was performed using a custom cam-follower scanner with a 2° sweep. Images were cropped to their optimized zone and sample size in post-processing.

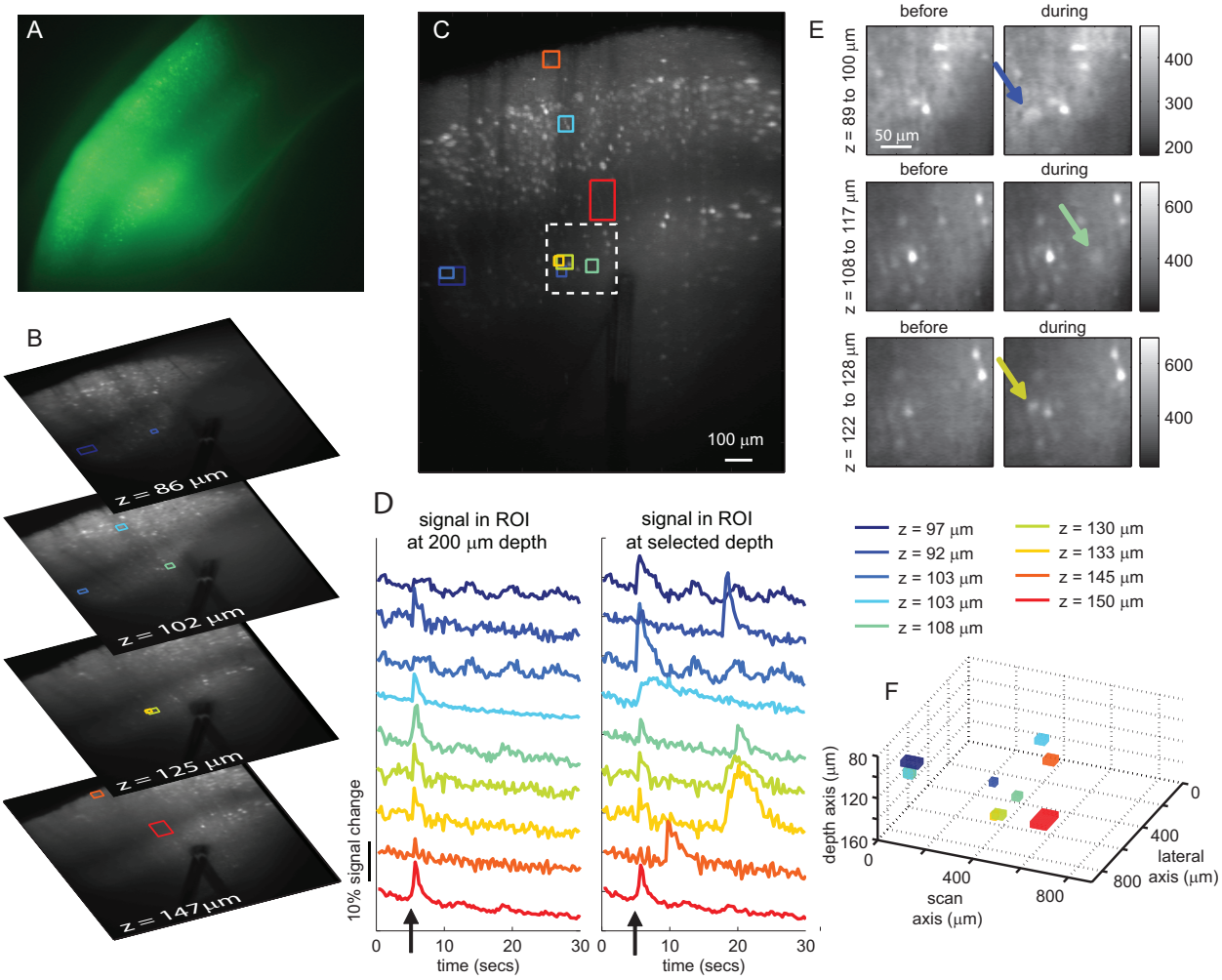

Figure 63: Dynamic L-SIPT data showing 3D intracellular calcium dynamics in an acute brain slice expressing GcaMP5. A.) 4x epifluorescence image (FITC cube) of the brain slice following L-SIPT imaging. B.) Selected image planes from the L-SIPT volume showing color-coded ROIs on their nearest plane. The stimulating electrode can be clearly seen as a black shadow. The surface of the slice was on a slight angle, such that cells are best resolved in different lateral locations at different depths C.) Maximum intensity projection of L-SIPT data with lateral ROIs shown. D.) Fluorescence intensity changes observed within each lateral ROI extracted (left) from a layer corresponding to -200 µm into the slice. The strong, ubiquitous response to stimulus (black arrow) can be seen in almost all cases. (right) shows signals extracted from the same lateral ROIs, but restricted to z-depths noted in legend to right corresponding to cells of interest. In all cases, independent dynamics are observed, including delayed spontaneous firing. This data is represented as time v/s depth maps. E.) Magnified region indicated by white dotted box in C.) after interpolation. Three different planes with the same lateral ROI show faint cells appearing during spontaneous firing (top to bottom are ROIs 2, 5 and 6). F.) 3D locations of regions of interest within the slice.

3.3.4 Exposed cortex imaging in rodent brain in-vivo

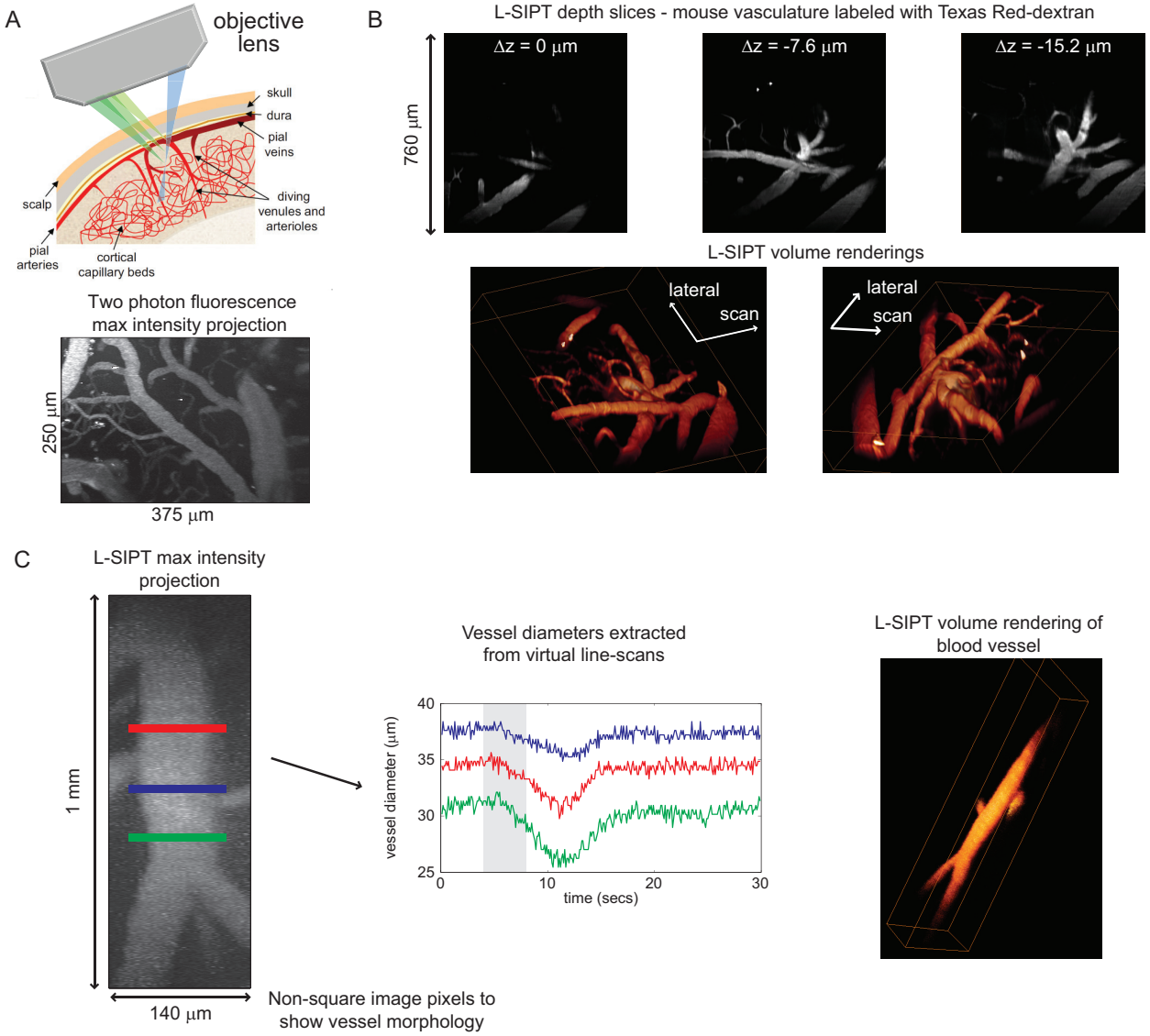

Figure 64: Initial results L-SIPT in-vivo cortical imaging in rodents. A.) L-SIPT imaging was performed in exposed mouse cortex under surgical anesthesia. The transgenic mouse expressed GCaMP3 in a sub-population of neurons under control of the Thy1 promoter. Texas Red-dextran was introduced to the vasculature via tail vein injection prior to imaging. (below) A two-photon fluorescence maximum intensity projection showing the labeled vasculate. B.) L-SIPT depth slices and volume renderings from a different region in the same animal. Depth slices compare well to the two- photon standard image. C.) High-speed L-SIPT volumetric acquisition in a second GCaMP3 postitive mouse demonstrates L-SIPT's ability to measure changes in blood vessel tone in response to somatosensory stimulation. (center) Timecourses of vessel diameters extracted from virtual line-scans taken at indicated locations. (right) volume rendering of measured blood vessel. Maximum intensity projection in A.) and C.) and L-SIPT depth slices in B.) smoothed via 2-dimensional spline interpolation using MATLAB's interp2 function.

An immediate challenge in neuroscience research is to be able to capture the dynamics of neuronal networks in 3D (Holekamp et al. 2008, Grewe et al. 2010, Grosberg et al. 2012). At the heart of decoding how neurons receive and relay information is the need to measure complete 3D networks, in parallel and at high speeds and with sufficient signal to noise to capture spontaneous events (i.e. detect functional responses in single trials). Most current approaches to high-speed neuronal imaging either acquire within a single plane, or require neurons of interest to be selected *a priori*, which necessarily biases acquired data. L-SIPT's ability to rapidly scan large, optically sectioned volumes holds the promise to allow for the capture of the 3D dynamics of complete cortical circuits. Here, we show the first preliminary results using L-SIPT to perform high-speed, volumetric imaging in living rodent cortex.

Experiment protocol

Using the system described in Table 3 we scanned the exposed cortex of a GCaMP3 positive mouse undergoing hindpaw electrical stimulation (Figure 64A) (Chen et al. 2012). GCaMP3 was expressed in a sub-population of neurons under control of the Thy1 promoter. In brief, the animal's skull was thinned and removed under surgical anesthesia. A coverslip window was placed over the exposed cortex and sealed to the skull using dental acrylic. Body temperature was maintained at 37°C using a heating pad. The 4^{th} ventricle was punctured to reduce pressure in the brain. Electrical stimuli synchronized to continuous L-SIPT volumetric image acquisition was provided to the hindpaw in 4 second intervals at 3 Hz with 3 ms stimulus widths, and amplitude of 1.0 ± 0.2 mA during certain acquisitions. 3D L-SIPT images were acquired from the contralateral side of the somatosensory cortex at various resolutions and volumetric scan rates. We used the exogenous fluorophore Texas Red conjugated to large dextran molecules to

provide fluorescent labeling to the animal's vasculature. Texas Red-dextran was administered via a tail-vein injection. Fluorescence was excited with a 488 nm laser (85-BCD-030-115, Melles Griot). Simultaneous dual-channel fluorescence detection was performed with a commercial image splitter with emission bands of 525 ± 50 nm and 600 ± 50 nm (Figure 54). Images were cropped to their optimized zone, fluorescence channel, and sample size in post-processing.

Results

We were unable to evoke a depth resolved response in the GCaMP3 fluorescence channel or were we able to resolve individual GCaMP3 labeled cells. This negative result was most likely due to the low magnification of the L-SIPT system (8.3X) and the low depth penetration of L-SIPT imaging, in addition responding cells could have been located at depths deeper than we were able to image. However, we were able to resolve blood vessels of varying sizes at depth using Texas Red-dextran as a contrast agent. In Figure 64B we show individual L-SIPT depth slices demonstrating L-SIPT's ability to optically section within the scattering mouse cortex. Volume rendering of the L-SIPT data shows the complete structure of the resolved vasculature network. These depth slices and the maximum intensity projection compare favorably to 2-photon fluorescence microscopy maximum intensity projection from the same animal shown in Figure 64A (920 nm two photon excitation, 560 - 650 nm emission). However, L-SIPT does not penetrate as deeply into the cortex as 2-photon fluorescence microscopy. This is due to L-SIPT using a visible light excitation wavelength and the rapid loss of the illumination light-sheet due to scattering as it penetrates into the cortex. We anticipate improvements in L-SIPT's penetration depth can be made using two-photon excitation, improved light-sheet formation optics, and/or adaptive optics.

The data shown in Figure 64B was acquired at a slow scan rate (0.01 VPS) across a large field of view to test L-SIPT's optical sectioning abilities in scattering cortical tissue at its best resolution. In a separate GCaMP3 mouse we performed high-speed scans (10 VPS) across small volumes to see if we could capture functional dynamics in response to stimulation. Figure 64C (left) shows one such vessel labeled with Texas Red-dextran where we observed changes in vessel diameter in single-trial responses to somatosensory stimulation. This image was stretched along the image's x-axis by approximately 250% to allow for visual inspection of the vessel morphology. Virtual line-scans were extracted from the 3D L-SIPT data in post-processing (virtual line-scan locations indicated by colored lines on maximum intensity projection image shown in Figure 64C (left)). The extracted timecourses shown in Figure 64C (center) clearly demonstrate L-SIPT's ability to resolve changes in vasculature tone in response to external stimulus. Vessel widths were calculated automatically by intensity thresholding the virtual line-scan and measuring the width of the vessel above the threshold. Figure 64C (right) shows a volume rendering of the measured blood vessel. Each virtual line-scan was extracted from a distinct L-SIPT depth plane which showed the best signal for that location on the blood vessel.

One of our central goals in developing L-SIPT is to perform high-speed functional neuroimaging in exposed rodent cortex. The results shown in this Section provide preliminary results pointing in the right direction towards achieving this goal. However, significant improvements in L-SIPT's depth penetration and ability to resolve small structures (~10 μm's) at depth in the cortex. We anticipate these improvements can be achieved through a combination of improved light delivery and collection optics, deconvolution approaches during post-processing, or incorporation of forward models of light propagation (Hillman et al. 2004). A complete model of the L-SIPT system using a commercially available optical design software package is

currently being constructed to determine the practical limits of L-SIPT spatial resolution and to design the system to achieve them. Additionally, L-SIPT could also be implemented using two-photon, Bessel beam or adaptive optics-optimized illumination, Powell lenses, or even multi-view configurations to further improve imaging performance (Planchon et al. 2011, Truong et al. 2011, Saghafi et al. 2013).

3.4 Summary

L-SIPT represents a fundamental shift in the types of and the speeds with which volumetric functional optical imaging data can be acquired. L-SIPT enables 3D imaging using light-sheet illumination without requiring translation of the sample relative to the imaging system for the first time by sweeping co-aligned illumination and detection planes. L-SIPT's *en-face*, translationless imaging geometry holds significant potential to image unconstrained, freely moving living samples in 3D at high spatial resolutions at and above video acquisition rates. The developed L-SIPT system is capable of acquiring signals from two different fluorescence channels simultaneously allowing powerful experiments studying both the morphological and functional interactions between multiple biological systems.

In developing the L-SIPT system we systematically demonstrated each component of the L-SIPT principle from the ground up using computer simulation codes, benchtop prototypes, and experiments imaging a series of increasingly complex optical phantoms and biological samples. We further developed the L-SIPT system for specific *in-vivo* functional optical imaging experiments: in imaging freely moving *Drosophila* larvae, calcium signaling dynamics in acute murine brain slices, and exposed cortical neuroimaging in rodents we have pushed and improved L-SIPT's spatial resolution and temporal resolution at each step of the way. An improved off-axis detection system was designed and incorporated into L-SIPT to improve spatial resolution. Video volumetric scan rates were achieved using a single-axis galvanometric scanner and a high-speed sCMOS camera.

While L-SIPT's resolution is currently lower than two-photon, confocal, and other light-sheet imaging techniques, it has the potential to achieve orders of magnitude improvements in imaging speed, enabling all regions of a large 3D volume to be sampled, precluding the need for

a priori selection of regions of interest. We have demonstrated that L-SIPT already has sufficient spatiotemporal resolution for sampling 3D neuronal calcium dynamics in living brain tissue, and for capturing the motion of small organisms. However, we expect that L-SIPT's imaging performance can be further enhanced using a higher end camera and scanner, custom optics, deconvolution approaches, or incorporation of forward models of light propagation (Hillman et al. 2004). A complete model of the L-SIPT system using a commercially available optical design software package is currently being constructed to determine the practical limits of L-SIPT spatial resolution and to design the system to achieve them. L-SIPT could also be implemented using two-photon, Bessel beam or adaptive optics-optimized illumination, Powell lenses, or even multi-view configurations to further improve imaging performance (Planchon et al. 2011, Truong et al. 2011, Saghafi et al. 2013).

Summary and future directions

Optical imaging is a powerful tool for the biological sciences and for clinical care because it is sensitive to a wide range of intrinsic, exogenous, and genetic sources of contrast and can be implemented in non-contact and non-destructive imaging geometries. Optical imaging is able to study the morphological and functional interactions between living biological systems simultaneously at unparalleled spatiotemporal resolutions. However, many existing optical techniques have been limited in their temporal acquisition speeds by their imaging geometry, light source, and/or hardware implementations. This thesis described the design, construction, and initial applications development of two novel, high-speed, functional optical imaging systems which have increased the spatiotemporal resolution with which functional optical imaging data can be acquired.

The 2D, wide-field, multispectral camera-based imaging system uses a camera-first design to deliver a 7.5 fold improvement in framerates over conventional functional multispectral imaging systems. High-speed, strobed LEDs allow for high-power illumination at almost any visible and NIR wavelength. Illumination is locked to image acquisition meaning the sample is only illuminated when an image is being exposed. This reduces photobleaching and photodamage to the sample, as well as reduces camera artifacts at high framerates. A second generation version of this system was built using laptop and a low-cost Firewire camera. This system was released as an open-source package to the scientific community to allow researchers access to cutting edge functional optical imaging technologies and spur additional development

of the system (SPLASSH). Both generations have been used in experiments studying neurovascular interactions in rodents *in-vivo* while the SPLASSH system was used as part of a pilot study investigating the use of optical imaging technologies in neurosurgical tumor resection guidance in humans. Future work on this system includes expanding the number of light sources which can be strobed sequentially. The current systems are limited to three light sources; however, additional sources could be added through modifications to the systems' control codes and hardware. With additional light sources high-speed multispectral absorption imaging could be combined with other functional imaging techniques such as laser-speckle contrast imaging (provides measurement of blood flow). Non-sequential strobe sequences could be developed to optimize image acquisition for combining imaging modalities. Additionally, the camera systems could be combined with simultaneous electrophysiological recordings to allow for direct, single-trial comparison between single cell and field potential recordings and optical data. Lastly, the camera systems could be combined with laser-scanning two-photon fluorescence microscopy to provide simultaneous measurements of global functional activity acquired with 3D-resolved, cellular scale functional imaging data.

The 3D imaging system, Laser-Scanning Intersecting Plane Tomography (L-SIPT), utilizes an *en-face*, single-lens translationless imaging geometry which can image unconstrained, freely moving living samples in 3D at high spatial resolutions at and above video acquisition rates (a 200 fold improvement over comparable technologies). L-SIPT achieves these framerates without requiring *a priori* knowledge of the sample for reduced ROI scanning and could be used to study the functional interactions within a complete neurovascular circuit. Further, L-SIPT's *en-face*, single lens geometry increases the sample diversity which can be scanned with high-speed, light-sheet illumination, making experiments such as *in-vivo* cortical imaging in rodents

possible. Here we described the full development of the L-SIPT system from concept to through several generations of benchtop prototypes. Geometrical raytrace models, imaging of synthetic and biological targets, and experiments imaging increasingly complex living biological systems were used to drive system development. Currently L-SIPT achieves a spatial resolution below comparable light-sheet illumination technologies such as multi-view SPIM. However, we expect improvements in L-SIPT imaging performance through optimization of the system's optical train, the use of off-line deconvolution approaches, the incorporation of forward models of light propagation, multiview implementations with image fusion, two-photon fluorescence excitation, and improvements in light-sheet generation. A complete model of the L-SIPT system using a commercially available optical design software package is currently being constructed to determine the practical limits of L-SIPT spatial resolution and to improve design the system's optical to achieve them. New technologies such as Bessel beams, Powell lenses, and adaptive optics-optimized illumination could be used to optimize the light sheet for scanning applications. Further, L-SIPT could be implemented with the new super-resolution technologies such as Stimulated Emission Depletion microscopy (STED) to further improve L-SIPT's spatial resolution. We anticipate with these improvements that L-SIPT will enable the study of 3D neurovascular interactions at spatiotemporal resolutions across large volumes not previously possible, as well as allow for cutting edge studies of freely moving organisms such as the interactions between the neuromuscular systems in crawling *Drosophila* larvae.

Bibliography

AB, N. M. (2013). "Microscopes: Time Line." Retrieved 1/31/2013, 2013, from http://www.nobelprize.org/educational/physics/microscopes/timeline/index.html.

Ahrens, M. B., M. B. Orger, D. N. Robson, J. M. Li and P. J. Keller (2013). "Whole-brain functional imaging at cellular resolution using light-sheet microscopy." Nat Methods **10**(5): 413-420.

Akerboom, J., T. W. Chen, T. J. Wardill, L. Tian, J. S. Marvin, S. Mutlu, N. C. Calderon, F. Esposti, B. G. Borghuis, X. R. Sun, A. Gordus, M. B. Orger, R. Portugues, F. Engert, J. J. Macklin, A. Filosa, A. Aggarwal, R. A. Kerr, R. Takagi, S. Kracun, E. Shigetomi, B. S. Khakh, H. Baier, L. Lagnado, S. S. Wang, C. I. Bargmann, B. E. Kimmel, V. Jayaraman, K. Svoboda, D. S. Kim, E. R. Schreiter and L. L. Looger (2012). "Optimization of a GCaMP Calcium Indicator for Neural Activity Imaging." J Neurosci **32**(40): 13819-13840.

Amoozegar, C. B., T. Wang, M. B. Bouchard, A. F. McCaslin, W. S. Blaner, R. M. Levenson and E. M. Hillman (2012). "Dynamic contrast-enhanced optical imaging of in vivo organ function." J Biomed Opt **17**(9): 96003-96001.

Bahlmann, K., P. T. C. So, M. Kirber, R. Reich, B. Kosicki, W. McGonagle and K. Bellve (2007). "Multifocal multiphoton microscopy (MMM) at a frame rate beyond 600 Hz." Optics Express **15**(17): 10991-10998.

Baik, A. D., J. Qiu, E. M. Hillman, C. Dong and X. E. Guo (2013). "Simultaneous tracking of 3D actin and microtubule strains in individual MLO-Y4 osteocytes under oscillatory flow." Biochem Biophys Res Commun **431**(4): 718-723.

Berwick, J., D. Johnston, M. Jones, J. Martindale, P. Redgrave, N. McLoughlin, I. Schiessl and J. E. Mayhew (2005). "Neurovascular coupling investigated with two-dimensional optical imaging spectroscopy in rat whisker barrel cortex." Eur J Neurosci **22**(7): 1655-1666.

Blood, A. J., N. Pouratian and A. W. Toga (2002). "Temporally staggered forelimb stimulation modulates barrel cortex optical intrinsic signal responses to whisker stimulation." J Neurophysiol **88**(1): 422-437.

Blood, A. J., N. Pouratian and A. W. Toga (2002). "Temporally staggered forelimb stimulation modulates barrel cortex optical intrinsic signal responses to whisker stimulation." J Neurophysiol **88**(1): 422-437.

Boot, M. J., C. H. Westerberg, J. Sanz-Ezquerro, J. Cotterell, R. Schweitzer, M. Torres and J. Sharpe (2008). "In vitro whole-organ imaging: 4D quantification of growing mouse limb buds." Nat Methods **5**(7): 609-612.

Bouchard, M. B., S. A. Burgess, P. Moussazadeh, A. J. Radosevich, J. P. Wuskell, L. M. Loew, A. Pertsov and E. M. C. Hillman (2008). Electrical and metabolic imaging of cardiac ischemia. OSA BIOMED 2008, St. Petersburg, FL, (Submitted).

Bouchard, M. B., B. R. Chen, S. A. Burgess and E. M. C. Hillman (2009). Ultra-fast multiwavelength CCD-based optical imaging. 2009 Engineering Conferences International Advances in Optics for Biotechnology, Medicine, and Surgery XI. Burlington, VT, USA.

Bouchard, M. B., B. R. Chen, S. A. Burgess and E. M. C. Hillman (2009). "Ultra-fast multispectral optical imaging of cortical oxygenation, blood flow, and intracellular calcium dynamics." Opt Express **17**(18): 15670-15678.

Bouchard, M. B., S. A. MacLaurin, P. J. Dwyer, J. Mansfield, R. Levenson and T. Krucker (2007). "Technical considerations in longitudinal multispectral small animal molecular imaging." J Biomed Opt **12**(5): 051601.

Buytaert, J. A. and J. J. Dirckx (2007). "Design and quantitative resolution measurements of an optical virtual sectioning three-dimensional imaging technique for biomedical specimens, featuring two-micrometer slicing resolution." J Biomed Opt **12**(1): 014039.

BYU-optics-lab. (2009). "(web resource) BYU Photonics - ABCD Matrix Analysis Tutorial/Ray Transfer Matrix Analysis/Transfer Matrices." 2013, from http://www.photonics.byu.edu/ABCD_Matrix_tut.phtml.

Cai, D., K. B. Cohen, T. Luo, J. W. Lichtman and J. R. Sanes (2013). "Improved tools for the Brainbow toolbox." Nat Methods **10**(6): 540-547.

Chalfie, M., Y. Tu, G. Euskirchen, W. W. Ward and D. C. Prasher (1994). "Green fluorescent protein as a marker for gene expression." Science **263**(5148): 802-805.

Chaney, A. J. B. (2013). "(web resource) Rayleigh scattering." Retrieved September 15, 2013, 2013, from http://www.princeton.edu/~achaney/tmve/wiki100k/docs/Rayleigh_scattering.html.

Chen, B. R., M. B. Bouchard, A. F. McCaslin, S. A. Burgess and E. M. Hillman (2011). "High-speed vascular dynamics of the hemodynamic response." NeuroImage **54**(2): 1021-1030.

Chen, Q., J. Cichon, W. Wang, L. Qiu, S. J. Lee, N. R. Campbell, N. Destefino, M. J. Goard, Z. Fu, R. Yasuda, L. L. Looger, B. R. Arenkiel, W. B. Gan and G. Feng (2012). "Imaging neural activity using Thy1-GCaMP transgenic mice." Neuron **76**(2): 297-308.

Chung, K. and K. Deisseroth (2013). "CLARITY for mapping the nervous system." Nat Methods **10**(6): 508-513.

Dani, J. W., A. Chernjavsky and S. J. Smith (1992). "Neuronal activity triggers calcium waves in hippocampal astrocyte networks." Neuron **8**(3): 429-440.

Denk, W., J. H. Strickler and W. W. Webb (1990). "Two-photon laser scanning fluorescence microscopy." Science **248**(4951): 73-76.

Devor, A., A. K. Dunn, M. L. Andermann, I. Ulbert, D. A. Boas and A. M. Dale (2003). "Coupling of total hemoglobin concentration, oxygenation, and neural activity in rat somatosensory cortex." Neuron **39**(2): 353-359.

Devor, A., E. M. Hillman, P. Tian, C. Waeber, I. C. Teng, L. Ruvinskaya, M. H. Shalinsky, H. Zhu, R. H. Haslinger, S. N. Narayanan, I. Ulbert, A. K. Dunn, E. H. Lo, B. R. Rosen, A. M. Dale, D. Kleinfeld and D. A. Boas (2008). "Stimulus-induced changes in blood flow and 2-deoxyglucose uptake dissociate in ipsilateral somatosensory cortex." J Neurosci **28**(53): 14347-14357.

Devor, A., I. Ulbert, A. K. Dunn, S. N. Narayanan, S. R. Jones, M. L. Andermann, D. A. Boas and A. M. Dale (2005). "Coupling of the cortical hemodynamic response to cortical and thalamic neuronal activity." Proc Natl Acad Sci U S A **102**(10): 3822-3827.

Dodt, H. U., U. Leischner, A. Schierloh, N. Jahrling, C. P. Mauch, K. Deininger, J. M. Deussing, M. Eder, W. Zieglgansberger and K. Becker (2007). "Ultramicroscopy: three-dimensional visualization of neuronal networks in the whole mouse brain." Nat Methods **4**(4): 331-336.

Dunn, A. K., A. Devor, H. Bolay, M. L. Andermann, M. A. Moskowitz, A. M. Dale and D. A. Boas (2003). "Simultaneous imaging of total cerebral hemoglobin concentration, oxygenation, and blood flow during functional activation." Optics Letters **28**(1): 28-30.

Dunn, A. K., A. Devor, A. M. Dale and D. A. Boas (2005). "Spatial extent of oxygen metabolism and hemodynamic changes during functional activation of the rat somatosensory cortex." NeuroImage **27**(2): 279-290.

Dunsby, C. (2008). "Optically sectioned imaging by oblique plane microscopy." Opt Express **16**(25): 20306-20316.

Dwyer, P. J., C. A. DiMarzio and M. Rajadhyaksha (2007). "Confocal theta line-scanning microscope for imaging human tissues." Appl Opt **46**(10): 1843-1851.

Dwyer, P. J., C. A. DiMarzio, J. M. Zavislan, W. J. Fox and M. Rajadhyaksha (2006). "Confocal reflectance theta line scanning microscope for imaging human skin in vivo." Opt Lett **31**(7): 942-944.

Ed. Diaspro, A. (2002). Confocal and Two-Photon Microscopy, Foundations, Applications, and Advances, Wiley.

Foundation, A. (2013). "Arduino - HomePage." Retrieved September 5, 2013, 2013, from http://www.arduino.cc/.

Fox, M. D., A. Z. Snyder, J. L. Vincent, M. Corbetta, D. C. Van Essen and M. E. Raichle (2005). "The human brain is intrinsically organized into dynamic, anticorrelated functional networks." Proceedings of the National Academy of Sciences of the United States of America **102**(27): 9673-9678.

Fuwa, K. and B. L. Valle (1963). "The Physical Basis of Analytical Atomic Absorption Spectrometry. The Pertinence of the Beer-Lambert Law." Analytical Chemistry **35**(8): 942-946.

Goeppert-Mayer, M. (1931). "Über Elementarakte mit zwei Quantensprüngen." Annalen der Physik **401**(3): 273-294.

Gordon, G. R., S. J. Mulligan and B. A. MacVicar (2007). "Astrocyte control of the cerebrovasculature." Glia **55**(12): 1214-1221.

Grewe, B. F., D. Langer, H. Kasper, B. M. Kampa and F. Helmchen (2010). "High-speed in vivo calcium imaging reveals neuronal network activity with near-millisecond precision." Nat Methods **7**(5): 399-405.

Grinvald, A., E. Lieke, R. D. Frostig, C. D. Gilbert and T. N. Wiesel (1986). "Functional architecture of cortex revealed by optical imaging of intrinsic signals." Nature **324**(6095): 361-364.

Grosberg, L. E., B. R. Chen and E. M. Hillman (2012). "Simultaneous multiplane in vivo nonlinear microscopy using spectral encoding." Opt Lett **37**(14): 2967-2969.

Grosberg, L. E., B. R. Chen and E. M. C. Hillman (2012). "Simultaneous multiplane in vivo nonlinear microscopy using spectral encoding." Opt Lett **37**(14): 2967-2969.

Grosberg, L. E., A. J. Radosevich, S. Asfaha, T. C. Wang and E. M. Hillman (2011). "Spectral characterization and unmixing of intrinsic contrast in intact normal and diseased gastric tissues using hyperspectral two-photon microscopy." PLoS One **6**(5): e19925.

Grueber, W. B., L. Y. Jan and Y. N. Jan (2002). "Tiling of the Drosophila epidermis by multidendritic sensory neurons." Development **129**(12): 2867-2878.

Grueber, W. B., L. Y. Jan and Y. N. Jan (2003). "Different levels of the homeodomain protein cut regulate distinct dendrite branching patterns of Drosophila multidendritic neurons." Cell **112**(6): 805-818.

H. J. Noordmans, R. de Roode and R. Verdaasdonk (2007). Compact multi-spectral imaging system for dermatology and neurosurgery. Medical Imaging 2007: Physics of Medical Imaging, 65100I, San Diego, CA, SPIE.

Haglund, M. M., G. A. Ojemann and D. W. Hochman (1992). "Optical imaging of epileptiform and functional activity in human cerebral cortex." Nature **358**(6388): 668-671.

Hahlweg, C. and H. Rothe (2007). Spectroscopic imaging from 400nm to 1800nm with liquid crystal tunable filters. Machine Vision Applications in Industrial Inspection XV, San Jose, CA, USA, SPIE.

Hama, H., H. Kurokawa, H. Kawano, R. Ando, T. Shimogori, H. Noda, K. Fukami, A. Sakaue-Sawano and A. Miyawaki (2011). "Scale: a chemical approach for fluorescence imaging and reconstruction of transparent mouse brain." Nat Neurosci **14**(11): 1481-1488.

Hecht, E. (2001). Optics, Addison-Wesley.

Helmchen, F. and W. Denk (2005). "Deep tissue two-photon microscopy." Nat Methods **2**(12): 932-940.

Hillman, E. M. (2007). "Optical brain imaging in vivo: techniques and applications from animal to man." J Biomed Opt **12**(5): 051402.

Hillman, E. M., D. A. Boas, A. M. Dale and A. K. Dunn (2004). "Laminar optical tomography: demonstration of millimeter-scale depth-resolved imaging in turbid media." Opt Lett **29**(14): 1650-1652.

Hillman, E. M., A. Devor, M. B. Bouchard, A. K. Dunn, G. W. Krauss, J. Skoch, B. J. Bacskai, A. M. Dale and D. A. Boas (2007). "Depth-resolved optical imaging and microscopy of vascular compartment dynamics during somatosensory stimulation." Neuroimage **35**(1): 89-104.

Hillman, E. M. and A. Moore (2007). "All-optical anatomical co-registration for molecular imaging of small animals using dynamic contrast." Nat Photonics **1**(9): 526-530.

Hillman, E. M., B. Yuan, S. Burgess, A. Iranmahboob and M. Bouchard (2007). Depth-resolved optical imaging of calcium sensitive dyes in somatosensory cortex in-vivo. Society for Neuroscience Annual Meeting 2007. San Diego, CA, SfN.

Holekamp, T. F., D. Turaga and T. E. Holy (2008). "Fast three-dimensional fluorescence imaging of activity in neural populations by objective-coupled planar illumination microscopy." Neuron **57**(5): 661-672.

Huisken, J. and D. Y. Stainier (2009). "Selective plane illumination microscopy techniques in developmental biology." Development **136**(12): 1963-1975.

Jacques, S. L. and S. A. Prahl. (1998). "(web resource) ECE 532, 3. Optical Properties." 2013, from http://omlc.ogi.edu/education/ece532/class3/musp.html.

Jacques, S. L. and S. A. Prahl. (1998). "(web resource) ECE 532, 3. Optical Properties." 2013, from http://omlc.ogi.edu/classroom/ece532/class3/gdefinition.html.

Jacques, S. L. and S. A. Prahl. (1998). "(web resource) ECE 532, E. Optical Properties." 2013, from http://omlc.ogi.edu/classroom/ece532/class3/musdefinition.html.

Jacques, S. L. and S. A. Prahl. (1998, 2002). "(web resource) ECE 532 Introduction to Biomedical Optics." 2013, from http://omlc.ogi.edu/education/ece532/.

Jones, M., J. Berwick, D. Johnston and J. Mayhew (2001). "Concurrent optical imaging spectroscopy and laser-Doppler flowmetry: the relationship between blood flow, oxygenation, and volume in rodent barrel cortex." NeuroImage **13**(6 Pt 1): 1002-1015.

Kasahara, T. (2002). MICROSCOPE OBJECTIVE LENS. USPTO. U. S. A., Olympus Optical Co., Ltd. **6501603**.

Kazmi, S. M., A. J. Salvaggio, A. D. Estrada, M. A. Hemati, N. K. Shaydyuk, E. Roussakis, T. A. Jones, S. A. Vinogradov and A. K. Dunn (2013). "Three-dimensional mapping of oxygen tension in cortical arterioles before and after occlusion." Biomed Opt Express **4**(7): 1061-1073.

Keller, P. J., A. D. Schmidt, A. Santella, K. Khairy, Z. Bao, J. Wittbrodt and E. H. Stelzer (2010). "Fast, high-contrast imaging of animal development with scanned light sheet-based structured-illumination microscopy." Nat Methods **7**(8): 637-642.

Klose, A. D. and A. H. Hielscher (1999). "Iterative reconstruction scheme for optical tomography based on the equation of radiative transfer." Med Phys **26**(8): 1698-1707.

Kocsis, L., P. Herman and A. Eke (2006). "The modified Beer-Lambert law revisited." Phys Med Biol **51**(5): N91-98.

Kozberg, M. G., B. R. Chen, S. E. DeLeo, M. B. Bouchard and E. M. Hillman (2013). "Resolving the transition from negative to positive blood oxygen level-dependent responses in the developing brain." Proc Natl Acad Sci U S A **110**(11): 4380-4385.

Krzic, U., S. Gunther, T. E. Saunders, S. J. Streichan and L. Hufnagel (2012). "Multiview light-sheet microscope for rapid in toto imaging." Nat Methods **9**(7): 730-733.

Kwong, K. K., J. W. Belliveau, D. A. Chesler, I. E. Goldberg, R. M. Weisskoff, B. P. Poncelet, D. N. Kennedy, B. E. Hoppel, M. S. Cohen, R. Turner and et al. (1992). "Dynamic magnetic resonance imaging of human brain activity during primary sensory stimulation." Proc Natl Acad Sci U S A **89**(12): 5675-5679.

Lansford, R., G. Bearman and S. E. Fraser (2001). "Resolution of multiple green fluorescent protein color variants and dyes using two-photon microscopy and imaging spectroscopy." J Biomed Opt **6**(3): 311-318.

Lawlor, J., D. W. Fletcher-Holmes, A. R. Harvey and A. I. McNaught (2002). "In Vivo Hyperspectral Imaging of Human Retina and Optic Disc " Investigative Ophthalmology & Visual Science **34**: 4350.

Levenson, R. M. and J. R. Mansfield (2006). "Multispectral imaging in biology and medicine: slices of life." Cytometry A **69**(8): 748-758.

Livet, J., T. A. Weissman, H. Kang, R. W. Draft, J. Lu, R. A. Bennis, J. R. Sanes and J. W. Lichtman (2007). "Transgenic strategies for combinatorial expression of fluorescent proteins in the nervous system." Nature **450**(7166): 56-62.

Lu, H. D., G. Chen, D. Y. Ts'o and A. W. Roe (2009). "A rapid topographic mapping and eye alignment method using optical imaging in Macaque visual cortex." NeuroImage **44**(3): 636-646.

Mahr, A. and H. Aberle (2006). "The expression pattern of the Drosophila vesicular glutamate transporter: a marker protein for motoneurons and glutamatergic centers in the brain." Gene Expr Patterns **6**(3): 299-309.

Malonek, D. and A. Grinvald (1996). "Interactions between electrical activity and cortical microcirculation revealed by imaging spectroscopy: implications for functional brain mapping." Science **272**(5261): 551-554.

Maqbool, T., C. Soler, T. Jagla, M. Daczewska, N. Lodha, S. Palliyil, K. VijayRaghavan and K. Jagla (2006). "Shaping leg muscles in Drosophila: role of ladybird, a conserved regulator of appendicular myogenesis." PLoS One **1**: e122.

Mayevsky, A. and B. Chance (2007). "Oxidation-reduction states of NADH in vivo: From animals to clinical use." Mitochondrion **7**(5): 330-339.

McCaslin, A. F. H., B. R. Chen, A. J. Radosevich, B. Cauli and E. M. C. Hillman (2009). In-vivo 3D morphology of astrocyte-vasculature interactions in the somatosensory cortex. Society for Neuroscience Annual Meeting. Chicago, IL, SfN**:** 324.327.

Minsky, M. (2011). "Memoir on inventing the confocal scanning microscope." Scanning **10**(4): 128-138.

Mohajerani, M. H., A. W. Chan, M. Mohsenvand, J. Ledue, R. Liu, D. A. McVea, J. D. Boyd, Y. T. Wang, M. Reimers and T. H. Murphy (2013). "Spontaneous cortical activity alternates between motifs defined by regional axonal projections." Nat Neurosci.

Muldoon, T. J., M. C. Pierce, D. L. Nida, M. D. Williams, A. Gillenwater and R. Richards-Kortum (2007). "Subcellular-resolution molecular imaging within living tissue by fiber microendoscopy." Opt Express **15**(25): 16413-16423.

Murphy, D. B. (2001). Fundamentals of Light Microscopy and Electronic Imaging. U. S. A., WIley-Liss, Inc.

Nakai, J., M. Ohkura and K. Imoto (2001). "A high signal-to-noise Ca(2+) probe composed of a single green fluorescent protein." Nat Biotechnol **19**(2): 137-141.

Owen, A. M., C. E. Stern, R. B. Look, I. Tracey, B. R. Rosen and M. Petrides (1998). "Functional organization of spatial and nonspatial working memory processing within the human lateral frontal cortex." Proceedings of the National Academy of Sciences of the United States of America **95**(13): 7721-7726.

Palero, J. A., H. S. de Bruijn, A. van der Ploeg van den Heuvel, H. J. Sterenborg and H. C. Gerritsen (2007). "Spectrally resolved multiphoton imaging of in vivo and excised mouse skin tissues." Biophys J **93**(3): 992-1007.

Peterka, D. S., H. Takahashi and R. Yuste (2011). "Imaging voltage in neurons." Neuron **69**(1): 9-21.

Photometrics. (2013). "Photometrics Dual-View and Quad-View Imaging Systems." Retrieved February 9, 2013, 2013, from http://www.photometrics.com/products/multichannel/.

Planchon, T. A., L. Gao, D. E. Milkie, M. W. Davidson, J. A. Galbraith, C. G. Galbraith and E. Betzig (2011). "Rapid three-dimensional isotropic imaging of living cells using Bessel beam plane illumination." Nat Methods **8**(5): 417-423.

Pouratian, N., A. F. Cannestra, N. A. Martin and A. W. Toga (2002). "Intraoperative optical intrinsic signal imaging: a clinical tool for functional brain mapping." Neurosurg Focus **13**(4): e1.

Prahl, S. A. (1999). "Online resource: http://omlc.ogi.edu/spectra/hemoglobin/summary.html."

Prakash, N., J. D. Biag, S. A. Sheth, S. Mitsuyama, J. Theriot, C. Ramachandra and A. W. Toga (2007). "Temporal profiles and 2-dimensional oxy-, deoxy-, and total-hemoglobin somatosensory maps in rat versus mouse cortex." NeuroImage **37 Suppl 1**: S27-36.

Radosevich, A. J., M. B. Bouchard, S. A. Burgess, B. R. Chen and E. M. Hillman (2008). "Hyperspectral in vivo two-photon microscopy of intrinsic contrast." Opt Lett **33**(18): 2164-2166.

Rahman, M. S., N. Ingole, D. Roblyer, V. Stepanek, R. Richards-Kortum, A. Gillenwater, S. Shastri and P. Chaturvedi (2010). "Evaluation of a low-cost, portable imaging system for early detection of oral cancer." Head Neck Oncol **2**: 10.

Ranji, M., D. L. Jaggard, S. V. Apreleva, S. A. Vinogradov and B. Chance (2006). "Simultaneous fluorometry and phosphorometry of Langendorff perfused rat heart: ex vivo animal studies." Opt Lett **31**(20): 2995-2997.

Rayshubskiy, A., T. J. Wojtasiewicz, C. B. Mikell, M. B. Bouchard, D. Timerman, B. E. Youngerman, R. A. McGovern, M. L. Otten, P. D. Canoll, G. M. McKhann II and E. M. C. Hillman (2013). "Direct, intraoperative of ~0.1 Hz hemodynamic oscillations in awake human cortex: Implications for fMRI." NeuroImage **under review**.

Rudin, M. and R. Weissleder (2003). "Molecular imaging in drug discovery and development." Nat Rev Drug Discov **2**(2): 123-131.

Ruzin, S. and H. Aaron. (2013). "(Web resource) Two-photon fluorescence microscopy." from http://microscopy.berkeley.edu/courses/tlm/2P/index.html.

Saghafi, S., K. Becker, C. Hahn and H. U. Dodt (2013). "3D-ultramicroscopy utilizing aspheric optics." J Biophotonics.

Sakaguchi, K., T. Tachibana, S. Furukawa, T. Katsura, K. Yamazaki, H. Kawaguchi, A. Maki and E. Okada (2007). "Experimental prediction of the wavelength-dependent path-length factor for optical intrinsic signal analysis." Appl Opt **46**(14): 2769-2777.

Schuster, C. M., G. W. Davis, R. D. Fetter and C. S. Goodman (1996). "Genetic dissection of structural and functional components of synaptic plasticity. I. Fasciclin II controls synaptic stabilization and growth." Neuron **17**(4): 641-654.

Sharpe, J. (2003). "Optical projection tomography as a new tool for studying embryo anatomy." J Anat **202**(2): 175-181.

Sharpe, J., U. Ahlgren, P. Perry, B. Hill, A. Ross, J. Hecksher-Sorensen, R. Baldock and D. Davidson (2002). "Optical projection tomography as a tool for 3D microscopy and gene expression studies." Science **296**(5567): 541-545.

Sheth, S. A., M. Nemoto, M. W. Guiou, M. A. Walker and A. W. Toga (2005). "Spatiotemporal evolution of functional hemodynamic changes and their relationship to neuronal activity." J Cereb Blood Flow Metab **25**(7): 830-841.

Shin, H. K., M. Nishimura, P. B. Jones, H. Ay, D. A. Boas, M. A. Moskowitz and C. Ayata (2008). "Mild induced hypertension improves blood flow and oxygen metabolism in transient focal cerebral ischemia." Stroke **39**(5): 1548-1555.

Shoham, D., D. E. Glaser, A. Arieli, T. Kenet, C. Wijnbergen, Y. Toledo, R. Hildesheim and A. Grinvald (1999). "Imaging cortical dynamics at high spatial and temporal resolution with novel blue voltage-sensitive dyes." Neuron **24**(4): 791-802.

Staveley, B. E. "(web resource) ch02f01.jpg." Retrieved September 18, 2013, 2013, from http://www.mun.ca/biology/desmid/brian/BIOL3530/DEVO_02/ch02f01.jpg.

Sun, R., M. B. Bouchard, S. A. Burgess, A. J. Radosevich and E. M. C. Hillman (2010). A Low-Cost, Portable System for High-Speed Multispectral Optical Imaging. OSA Biomedical Optics, Miami, FL, Optical Society of America.

Sun, R., M. B. Bouchard and E. M. Hillman (2010). "SPLASSH: Open source software for camera-based high-speed, multispectral in-vivo optical image acquisition." Biomed Opt Express **1**(2): 385-397.

Svanberg, K., I. Wang, S. Colleen, I. Idvall, C. Ingvar, R. Rydell, D. Jocham, H. Diddens, S. Bown, G. Gregory, S. Montan, S. Andersson-Engels and S. Svanberg (1998). "Clinical multi-colour fluorescence imaging of malignant tumours--initial experience." Acta Radiol **39**(1): 2-9.

Themelis, G., J. S. Yoo and V. Ntziachristos (2008). "Multispectral imaging using multiple-bandpass filters." Opt Lett **33**(9): 1023-1025.

Themelis, G., J. S. Yoo, K. S. Soh, R. Schulz and V. Ntziachristos (2009). "Real-time intraoperative fluorescence imaging system using light-absorption correction." J Biomed Opt **14**(6): 064012.

Tomer, R., K. Khairy, F. Amat and P. J. Keller (2012). "Quantitative high-speed imaging of entire developing embryos with simultaneous multiview light-sheet microscopy." Nat Methods **9**(7): 755-763.

Troyan, S. L., V. Kianzad, S. L. Gibbs-Strauss, S. Gioux, A. Matsui, R. Oketokoun, L. Ngo, A. Khamene, F. Azar and J. V. Frangioni (2009). "The FLARE intraoperative near-infrared fluorescence imaging system: a first-in-human clinical trial in breast cancer sentinel lymph node mapping." Ann Surg Oncol **16**(10): 2943-2952.

Truong, T. V., W. Supatto, D. S. Koos, J. M. Choi and S. E. Fraser (2011). "Deep and fast live imaging with two-photon scanned light-sheet microscopy." Nat Methods **8**(9): 757-760.

Tsai, P. S., N. Nishimura, E. J. Yoder, E. M. Dolnick, G. A. White and D. Kleinfeld (2002). In Vivo Optical Imaging of Brain Function. Boca Raton, CRC Press.

Tso, D. Y., R. D. Frostig, E. E. Lieke and A. Grinvald (1990). "Functional-Organization of Primate Visual-Cortex Revealed by High-Resolution Optical Imaging." Science **249**(4967): 417-420.

Turaga, D. and T. E. Holy (2012). "Organization of vomeronasal sensory coding revealed by fast volumetric calcium imaging." J Neurosci **32**(5): 1612-1621.

van Munster, E. B. and T. W. Gadella (2005). "Fluorescence lifetime imaging microscopy (FLIM)." Adv Biochem Eng Biotechnol **95**: 143-175.

Vanzetta, I., R. Hildesheim and A. Grinvald (2005). "Compartment-resolved imaging of activity-dependent dynamics of cortical blood volume and oximetry." J Neurosci **25**(9): 2233-2244.

Verveer, P. J., J. Swoger, F. Pampaloni, K. Greger, M. Marcello and E. H. Stelzer (2007). "High-resolution three-dimensional imaging of large specimens with light sheet-based microscopy." Nat Methods **4**(4): 311-313.

Walls, J. R., J. G. Sled, J. Sharpe and R. M. Henkelman (2007). "Resolution improvement in emission optical projection tomography." Phys Med Biol **52**(10): 2775-2790.

Zemlin, C. W., O. Bernus, A. Matiukas, C. J. Hyatt and A. M. Pertsov (2008). "Extracting intramural wavefront orientation from optical upstroke shapes in whole hearts." Biophys J **95**(2): 942-950.

Zijlstra, W. G., A. Buursma and W. P. Meeuwsen-van der Roest (1991). "Absorption spectra of human fetal and adult oxyhemoglobin, de-oxyhemoglobin, carboxyhemoglobin, and methemoglobin." Clin Chem **37**(9): 1633-1638.

Zimmermann, T., J. Rietdorf and R. Pepperkok (2003). "Spectral imaging and its applications in live cell microscopy." FEBS Lett **546**(1): 87-92.